THE UNIVERSITY OF CHICAGO

COARSE GRAINED MODELING OF BLOCK COPOLYMER LITHOGRAPHY: THE EFFECTS OF PATTERN DESIGN ON THE THERMODYNAMICS AND KINETICS OF THE DIRECTED SELF ASSEMBLY OF BLOCK COPOLYMERS

A DISSERTATION SUBMITTED TO
THE FACULTY OF THE INSTITUTE FOR MOLECULAR ENGINEERING
IN CANDIDACY FOR THE DEGREE OF
DOCTOR OF PHILOSOPHY

BY
GRANT PARKER GARNER

CHICAGO, ILLINOIS
DECEMBER 2017

Dedication Text

To my mother and father, none of this would have ever been possible without their love and the sacrifices they have made. I love you Mom and Dad.

Epigraph Text

If you can keep your head when all about you;
Are losing theirs and blaming it on you,
If you can trust yourself when all men doubt you,
But make allowance for their doubting too.
If you can wait and not be tired by waiting,
Or being lied about, dont deal in lies,
Or being hated, dont give way to hating,
And yet dont look too good, nor talk too wise:
If you can dream - and not make dreams your master;
If you can think - and not make thoughts your aim;
If you can meet with Triumph and Disaster,
And treat those two impostors just the same;
If you can bear to hear the truth you've spoken
Twisted by knaves to make a trap for fools,
Or watch the things you gave your life to, broken,
And stoop and build em up with worn-out tools:
If you can make a heap of all your winnings
And risk it on one turn of pitch-and-toss,
And lose, and start again at your beginnings
And never breathe a word about your loss;
If you can force your heart and nerve and sinew
To serve your turn long after they are gone,
And so hold on when there is nothing in you
Except the Will which says to them: Hold on!
If you can talk with crowds and keep your virtue,
Or walk with Kings - nor lose the common touch,
If neither foes nor loving friends can hurt you,
If all men count with you, but none too much;
If you can fill the unforgiving minute
With sixty seconds worth of distance run,
Yours is the Earth and everything thats in it,
And - which is more - youll be a Man, my son!

—Rudyard Kipling

TABLE OF CONTENTS

LIST OF FIGURES

LIST OF TABLES

ACKNOWLEDGMENTS

My education is a reflection of the support of my friends, family, and mentors, as the opportunities that I have been afforded are a direct consequence of the compassion and kindness of others.

My research was graciously funded by the Semiconductor Research Corporation, the Interuniversity MicroElectronics Center, and the National Science Foundation.

Thank you to the administration of the IME, especially Professor Matthew Tirrell, for providing such a welcoming atmosphere. Diana Morgan, Janet Boland, Novia Pagone, Rovana Papoff, and Sandra Marijan have gone above and beyond in providing the entirety of the IME with an incredible support system. The department's success depends on the dedication of these individuals.

My advisors, Professor Juan de Pablo and Professor Paul Nealey, provided me with a graduate career that I would call atypical. Living for extended periods of time in four different locations is not something that every graduate student is fortunate enough to experience. My life has been enriched by the cultures I have had the opportunity to experience and the relationships I have had the opportunity to foster due to these two men. Their support and guidance through this six year journey has given me the resources to forge a foundation on which to build a career. I am forever indebted to these men.

A perk of being co-advised by these two men, is the opportunity to work closely among an even larger collection of admirable individuals. Being able to work alongside Xuanxuan Chen, Jiaxing Ren, Paulina Rincon-Delgadillo, Lance Williamson, Robert Seidel, and Moshe Dolejsi of the Nealey group has been an honor. Their knowledge and expertise has been as much of a boon to my own development as it has been humbling.

There is much to be said of those that are members of the de Pablo group as well. A group that has become a second family for me. I entered into the group with Josh Lequieu and Lucas Antony. They have been, without a doubt, two of the most genuinely kind individuals that I have had the fortune of meeting. I believe their dedication to excellence

and generosity will lead them to great successes, and I am proud to have grown with the two of them. In addition to the brothers that I joined with, I have found inspiration and guidance from my seniors in the group. Su-mi Hur, Abelardo Ramírez-Hernández, Jian Qin, Johnathan Whitmer, and Arnout Boelens have provided me with nothing but support and kindness throughout our time together. The younger members of the group, Cody Bezik, Emre Sevgen, Josh Moller, Ashley Guo, and Daniel Reid teach me so much, so frequently, I often forget that I am their senior. I must also thank Aaron Fluitt and Kyle Hoffman; I do not believe there has ever been an instance where they have denied to offer a helping hand. More than once have I benefited from their kindness. Honestly, Professor de Pablo provides an environment that draws in incredible individuals, and I am lucky to have been able to benefit from their presence. This group, this family, is everything I didn't know that I wanted from my graduate career.

In addition, I must mention three men in particular: Alec Bowen, Brandon Peters, and Gurdaman Khaira. I know that I have been spoiled by the opportunity to work in the Block Copolymer subsection of the de Pablo group with these men. The friendship that spawned from the TICG model is something that I most proud of from the past six years. I would just like to thank the three of you for teaching me and allowing me to be your friend.

I mentioned that I have spent long periods of time in four locations throughout my graduate career. Those were Madison, Wisconsin, San Jose, California, Chicago, Illinois, and Leuven, Belgium. I would like to thank Azat Latypov of GLOBALFOUNDRIES and Roel Gronheid of imec for allowing me the opportunity to take part in internships under their supervision.

I must thank three of my previous teachers as well: Heidi Downs, Ashley Hobson, and Billy Jones. I believe they instilled in me the determination and confidence to chase my goals, and i find myself privately thanking them for all the sacrifices they made for me as an adolescent.

I want my brothers and sisters, Laura Peresta, John Findley, Josh Peresta, and Angel

Findley, to know that their love is never forgotten and that I cherish their support.

My gratitude to my mother, Deb Garner, and my father, Steve Garner, knows no limit. Throughout my life they have provided me with everything that they could afford: time, money, love, I have never had to want for anything of that sort, and I want them know that I realize how lucky I am.

And finally to the love of my life. Thank you Carmen, for filling my life with love, for challenging me on a daily basis to improve, and for helping me continue to grow. You are constant source of motivation and support. Te quiero, para siempre.

ABSTRACT

The directed self assembly of block copolymers is an exciting complimentary technique for the fabrication of nanoscale structures for lithographic applications. Typically a directed self assembly process is driven through substrates with chemical (chemoepitaxy) or topographical (graphoepitaxy) guiding features. These patterning strategies have led to the ability to assemble structures with a high degree of perfection over large areas. However, a guiding pattern has not been created which assembles the desired features with a defect density that is commensurate with industrial standards of 1 defect/$100cm^2$. This work focuses on using molecular simulations on the Theoretically Informed Coarse Grained model to provide design rules for substrate patterns which drive the assembly of desired, device-oriented morphologies.

Prior to the work presented in Chapter 2, the TICG model has been used in conjunction with a chemical pattern that is approximated as a a hard-impenetrable surface. As many experimental systems use polymer brushes to help guide the polymer melt deposited on the substrate, this work analyzes the consequences of such an assumption by comparing a model where the polymer brush is explicitly implemented to the hard-wall substrate used in the past. Then, a methodology which utilizes a evolutionary optimization method is used to map the parameters of the more detailed model to the hard-surface model. This provides a qualitative understanding of how to interpret the model parameters used in previous works in the context of real experimental pattern designs.

Chapter 3 discuss the concept of competitive assemblies in regards to defining a thermodynamic processing window in design space for assembling lines-and-spaces. The most competitive assembly to the desired orientation of the lamella is defined as a rotation of assembled lamella to the underlying pattern. Thermodynamic integration is used to calculate the free-energy difference between these assemblies over chemical patterns with varied design parameters. Local maximums in the free-energy difference are observed over pattern designs that are in qualitatively agreement with the pattern designs which produce the most

perfect assemblies in experiments. The analysis is extended to study how choice of chemistry impacts this thermodynamic selection for the desired morphology.

Finally, Chapter 4 provides insight into the kinetics of patterned directed self-assembly by investigating cylinder forming block copolymers within cylindrical confinements. Through the use of the string method, the minimum free-energy path between a defective state and the desired assembled morphology is calculated and clear transition states are highlighted. The effects of key parameters of the confinement design on the calculated minimum free energy path are calculated to identify design rules which should lead to a better understanding of optimal confinement design for eliminating defects. In addition, a specific modification to existing cylindrical confinements is discussed as a possibility for tackling the problem of placement accuracy for a cylinder that is assembled within the confinement.

CHAPTER 1

INTRODUCTION

Block copolymers are a class of macromolecules composed of two or more homopolymer subunits that are connected through a covalent bond. In the case of diblock copolymers, there are only two subunits. These materials have been shown to spontaneously microphase separate into a number of morphologies, most notably spheres, cylinders, and lamella, with length scales on the order of tens of nanometers.[1] The equilibrium morphology is a result of the competition of entropic and enthalpic interactions. The entropic effects are governed by the chain stretching and packing, while the enthalpic interactions are governed by the chemical incompatibility of the two blocks, measured by the Flory Huggins parameter.[2] The chemical incompatibility leads to phase separation, while the chain connectivity limits the distance over which the materials can separate from one another. Without the two species being connected, they would macrophase separate. [3] In addition, if the block copolymer is deposited as a thin-film onto a substrate, or into a confinement, the boundary conditions of the surface impact the resulting equilibrium morphology.

The material volume fraction, the degree of polymerization, and the chemical incompatibility are intrinsic characteristics of the block copolymer that can be leveraged alongside factors extrinsic to the material, such as substrate design, to direct the assembly of the block copolymer into desired morphologies. Having numerous design parameters allows for the ability to create various shapes of tunable size. This has made block copolymers an attractive candidate for nanoscale fabrication in recent years.

In nanolithography applications, the current state-of-the-art fabrication facilities utilize 193nm immersion lithography tools. The directed self-assembly of block copolymers offers a cost-effective solution to access similar, or smaller, length scales, for creating dense arrays of device oriented structures for future microelectronics. However, industrial standards demand that fabrication processes must have defect rates of lower than 1 defect/$100cm^2$. Therefore, eliminating the existence of defects when assembling desired structures is critical to the

success of the directed self assembly of block copolymers for industrial application. Chemical patterns[4–7], shear flow[8–13], graphoepitaxy [14, 15], and solvent annealing[16] have all proven to be methodologies that have the ability to drive long range order of the DSA process. However, a process has not been developed which can meet the industrial defect requirements. To understand the effects of pattern design on the DSA process, I perform Monte Carlo simulations with a Theoretically Informed Coarse Grained model for block copolymers to provide useful design rules for DSA processes.

In the second chapter, I present an analysis of a common assumption made when using molecular simulations to study the DSA of BCPs in thin-films. All previous work done with the TICG model has assumed that the polymer-substrate interface can be approximated as the polymer melt interacting with a hard, impenetrable wall.[17, 18] The chemical patterns are calculated through fast-decaying potentials. This assumption is demonstrably different than experimental setups, where the polymer melt that is being assembled is often interacting with soft polymer brushes, as the chemical patterns consist of random copolymer brushes that provide the necessary chemical contrast to drive the assembly process.[19] In order to better understand how the TICG model maps to experimental systems, we implement a guiding pattern that is composed of explicit polymer brush molecules. A methodology is proposed for mapping this explicit model to the more common implementation of the hard, impenetrable wall with the implicit potential. This mapping is beneficial as it provides heuristics for understanding the results of the simpler, more computationally efficient model. and allows for better understanding of the esoteric parameters that govern the implicit potential. In addition, evolutionary optimization techniques are used to demonstrate that equivalent equilibrium morphologies can be assembled using both substrate models.

In the third chapter, we shift the focus to understanding how free-energy relationships between competitive morphologies can be controlled through pattern design. We focus on systems that produce lines-and-spaces. It is well-established by theory and experiment that lamella forming block copolymers with characteristic periodicity, L_0, can assemble lines-and-

spaces over carefully crafted chemically patterned substrates comprised of stripes of width W that repeat with period L_S. Where as previous works measured the efficacy of pattern designs for self-assembly through visual inspection of experimental images or examination of morphologies obtained from simulations, here we combine visual inspection over a large number of processing conditions with a new theoretical strategy that quantitatively measures the thermodynamic driving force of chemical patterns to produce a single grain of lines-and-spaces. The metric we use to describe the thermodynamic driving force is defined by the free-energy difference between the desired assembly of lines-and-spaces and the grain orientation with the lowest energy, referred to as the most-competitive assembly. Visualization of experimental systems using SEM-imaging provides a first-order approximation of the process windows in pattern design space in regards to W and the chemical contrast of the stripe and the background region, where the thermodynamic driving force is large enough to eliminate competitive grains. The strategy proposed in this work then uses complimentary molecular simulations to elucidate which combination of these pattern parameters provides the largest driving force through free-energy calculations obtained by thermodynamic integration and attempts to identify which pattern designs minimize the probability of assembling lamella that are stabilized at undesired angles to the patterned stripes. The combination of experiment and theory shows that narrow guiding stripes with width $0.4 \leq W/L_0 \leq 0.8$ that are highly preferential for one of the blocks are best for obtaining a directed self-assembly process flow with the highest probability of assembling a desired grain orientation.

Finally in the fourth chapter, we investigate the directed self-assembly of block copolymers in cylindrical cavities or holes is a promising technology for lithographic patterning, particularly in the context of vertical interconnect accesses. While the so-called hole-shrink process for single cylinders has been extensively explored, a number of challenges remain related to morphological defects and placement accuracy. In this work, we use theory and simulations to systematically explore the metastable morphologies that form within cylindrical confinements for different combinations of the interfacial energy between the polymer

and the bottom and sidewall of the confining holes. We identify a set of well-defined defective morphologies, in addition to the desired cylindrical morphology, in geometries where the sidewall is wet by the majority block. By relying on coarse-grained simulations of model polymers, coupled to a string method in collective variables, we identify transition pathways between defective morphologies and the sought after cylindrical morphology to elucidate the mechanism of defect annihilation within the confinements considered here. In addition, the string method is also used to identify the formation of the desired morphology from a disordered state. This work provides evidence that the minimum free energy path for the formation of a cylinder goes through transition states that consist of defective morphologies, and that proper design of confinement can help eliminate these undesirable transition states in the underlying pathway. This work demonstrates the importance of controlling the chemistry of the sidewall within single-hole confinements as it relates to increasing the probability of defect annihilation.

CHAPTER 2

MODELING POLYMER BRUSHES IN CHEMOEPITAXIAL PATTERNS: A COMPARISON OF TWO SUBSTRATE MODELS FOR MODELING THE DIRECTED SELF-ASSEMBLY OF BLOCK COPOLYMERS IN THIN-FILMS

2.1 Introduction

Block copolymers can assemble into numerous device-oriented morphologies that are useful for lithographic fabrication of integrated circuits.[20] The directed self-assembly of these molecules on chemically or topographically patterned substrates provides a strategy to control the assembly process.[4–7] Molecular models have provided qualitative and quantitative descriptions of the DSA process, primarily through simulations and self-consistent field calculations.[14, 17, 18, 21, 22]

The Theoretically Informed Coarse Grained (TICG) model, in particular, has been used extensively to understand the self-assembly of a number of materials into ordered thin-film morphologies. [17, 23] The model has elucidated the three-dimensional shape of assemblies over patterned surfaces, demonstrating that the top-down view of an assembly does not provide adequate information about the uniformity through-film.[21] It has been instrumental in detailing the equilibrium relationship between desired assembled morphologies and defects, namely dislocation-type defects.[24] The model has even been used in tandem with evolutionary optimization strategies to identify optimal design parameters for desired, device-oriented structures.[20] These optimization strategies have also been used in conjunction with x-ray scattering to provide information regarding three-dimensional structure from X-ray data.

The body of work mentioned above has always approximated the patterned surfaces as a hard, impenetrable walls, where the surface-polymer interaction is modeled by a fast-decaying Gaussian potential. However, in a wide range of experiments, the surface that

the block copolymer is deposited onto is in fact coated with a polymer brush.[19] These soft surfaces allow for the interpenetration of the block copolymer, and the question that arises is whether a hard surface is a reasonable approximation to a polymer brush and, if so, what is the appropriate mapping required to establish a correspondence between results for polymer brushes and hard walls.

In this study, we consider the assembly of symmetric diblock copolymers on stripe-patterned substrates. We consider a density multiplication strategy under which sparse stripes, coated with explicit polymer brushes, are used to direct the assembly of a block copolymer thin film. A genetic optimization strategy is used to parameterize the fast-decaying Gaussian potential model that best matches the more realistic design parameters that correspond to an explicit polymer brush pattern. The results of this parameterization indicate that an effective mapping can be devised to translate results from detailed (explicit brush) models of the patterned substrates onto simpler, hard-wall representations while retaining the ability to capture the films three-dimensional equilibrium morphology.

2.2 Simulation Model

The simulation results presented here are based on the standard coarse-grained model for block copolymers. Previous work used this model to elucidate the morphological behavior of block copolymer films on chemically and topologically patterned substrates. In general, the results from model calculatuions have been found to be consistent with experimental observations. In this model, polymer molecules are represented by flexible, linear Gaussian chains discretized into N beads, where the position of the s^{th} bead in the i^{th} chain is given by the vector $r_i(s)$. A system comprises n AB copolymer molecules in a fixed volume V at a fixed temperature T. The Hamiltonian $H = H_b + H_{nb}$ of the system includes the interactions between bonded beads (b), as well as non-bonded interactions(nb). The connectivity of

neighboring beads in a polymer chain is described by:

$$\frac{H_b[\{\mathbf{r}_i(s)\}]}{k_BT} = \frac{3}{2b^2}\sum_{i=1}^{n}\sum_{s=1}^{N-1}[\mathbf{r}_i(s+1)-\mathbf{r}_i(s)]^2 \tag{2.1}$$

where k_b is the Boltzmann constant, $b^2 = R_e^2/(N-1)$ is the mean-squared bond length, and R_e^2 is the mean-squared end-to-end distance of an ideal chain. Non-bonded interactions are described by

$$\frac{H_{nb}[\phi_A,\phi_B]}{k_BT} = \frac{\sqrt{\overline{N}}}{R_e^3}\int_V d\mathbf{r}[\chi_{AB}N\phi_A\phi_B + \frac{\kappa N}{2}(1-\phi_A-\phi_B)^2] \tag{2.2}$$

where $\sqrt{\overline{N}} = \frac{\rho_0 R_e^3}{N}$ represents the invariant degree of polymerization, which is proportional to the polymer's molecular weight in a dense melt, and where ρ_0 is the bead number density. The local dimensionless density ϕ_K of species $K = A, B$ is computed using the configuration of the polymer beads relative to a lattice with spacing ΔL using a zeroth order particle-to-mesh interpolation scheme. [17] The incompatibility between unlike species is measured by the Flory-Huggins parameter, $\chi_{AB}N$; the inverse isothermal compressibility, κN, gives the polymer melt a finite compressibility.

Monte Carlo (MC) simulations are used to identify possible self-assembled morphologies over distinct chemical patterns. Configurations are sampled according to Metropolis criteria, where the probability of accepting a trial configuration is given by $P_{acc} = \exp(-\Delta H/(k_BT))$, and where ΔH represents the energy difference between the original and proposed configuration. Trial configurations are produced using four different Monte Carlo moves: single bead displacement, translation of a chain, chain reptation, and chain inversion.

The lattice for computing local densities is defined such that the average number density of beads in any cell is $n_{int} = 14$. To model the self-assembly of a block copolymer thin film, the polymer is confined between two impenetrable walls normal to the z-axis of the simulation box, while periodic boundary conditions are applied in the x and y dimensions

of the box. The top wall at $z = L_z$ is considered neutral, whereas the bottom wall at $z = 0$ mimics the chemically patterned substrate on which the block copolymer assembles. In this work, two possible models are presented to represent this bottom, chemically patterned surface. In each model, the underlying chemical pattern is composed of repeated stripes of width W that have a period L_S. The area between stripes is referred to as the "backfill" region. The x-dimension of the simulation box has length PL_S, where P is a positive integer. However, one model explicitly includes the polymer brush, while the other approximates the surface as a hard surface with interactions described by an implicit field.

2.2.1 Gaussian Potential Model

The first model, which utilizes a Gaussian potential to approximate the surface interactions has been described in the literature. The hamiltonian is extended to $H = H_b + H_{nb} + H_s$, where the substrate interaction is denoted by H_s. The interaction between the substrate and polymer is modeled by a one-body potential acting on each bead:

$$\frac{U_S(\mathbf{r}_i, K_i)}{k_B T} = \frac{\Lambda_{K_i}(x, y)}{N} d_s \exp(\frac{-z^2}{2d_s^2}) \tag{2.3}$$

where d_s governs the range of the interaction and z is the distance between the polymer bead and the substrate along the axis normal to the substrate. The total contribution of the substrate-polymer interaction to the Hamiltonian is

$$\frac{H_s}{k_B T} = \sum_{i=1}^{nN} U_S(\mathbf{r}_i, K_i). \tag{2.4}$$

Here, $\Lambda_K N$ represents the strength of the interaction between polymer beads of type $K = A, B$ located at (x, y) and the substrate. The functional form of $\Lambda_K N$ depends on the geometry of the chemical pattern. The guiding stripes' strength of interaction with the polymer is denoted by $\Lambda_S N$ and the backfill interaction by $\Lambda_B N$. A larger value of $\Lambda_S N$

indicates a greater affinity of the stripes for the A-type polymer, whereas a larger value of $\Lambda_B N$ indicates a greater affinity of the backfill for the B-type polymer.

2.2.2 Explicit Brush Model (EBM)

In the second model, brush molecules are anchored to the bottom surface of the simulation box. The brush molecules are represented at exactly the same level of description as the thin film copolymer molecules. Brush molecules have a grafting density B_D [chains/R_e^2], and a molecular weight of $M_b N$, where M_b is the ratio of the molecular weight of the brush molecules relative to the polymer melt. In each simulation of a chemical pattern, two classifications of brush molecules are used; a brush for the guiding stripe and a brush for the backfill region. Each brush has the same grafting density and molecular weight ratio; however, the composition of each brush class is different, and represented by $f_{V,A}$, which is the fraction of brush class V (where V is either guiding stripe, GS, or backfill, BF) comprising beads of species A. The composition of bead species B is $f_{V,B} = 1.0 - f_{V,A}$. The random block copolymer brushes were consist of a random sequence of beads, where each bead has a probability $f_{V,A}$ of being A-type; otherwise, the bead would be B-type. The interfacial energy between the random copolymer brushes and the block copolymer is governed by these compositions.

Each brush molecule is anchored to the bottom wall of the simulation box, where z=0. A random pair of coordinates x,y serves to specify each anchoring position. Any brush molecule that is anchored at an x-position within $[QL_S, QL_S + W]$, where Q is a integer that satisfies $0 \leq Q < P$, is considered to be of the guiding stripe brush class. Otherwise, the brush molecule is considered to be a part of the backfill. Brush chains interact with the polymer melt through the non-bonded potential described above, and their connectivity is maintained through the bonded potential.

2.3 Results

In this work, several key parameters of the TICG model are kept constant, at values that have been shown in previous work to be consistent with experimental observations. These parameters are the chain discretization of the block copolymer, N, the interdigitation number, $\sqrt{\overline{N}}$, and the isothermal compressibility, κN^{-1}, mentioned in the Methods section. A value of $N = 50$ was chosen for discretization, as it allows for a reasonable representation of polymer brush molecular weights in the EBM. The other two parameters are chosen to be $\sqrt{\overline{N}} = 83$ and $\kappa N = 22$, to be consistent with previous work.[25]

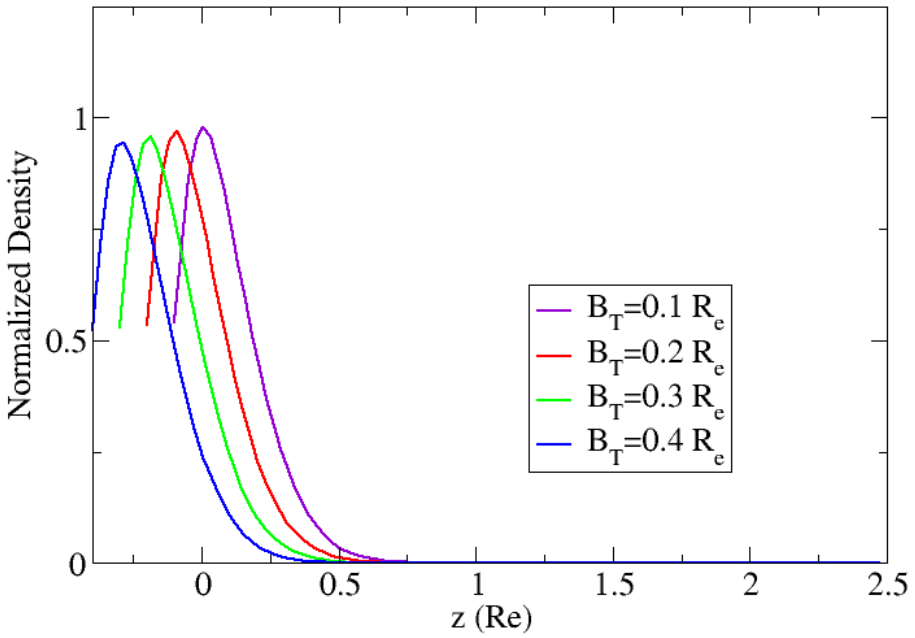

Figure 2.1: The normalized number density of polymer brush beads calculated from simulations of the Explicit Brush Model as a function of distance z from a substrate located at $z = -B_T$ within a thin film that is $[2.5 + B_T]R_e$ thick. Simulation results of four different values of B_T are shown here, where all other simulation parameters are held constant. The brush grafting density is $B_D = 125$ [chains/R_e^2], and the ratio of the molecular weight of a brush molecule to a molecule in the polymer melt is $M_b = 0.2$.

Attaching brush molecules to the surface of the substrate leads to a compression of the

polymer melt; additional volume must be added to the simulation box in order toaccommodate the excess brush beads. The necessary thickness that must be added to the thin film to accommodate the brush material is a function of the chosen grafting density, B_D, and the molecular weight M_bN of the brush molecules. For the Explicit Brush Model (EBM), once the grafting density B_D and the molecular weight ratio M_b are specified, several simulations can be performed at various thicknesses in order to establish a correspondence with results for the hard surface model. For concreteness, we chose a reference thickness that governs the amount of polymer in the simulation box for each simulation; for this work, we chose $2.5R_e$. This means that $2.5L_xLyN\sqrt{\overline{N}}$ beads are used for the polymer atop the brush. The thickness of the confinement is therefore $2.5 + B_TR_e$; in this work, we simulate thicknesses where B_T is in the range of $[0.0, 1.0]R_e$. The polymer and brush consist of only A-type beads in order to remove the enthalpic interactions in the simulations. Figure 2.1 shows the normalized number density of brush beads as a function of distance z from the hard surface, where $z = -B_T$ corresponds to the location of the substrate and B_T is the thickness added to the simulation box. The number density is normalized by the bulk density of the polymer melt in the TICG model, which is $\rho_0 = \frac{\sqrt{\overline{N}}}{N}R_e^3$. The brush density curves generated for different thicknesses are similar; each shows a depletion layer near the surface and a peak in density, followed by a sharp decrease. The peak heights follow intuition; they are slightly higher for thinner films, as the volume is smaller with the same quantity of material, leading to more compression. Figure 2.2 shows the density profile of the polymer melt within films of different thicknesses. The same trends observed for the brush profile are seen for the polymer melt, with thinner films leading to higher compression. Examination of Figures 2.1 and 2.2 reveals that there is significant interpenetration between the brush and the polymer melt. In order to determine which thickness is most appropriate to carry out a comparative study of the two surface models, we compare the density profiles of a homopolymer melt over an explicit brush to the density profile obtained from the TICG model in the absence of a brush or an interfacial potential.

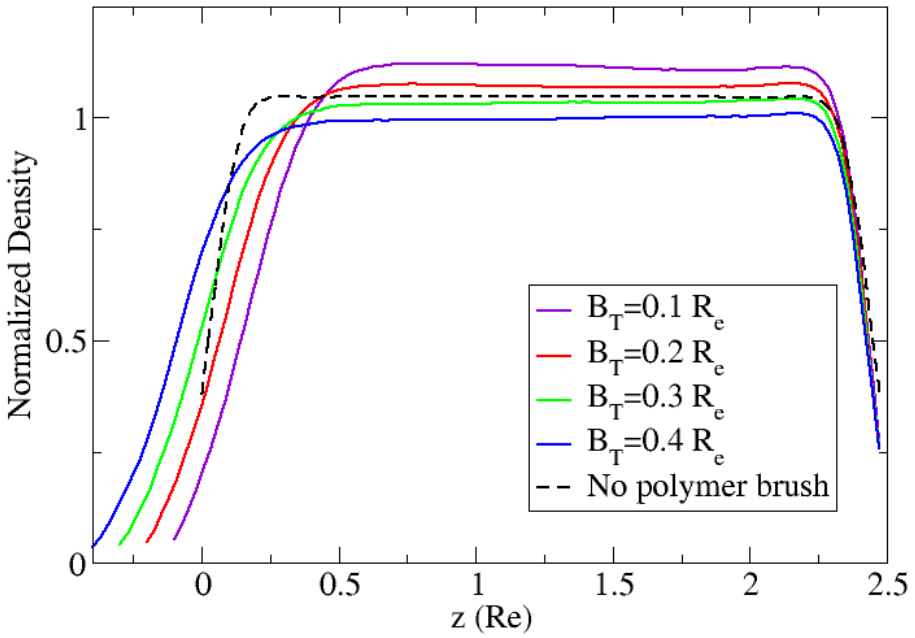

Figure 2.2: The normalized number density of polymer melt beads as a function of distance z from a substrate located at $z = -B_T$ within a thin film that is $[2.5 + B_T]R_e$ thick. Simulation results of four different values of B_T are shown here for the simulations of the Explicit Brush Model, where all other simulation parameters are held constant. The brush grafting density is $B_D = 125$ [chains/R_e^2], and the ratio of the molecular weight of a brush molecule to a molecule in the polymer melt is $M_b = 0.2$. The dotted black curve represents the density profile of the polymer melt within a $2.5R_e$ thick film, which was calculated using the Gaussian Potential Model. The normalization factor is $\rho_0 = \frac{\sqrt{\overline{N}}N}{R_e^3}$, where $\sqrt{\overline{N}} = 83$ and $N = 50$.

Figure 2.2 shows the average density profile in the dimension normal to the hard surface for beads confined in a slit of thickness $2.5R_e$. As expected, a depletion layer is observed in the vicinity of the hard surfaces. Far away from the surface, an equilibrium normalized density is attained. The equilibrium normalized density in the thin-film ρ_{TF} is defined as the mean of all values of $\phi(z)$ where $\frac{\delta}{\delta z}\phi(z) = 0$. In order to model the same physical system when using an explicit brush, we must choose a value of B_T for the EBM such that far away from the brush-melt interface, the polymer melt has the same ρ_{TF}. The value of B_T for a given combination of B_D and M_b that is used for our simulations corresponds to the

condition where $\Delta E^2 = (\rho_{TF,EBM} - \rho_{TF,GPM})^2$ is minimized.

Figure 2.2 shows the local density profile for a series of B_T with $B_D = 125$ chains/R_e^2 and $M_b = 0.2$. In Figure 2.2, the portion of the x-axis that is below zero is equivalent to the added thickness. The hard wall that the brush is anchored to is located at tR_e in the dimension normal to the confining walls. The change in the density profile of the polymer melt is satisfies intuition for changing B_T; we see that brush takes up space and compresses the polymer melt until more volume is added to the simulation box. This is true until too much volume is added, and the volume filling nature of the TICG model causes the polymer to be too disperse in the EBM when compared with the GPM. In addition, the depletion layer is wider when an explicit brush is present, as there is considerable interpenetration of the polymer belt into the brush. The reverse is also true (interpenetration of the brush into the melt), as can be appreciated in the plot of the brush bead local density in Figure 2.1.

The thickness B_T where ΔE^2 is minimized is of interest for design of a suitable reference EBM. Figure 2.3 shows the value of ΔE^2 as a function of B_T for a series of grafting densities and a $M_b = 0.2$. The value of M_b is fixed at 0.2 as it is a common molecular weight ratio for the polymer brush to the polymer melt used in DSA experiments over chemical patterns with brushes. This analysis can easily be extended to other molecular weight brushes. Figure 2.3 shows that each grafting density requires a different B_T to achieve $\Delta E^2 = 0$. Higher grafting densities require a thicker film to accommodate the increased total mass of the system that corresponds to a higher number of brush beads.

Using this approach, we are able to specify which simulation box to use with a polymer brush anchored to one of the confinement walls in order to mimic DSA in thin films over guiding brushes. For a desired combination of B_D and M_b we can find the corresponding B_T through a series of short simulations of homopolymers. For $B_D = 125$ chains, $/R_e^2$, $M_b = 0.2$, and the optimal value for the thickness is $B_T = 0.25$ as shown in Figure 2.3. As we transition to represent DSA over chemical patterns, the design properties of the chemical pattern must be specified. This work focuses on equilibrium lines-and-spaces formed from

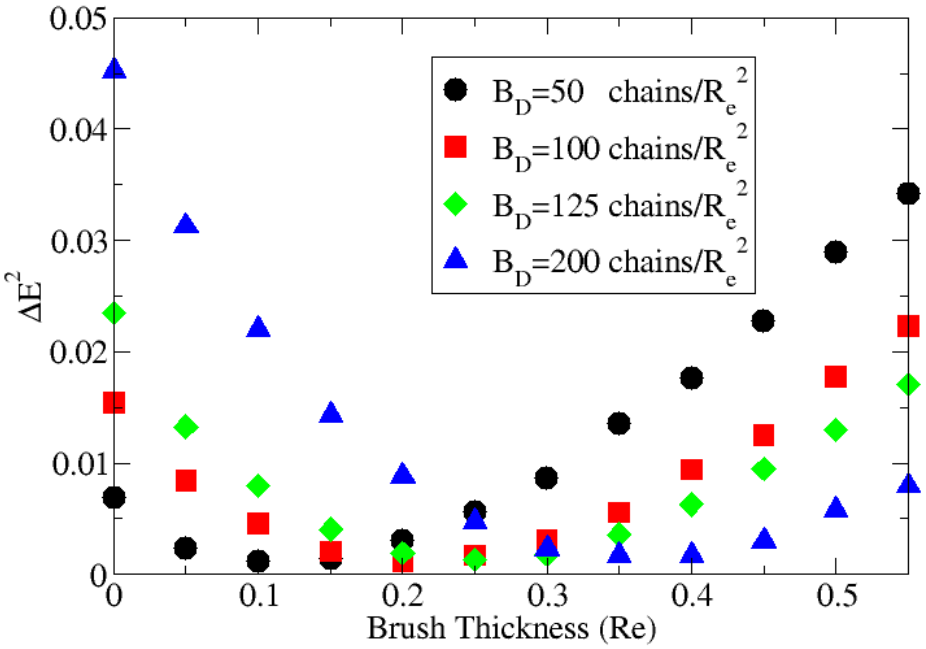

Figure 2.3: The squared difference, ΔE^2, of the normalized thin film density of a homopolymer which is calculated using the Explicit Brush Model within a film of thickness $[2.5 + B_T]R_e$ and the Gaussian Potential Model within a film of thickness $2.5R_e$. The parameters describing the polymer melt are the same in all simulations used: $\sqrt{\overline{N}} = 83.0$, $n_{int} = 14.0$, $\kappa N = 22.0$, and $N = 50$. A series of calculations of ΔE^2 at different brush thicknesses, B_T, are shown for four different brush grafting densities, B_D. In all simulations of the Explicit Brush Model used in in this plot, the ratio of the molecular weight of a brush molecule to a molecule in the polymer melt is $M_b = 0.2$

symmetric lamella-forming block copolymers with fraction $f_A = 0.5$. A typical density multiplication pattern is considered where guiding stripes of width W/L_0 are separated by a pattern periodicity L_S with a backfilled region of width $L_S - W$. The guiding stripe anchors homopolymer brush of type A, and is therefore preferential for the A-species of the diblock copolymer. The backfill region anchors random copolymer brushes comprising both A and B type beads. Changing the composition of the backfill brush allows for control of interfacial energy between the brush and polymer melt.

In order to supplement the less detailed description of the patterning surface in the

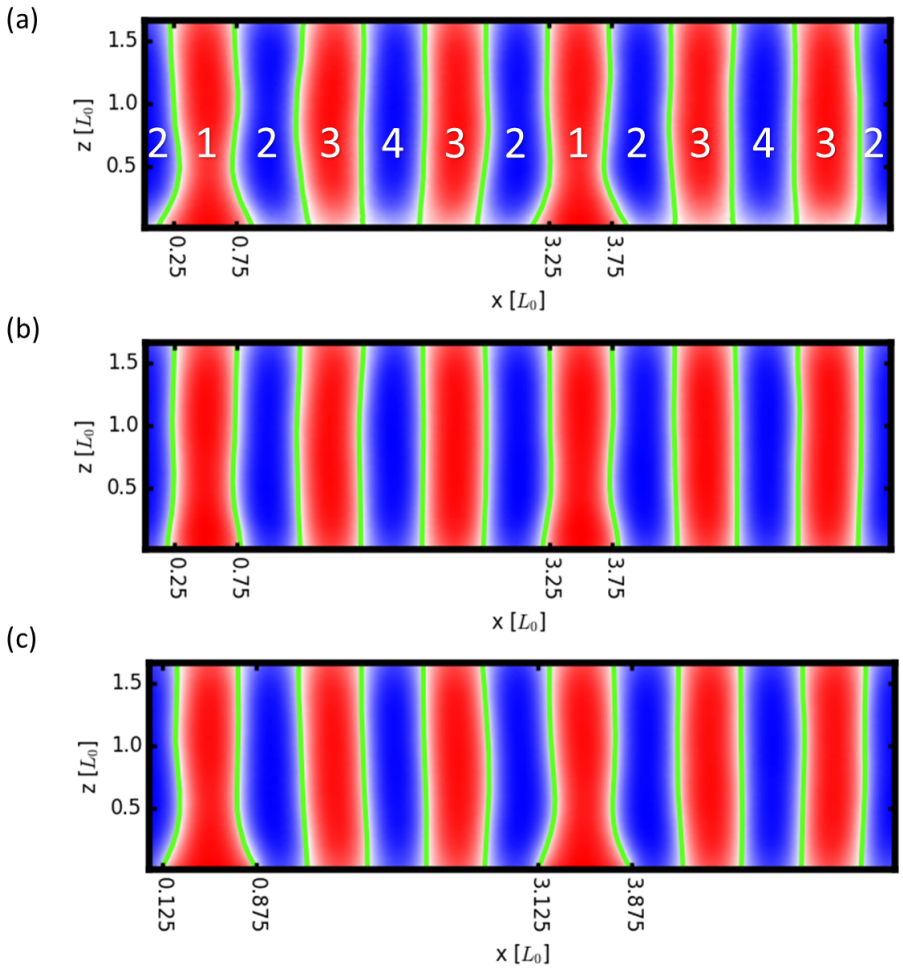

Figure 2.4: Average two-dimensional equilibrium morphologies. The red domains represent the block copolymer domain, which is guided by the guiding feature, and the blue domains are comprised of the unguided block. The domains are labeled between 1 and 4 to identify the number of unique domains which exist atop a 3X density multiplication pattern with a guiding feature with width $W/L_0 < 1.0$. The tick marks on the horizontal axis represent the bounds of the guiding features within the simulation box. a) The morphology captured from a simulation of the Explicit Brush Model, with $W/L_0 = 0.5$, $f_{V,A} = 0.5$, $B_T = 0.25$, $B_D = 125$ chains/R_e^2, and $M_b = 0.2$. b) The morphology captured from a simulation of the Gaussian Potential Model with $W/L_0 = 0.5$, $d_s = 0.15$, $\Lambda_S N = 0.75$, and $\Lambda_B N = 0.00$. c) The morphology captured from a simulation of the Gaussian Potential Model with the optimized parameters to match the simulation in subset a) of $W/L_0 = 0.75$, $d_s = 0.07$, $\Lambda_S N = 0.945$, and $\Lambda_B N = -0.004$.

Gaussian Potential Model (GPM), the EBM is used to define an expected morphology for a certain brush composition. Once the polymer brush thickness and chemistry are specified, the expected morphology for a chemical pattern can be obtained from a series of Monte Carlo simulations. The morphology is defined using the density order parameter $\Phi(\mathbf{r}) = \frac{\phi_A(\mathbf{r})-\phi_B(\mathbf{r})}{\phi_A(\mathbf{r})+\phi_B(\mathbf{r})}$, where a positive value of $\Phi(\mathbf{r})$ designates an A-rich location, and a negative value designates a B-rich location for both models. By averaging $\Phi(\mathbf{r})$ along the y-dimension, the morphology can be collapsed into a two-dimensional slice of the average morphology in the xz plane. The iso-curve, $I(z)$, where $\Phi(\mathbf{r}) = 0$ then defines the average interfacial profile. Using the interfacial profile, the width of each lamellar domain within the simulation box can be calculated as a function of height in the film. In the EBM, only the polymer above height B_T is used to generate the morphology, as this is the equivalent volume used in the GPM. Figure 2.4a provides an example of the collapsed two-dimensional morphology, where green curves are used to show the location of the iso-curves.

Figure 2.4b shows the two-dimensional morphology that arises in a GPM simulation, where the pattern parameters are chosen to "naïvely" mimic the EBM. In the case in Figure 2.4b, we chose the guiding stripe width to be $W/L_0 = 0.5$ in order to match the width of the area that anchors the stripe brush, and $\Lambda_B N = 0.00$ in order to mimic the $50:50$ backfill brush in the EBM simulation shown in Figure 2.4a. In addition, the guiding stripe strength is chosen to be $\Lambda_S N = 0.75$, and the range of interaction is set to $d_s = 0.15$ in order to be consistent with previous works.[17, 25] There is a distinct difference in the guided domains corresponding to the two cases; a simple optical inspection of the image shows that the GPM model underestimates the structural perturbation induced by the patterned stripe.

By comparing the average domain widths predicted by simulations of each model, we are able to quantify the most salient differences. By considering a variety of parameter combinations for the GPM, a specific substrate potential can be identified that best approximates the profiles corresponding to the more detailed brush model. The key parameters in the GPM are the range of interfacial interaction, ds, the strength of the interfacial interactions,

$\Lambda_S N$ and $\Lambda_B N$, and the width of the guiding stripe, W/L_0. All patterns considered here correspond to a 3X density multiplication scheme, which means that there is one feature on the patterned surface for every three lamella created by the block copolymer.

This work focuses on patterns consisting of relatively thin guiding stripes, $W/L_0 = [0.2, 1.0]$, due to the fact that the stable morphology over these patterns consists of only a single A domain over the guiding feature. Wider stripes, approximately $1.5L_0$, stabilize two A domains over the stripe that often become connected through a wetting layer. This makes the comparison of the iso-curves less transparent. Also, by limiting the simulations to only the case of thin stripes, there are four domain types that must be accounted for, instead of six. This is due to the symmetry of the periodic assemblies. These four unique domains are labeled according to their location in Figure 2.4. The first domain sits centered on the guiding stripe and is A-rich. The second domain is B-rich and is directly adjacent to the guiding stripe. The third domain is A-rich and is located over the backfill brush. The final, fourth domain is centered over the backfill brush.

All simulations for the remainder of the paper focus on a brush with grafting density $B_D = 125$ chains$/R_e^2$, and with relative molecular weight $M_b = 0.2$, as these conditions represent well the brushes used in experiments. The domain widths as a function of distance from the surface-brush interface are plotted in Figure 2.5 for a pattern with $W/L_0 = 0.5$ and a backfill brush composition of $f_{A,BF} = 0.5$. As the domains get far away from the interface, their width returns to the average bulk domain value; however, there are perturbations near the interface as a result of the interaction between the polymer melt and the brush pattern. The most prominent of the perturbations seen in Figure 2.5 occurs over the first domain type, which is centered over the guiding stripe. The width of this domain near the brush interface is much greater than the bulk width, and much greater than the width of the area which has the A-type brush anchored to it. This indicates that some A-type polymer brush chains extend not only up through the film but also horizontally into the neighboring random copolymer brush, causing an A-preferential region that is much larger

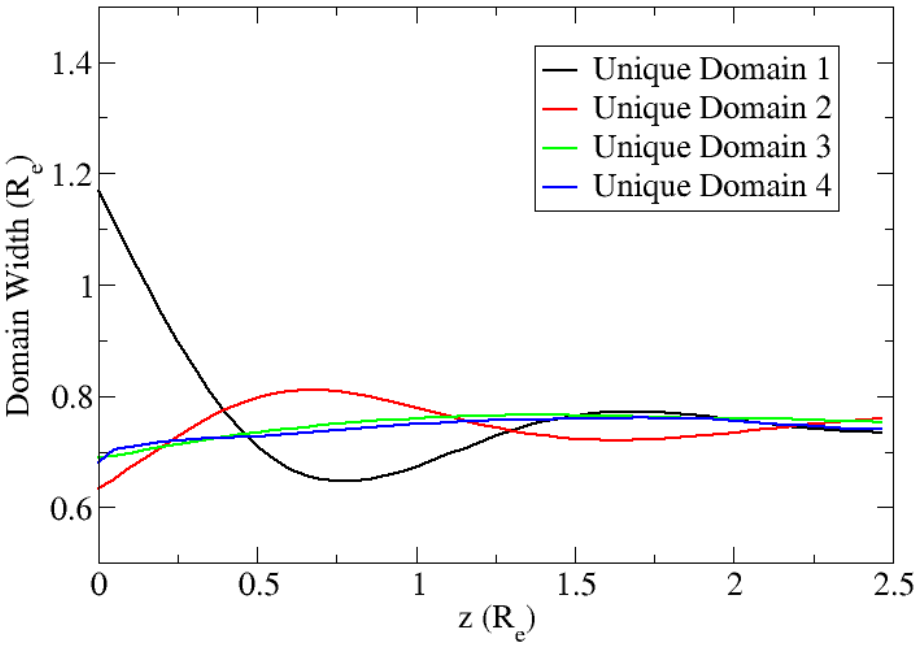

Figure 2.5: The average domain width of each unique domain shown in Figure 2.4a. The width is plot as a function of distance from $z = 0.0$ within the thin film.

than the design anticipates. The domain narrows before it returns back to approximately a bulk spacing. The second unique type of domain, adjacent to the guiding stripe domain, is compressed near the brush due to the extreme stretching of the domain over the stripe. The other two domains are slightly narrower than the bulk spacing near the pattern; however, the perturbation is not as pronounced. This is also due to the stretching of the domain over the stripe, because the neutral brush in this simulation should not exhibit a preference for either of the species, as $f_{A,BF} = 0.5$.

The same set of iso-curves can be produced with the GPM. The square difference can then be integrated over the film height. This integral can be calculated for each of the four unique domains in order to create a similarity measurefor the two morphologies obtained for the different models. The fitness function to describe the sameness of two assemblies can be

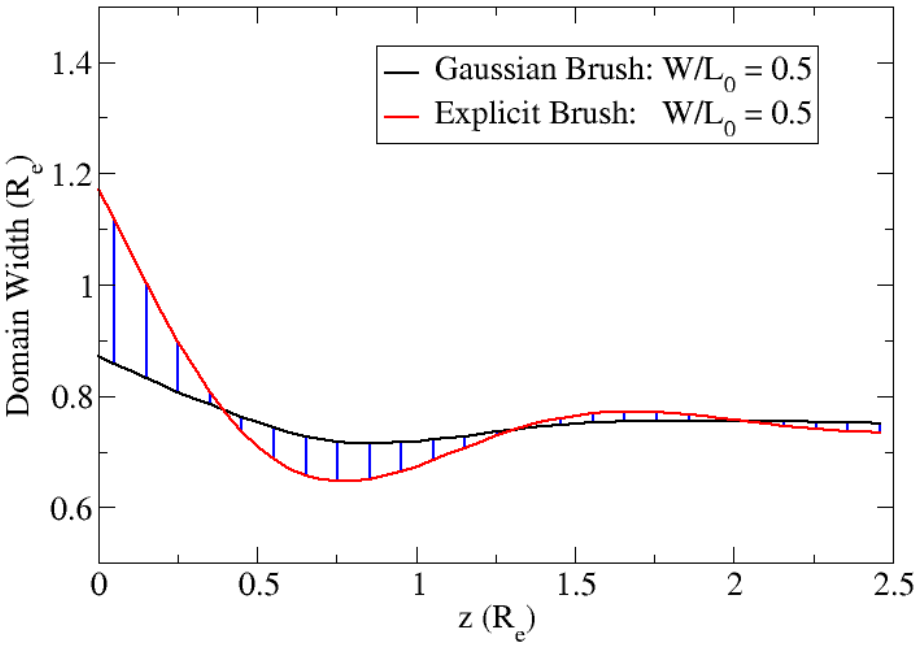

Figure 2.6: The average domain width of Domain 1 shown in Figure 2.4a for two different simulations. The blue lines connecting the two curves are a visual indicator of the integral of the difference that is used to calculate the fitness of a Gaussian Potential Model parameter set for modeling an explicit polymer brush.

calculated as the integral

$$\gamma = \sum_{j} \int_{0}^{L_z} (I_{j,EBM}(z) - I_{j,GPM}(z))^2 dz \tag{2.5}$$

where $I_{j,k}(z)$ is the iso-curve of domain $j \in \{1, 2, 3, 4\}$ for the model $k \in \{\text{EBM}, \text{GPM}\}$ over the dimension normal to the hard surfaces, z. A graphical interpretation of the integral γ can be seen in Figure 2.6. The set of GPM parameters $\{ds, W, \Lambda_S N, \Lambda_B N\}$ that minimizes the function γ provides the mapping of the chosen brush parameters.

First, we demonstrate this minimization by fixing $\Lambda_S N$, $\Lambda_B N$, and d_s, and minimizing γ through the width of the guiding stripe. The backfill strength is chosen to be $\Lambda_B N = 0.0$ as the backfill brush being investigated is non-preferential, while $\Lambda_S N = 0.75$ and $d_s = 0.15$

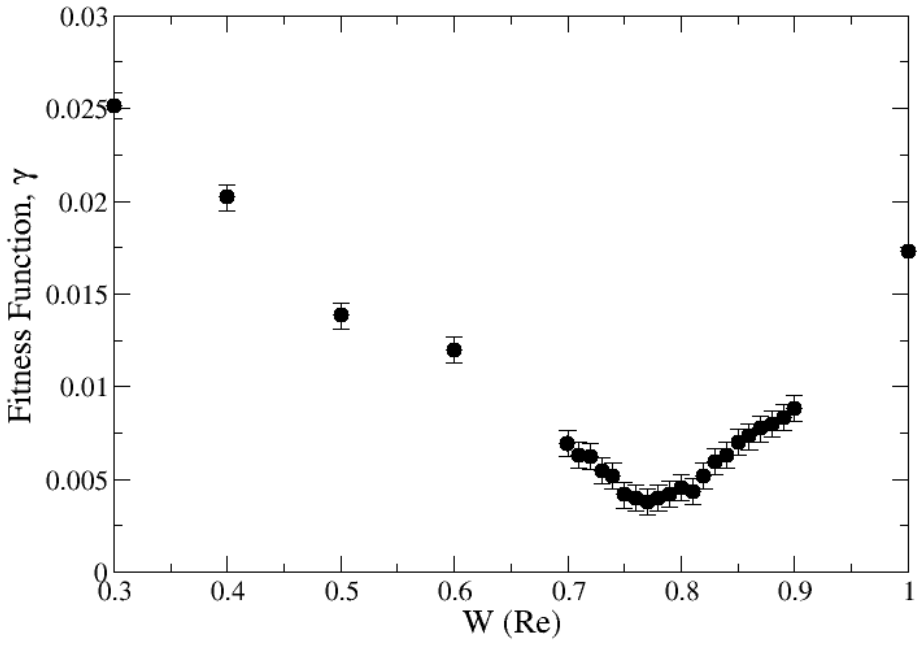

Figure 2.7: The value of the fitness function γ for different guiding striped widths, which is a metric for quantifying the efficacy of a given set of parameters for the Gaussian Potential Model for modeling a given explicit polymer brush. In these simulations, only the guiding stripe width is changed, the other relevant parameters are kept constant: $d_s = 0.15$, $\Lambda_S N = 0.75$, and $\Lambda_B N = 0.00$.

to be comparable to values used in previous works using the TICG model. Figure 2.7 shows the value of γ for a set simulations of the GPM with different guide stripe widths versus the same EBM, where $B_D = 125$ chains/R_e^2, $M_b = 0.2$, $W/L_0 = 0.5$, and $f_{A,BF} = 0.5$. It is clear that there is a width of the guiding feature for the GPM that best represents the more detailed model. However, there is still a difference between the interfacial profiles, as the minimization is only being done using one parameter. A brute force search over all four parameters would be ineffective, especially when considering that such a methodology would need to be repeated for new brush designs.

We therefore rely on an evolutionary optimization algorithm (the Covariance Matrix Adaptation−Evolutionary Strategy (CMAES)) to find an optimal set of parameters in this

large design space. This optimization technique seeks to maximize a chosen fitness function by exploring an arbitrary number of continuous variables, in this case four. The details of this strategy can be found in previous works. The fitness function used here is simply γ. Each optimization generation consists of 32 simulations; the single simulation with the lowest value of γ is used when launching the next generation of simulations.

Once again, the same simulation of the EBM is used to generate the target morphology. The CMAES minimizes the fitness function by varying all four parameters simultaneously. The evolution of all four parameters and the value of the fitness function can be seen in Figure 2.8. After approximately 50 generations the four parameters have converged to a set of values that remains essentially unchanged over the next 50 generations. Figure 2.9 shows iso-curves of each type of domain from the best simulation in Generation 1 in red, the best simulation in Generation 109 in green, the iso-curve from the brute force minimization in blue, and the target iso-curve from the EBM. The CMAES finds a set of parameters for the GPM to approximate the more detailed EBM faster and with less total simulations than trying to find the optimal combination of parameters through brute force parameter sweeps. The value of the γ found using the CMAES is also lower than that found through the "naïve" minimization above. The value found through CMAES is $\gamma = 0.001$ and through the naïve approach it is $\gamma = 0.005$.

The values of the converged parameter set found by the CMAES are shown in Figure 2.8. As expected, the strength of the backfill converges to $\Lambda_B N = 0.0$, which was the value used in the brute force minimization above. In addition, the width of the stripe is $W/L_0 = 0.75$, which is approximately the value found in the naïve minimization. However, the values of $\Lambda_S N$ and the range of interaction d_s are different. A stronger interaction strength and a shorter range of interaction provides a lower value of γ than the brute force simulation.

Looking back at Figure 2.4, there is a clear visual difference between the morphology equilibrated through a naïve implementation of the pattern parameters and the morphology predicted after the optimization. The ability of the brush chains to move laterally creates an

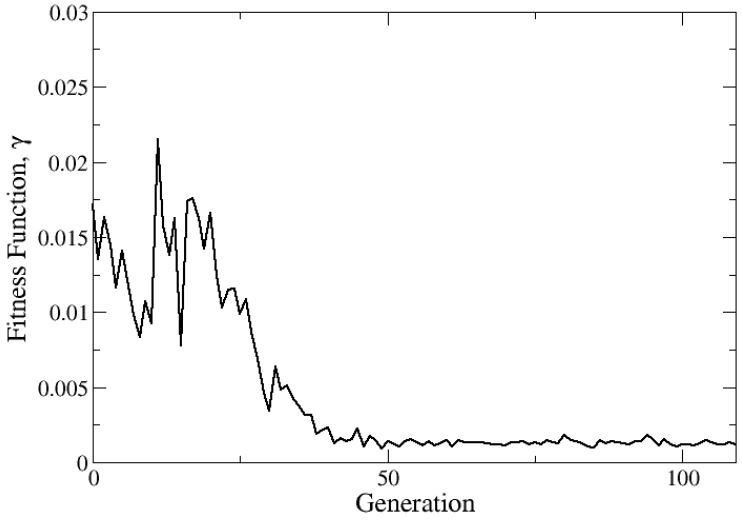

(a)

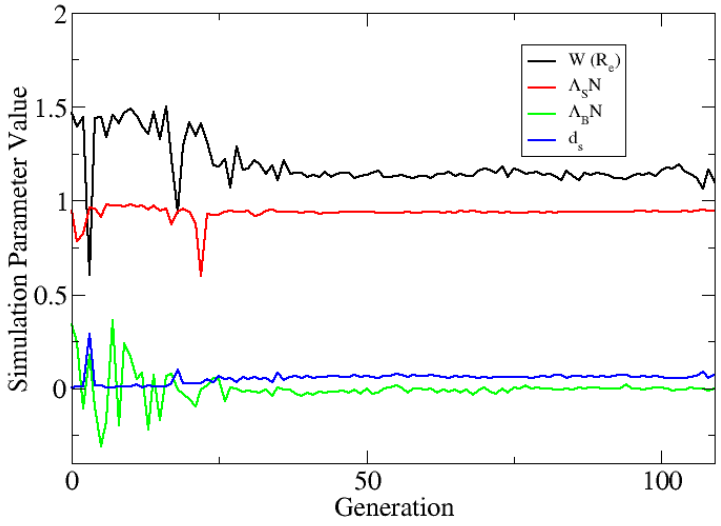

(b)

Figure 2.8: a) Value of the fitness function gamma at each generation of the CMA-ES, when calculating the optimum parameter set for the Gaussian Potential Model for modeling the Explicit Brush Model with $W/L_0 = 0.5$, $f_{V,A} = 0.5$, $B_T = 0.25$, $B_D = 125$ chains/R_e^2, and $M_b = 0.2$. (b) The evolution of the parameters used in the Gaussian Potential Model at each generation of the CMA-ES optimization procedure.

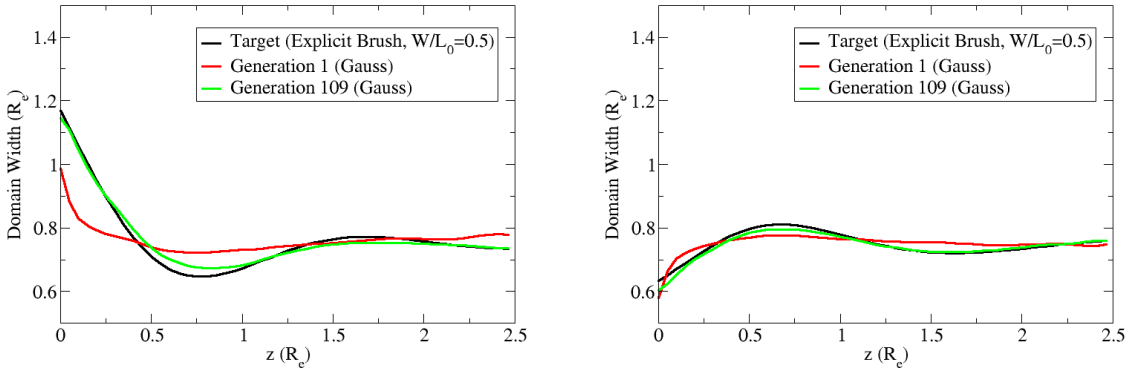

Figure 2.9: Curves of the average interfacial domain width as a function of distance from the substrate interface at $z = 0.0$. The unique domains highlighted in Figure 2.4a are shown in the different graphs. Unique domain 1, 2, 3, and 4 are shown in plots a, b, c, and d, respectively. The black curves rerpesent the domain width of the target morphology. The red curve represents the domain widths calculated in the first generation of the CMA-ES algorithm. Finally, the blue curve represents the domain widths calculated after convergence of the CMA-ES optimization procedure.

Table 2.1: Parameters and fitness of different optimization schemes for fitting an explicit brush simulation, where $B_D = 125$ chains/R_e^2 and $M_b = 0.2$

Optimization Strategy	**Guiding stripe width** $[W/L_0]$	**Range of interaction** $[d_s]$	**Guiding stripe strength** $[\Lambda_S N]$	**Backfill strength** $[\Lambda_B N]$	**Fitness function value**
Naïve	0.50	0.15	0.750	0.000	0.016
Single Parameter	0.78	0.15	0.750	0.000	0.005
CMA-ES	0.75	0.07	0.945	-0.004	0.001

artificially larger stripe area, that must be accounted for when modeling the same system, except where the brush surface is approximated as a hard wall. However, even though some physics is lost in the approximation, there exists a set of parameters that allows for one to capture the same end result, with the more simplified model.

Using the parameters identified with the CMA-ES algorithm, we attempt recover the morphologies stabilized in simulations of the same brush in the EBM with different guiding stripe widths. We show the comparison between a GPM with the CMA-ES parameters where the guiding stripe is $W/L_0 = 0.65$ and the EBM that has been used to parameterize the GPM in this work, except with a guiding stripe of $W/L_0 = 0.3$, is shown Figure 2.10 . The four unique domain types identified in Figure 2.4 are shown in insets a through d, where the interfacial width as a function distance from the substrate of the two simulations are compared. Qualitatively the GPM with the optimized parameter set reproduces the interfacial profile closely. The same qualitative comparison is provided in Figure 2.11 between a GPM with $W/L_0 = 0.95$ and an EBM with $W/L_0 = 0.7$. In both Figure 2.10 and Figure 2.11 it can be seen that the parameterization of the GPM does a good job recovering the morphologies predicted by the EBM for this range of guiding stripe widths, those that have widths of $W/L_0 < 0.8$.

However, by analyzing Figure 2.12 closely, it can bee seen through optical inspection that this parameterization of the GPM does not exactly recover the morphologies observed over wider guiding stripes, where $W/L_0 > 0.8$. Over these widths in the EBM, the assembled morphology has a unguided domain centered atop the guiding stripe, creating a U-shaped

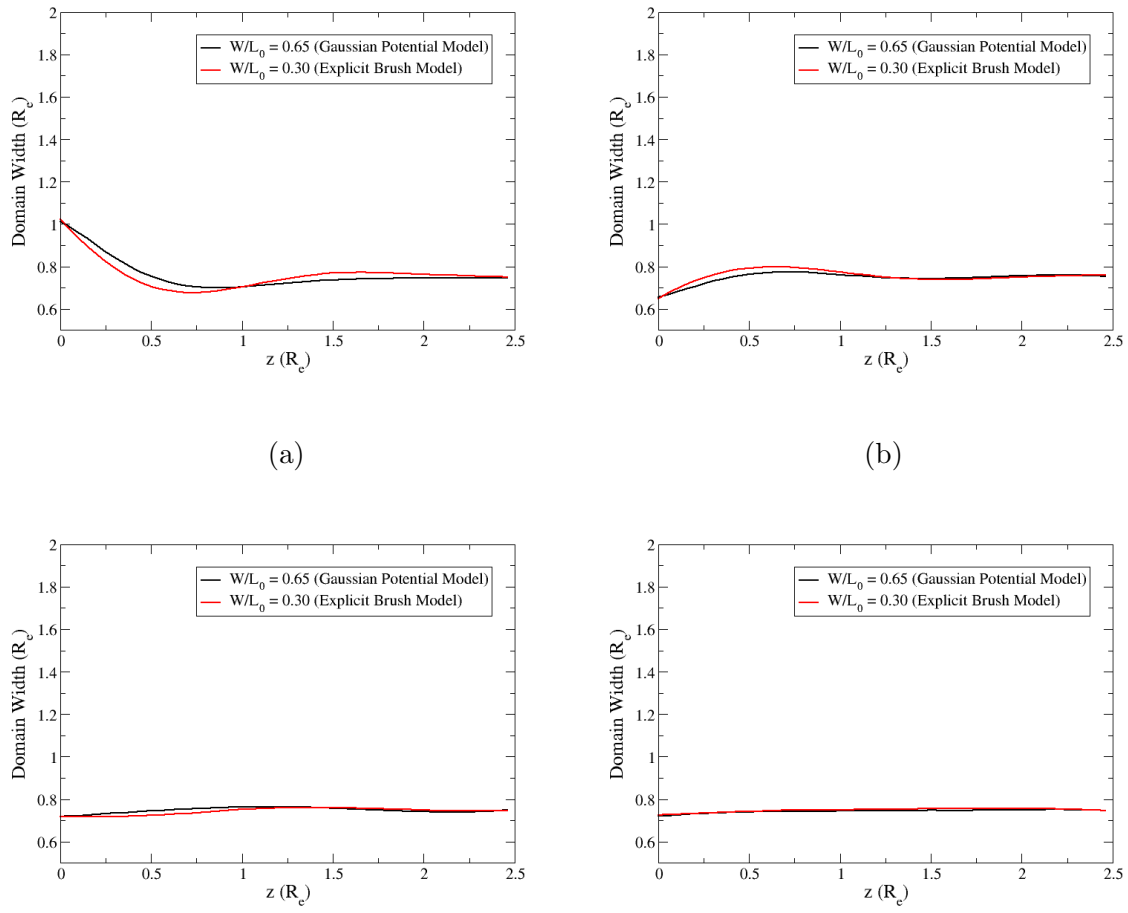

Figure 2.10: Curves of the average interfacial domain width as a function of distance from the substrate interface at $z = 0.0$. The unique domains highlighted in Figure 2.4a are shown in the different graphs. Unique domain 1, 2, 3, and 4 are shown in plots a, b, c, and d, respectively. This is a comparison of a morphology assembled in the EBM model where the guiding stripe width was $W/L_0 = 0.3$ with a morphology assembled in the GPM model where the guiding stripe width was $W/L_0 = 0.65$. The red curves rerpesent the domain widths of morphology assembled in the EBM model. The black curves represent the domain widths calculated using the optimized CMA-ES parameters detailed in Table 2.1.

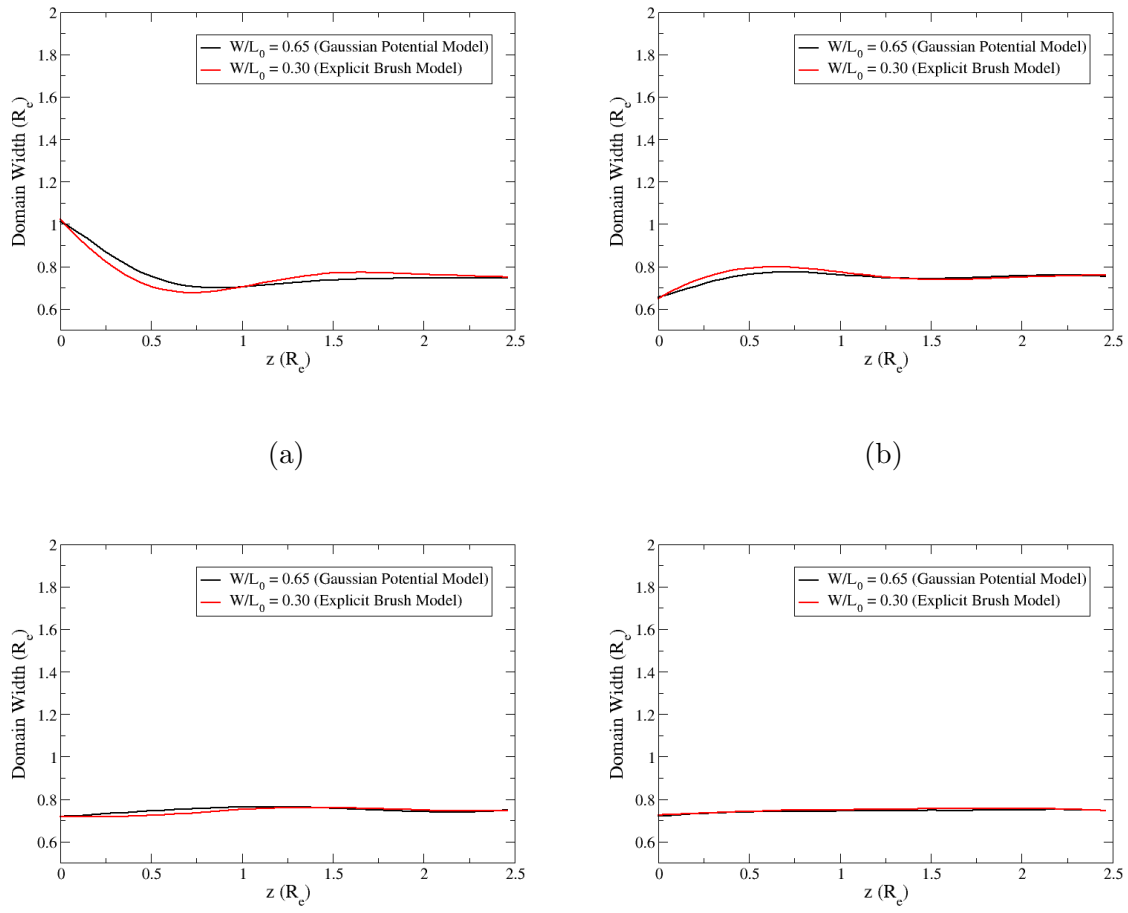

Figure 2.11: Curves of the average interfacial domain width as a function of distance from the substrate interface at $z = 0.0$. The unique domains highlighted in Figure 2.4a are shown in the different graphs. Unique domain 1, 2, 3, and 4 are shown in plots a, b, c, and d, respectively. This is a comparison of a morphology assembled in the EBM model where the guiding stripe width was $W/L_0 = 0.7$ with a morphology assembled in the GPM model where the guiding stripe width was $W/L_0 = 0.95$. The red curves rerpesent the domain widths of morphology assembled in the EBM model. The black curves represent the domain widths calculated using the optimized CMA-ES parameters detailed in Table 2.1.

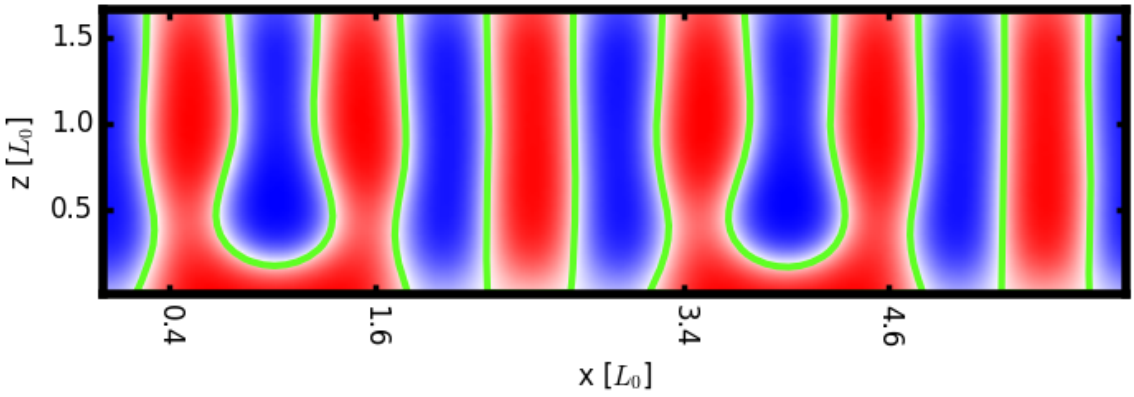

(a)

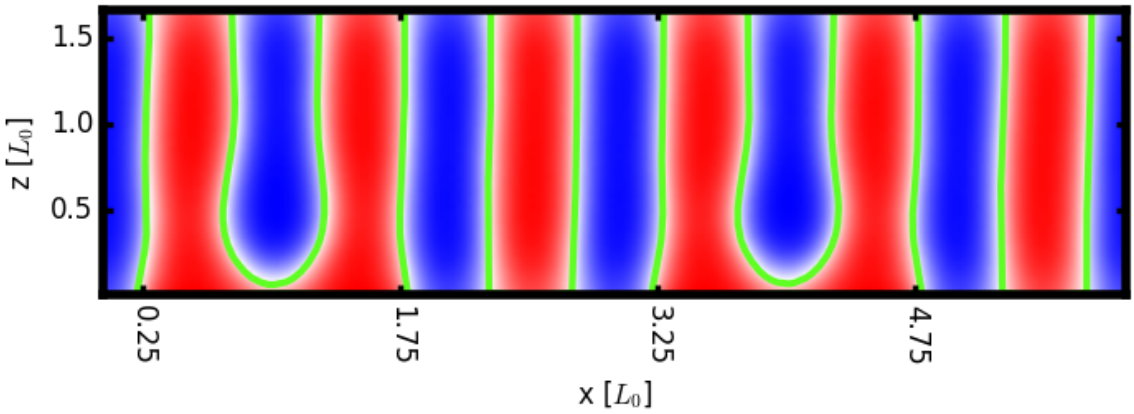

(b)

Figure 2.12: Average two-dimensional equilibrium morphologies. The red domains represent the block copolymer domain, which is guided by the guiding feature, and the blue domains are comprised of the unguided block. The domains are labeled between 1 and 4 to identify the number of unique domains which exist atop a 3X density multiplication pattern with a guiding feature with width $W/L_0 < 1.0$. The tick marks on the horizontal axis represent the bounds of the guiding features within the simulation box. a) The morphology captured from a simulation of the Explicit Brush Model, with $W/L_0 = 1.2$, $f_{V,A} = 0.5$, $B_T = 0.25$, $B_D = 125$ chains/R_e^2, and $M_b = 0.2$. b) The morphology captured from a simulation of the Gaussian Potential Model with $W/L_0 = 1.5$, $d_s = 0.07$, $\Lambda_S N = 0.945$, and $\Lambda_B N = -0.004$.

structure, where the guiding stripe is completely wet by the guided material. As seen in Figure 2.12, the thickness of this wetting layer is underestimated, however the basic shape of the structure is recovered. The difference in wetting layer thickness is unsurprising as the CMA-ES did not optimize based on this parameter. There is opportunity to develop a more comprehensive fitness function that may be able to identify a parameter set that more accurately recovers this feature while maintaining accuracy over the thinner stripes. The optimizatoin using the fitness function presented in this work, however, shows that a a hard surface model can adequately model the morphological behavior of these brush systems.

Table 2.1 shows the comparison between the techniques to choose a parameter set to describe the brush system. It is clear that optimization of all four parameters simultaneously via the genetic optimization algorithm produces a set of hard-surface parameters that provide the best approximation of the more real brush system. This strategy provides an efficient methodology to map an explicit brush design to an implicit surface potential. The key values of d_s, $\Lambda_S N$, and $\Lambda_B N$ can then be used to explore various other guide stripe widths, while the mapping procedure provides reference to the relative difference between the functional size of the guide stripe width versus its design size. While, this strategy does well for a range of guiding stripe widths, it is unable to capture exact morphological recovery over wider guiding stripes, where it underestimates the wetting layer formation. Through this methodology, the values of $\Lambda_S N$ and $\Lambda_B N$ gain a more quantitative meaning rather than the qualitative relationship to pattern design that existed when using this model in previous works.

2.4 Conclusions

The development of a framework for implementing an explicit polymer brush as a substrate pattern has been presented. The size and volume of the simulation must be scaled appropriately to maintain reasonable local densities within the simulation box. A film-thickness can be chosen for each combination of grafting density and brush molecular weight to re-

alize local densities that are similar with previous work and theory. With a commensurate thickness for the brush pattern, the brush can be separated into two different components, one being the guiding feature and the other is the backfill region.

With a model for the explicit brush created, we present a methodology for mapping this more detailed simulation back to the the simpler Gaussian Potential Model, which approximates the brush-melt interface as a hard, impenetrable surface. Through a fitness function which quantifies the difference in predicted equilibrium morphology, we used the Covariance Matrix Adaptation−Evolution Strategy to optimize the parameters of the hard-surface substrate to most closely mimic the results of the explicit brush. We show that a set of parameters can be chosen for the Gaussian Potential Model to suitably recreate the morphology predicted in the Explicit Brush Model. The optimization procedure revealed that the hard surface underestimates the perturbation caused by a guiding stripe, due to the ability of brush molecules to penetrate and reach further than their anchoring. This results in needing to use a wider stripe in the GPM to model the relevant brush pattern. The work demonstrates that, the GPM is an adequate tool for simulating the Directed Self-Assembly of block copolymers in thin films, as it can be tailored to produce results that are equivalent to more computationally expensive and realistic models; as long as a parameterization is done to identify the necessary mapping.

CHAPTER 3
DESIGN OF SURFACE PATTERNS WITH OPTIMIZED THERMODYNAMIC DRIVING FORCES FOR THE DIRECTED SELF-ASSEMBLY OF BLOCK COPOLYMERS IN LITHOGRAPHIC APPLICATIONS

3.1 Introduction

The directed self assembly (DSA) of block copolymers (BCP) in thin-films has garnered interest as a complimentary technique for nanolithographic patterning at ultra-small dimensions.[2, 5, 6] The DSA process offers a cost-effective solution to enhance the performance of current 193nm immersion lithography technology for obtaining dense arrays of features, [19, 26–28] and has recently undergone a transition from laboratory to industrial scale to assess for high volume manufacturing (HVM).[29, 30] Several bottom-up techniques, where the polymer melt is spin-coat onto a substrate that has chemical or topographic patterns, have been shown to achieve long-range order of the self-assembled microdomains.

Density multiplication is one of the techniques has emerged as one of the most promising techniques for producing arrays of lines-and-spaces with critical dimensions of less than 30 nm. A nanopatterned substrate used for density multiplication of diblock copolymers is comprised of a stripe, which is preferentially wet by one of the blocks, and a region referred to as the background, which exhibits little to no preference for either block. Typically, the backfill is functionalized using random copolymer brushes made of the same monomer units as the BCP being assembled, the industry standard being poly-styrene (PS) and poly-methyl methacrylate (PMMA). Mansky *et al.* demonstrated that the composition of random copolymer brushes can be varied to tune the surface energy in a precise manner.[31, 32] In the case of hydroxyl terminated poly(styrene-*random*-methyl methacrylate) copolymer (P(S-*r*-MMA-OH) brushes, a brush with approximately 58% PS was shown to have the same

interfacial energy with each block of a lamella forming PS-PMMA BCP. Using this type of nonpreferential material provides the boundary conditions that allow for the assembly of the lamella domains perpendicular to the substrate, which is the desired orientation for industrial application. Although there is a unique composition that is neutral to both blocks of the assembled polymer, there exists a range of brush compositions that allows for perpendicular orientation of the assembly. Liu *et al.* studied the effects of brushes in this composition range on DSA using density multiplication and discovered that the best patterns for assembling lines-and-spaces were composed of a backfill brush that had slight preference for the the block opposite of that which is preferred by the guiding stripe.[27]

Rincon Delgadillo *et al.* were able to achieve DSA with high degrees of perfection over large areas in the final assembly of the BCP over 3X density multiplication patterns with multiple guide stripes that were approximately half and three-halves of the natural domain spacing of the assembled polymer using a non-preferential backfill brush.[33] In that study, the final assemblies were analyzed using top-down scanning-electron microscopy (SEM) images. The two process windows in substrate design space identified by Rincon Delgadillo *et al.* were separated by a range of guiding stripe widths that resulted in fingerprint assembly over the guiding pattern.[34] The transitions in design space from a pattern that produces a single grain of lines-and-spaces to a pattern that results in a random assortment of grains are abrupt. Within these process windows of successful DSA, there is little that can be gleaned about the capabilities of one set of pattern parameters to drive the assembly of lines-and-spaces relative to another set through top down image inspection. In past works, molecular simulations have provided insight into the three-dimensional morphology of assembled films and corroborated the existence of large windows in process space where one can assemble lines-and-spaces over nanopatterned substrates.[35, 36] However, little has been done to quantify how pattern design at macromolecular length scales affects the thermodynamic driving force for assembly of a single grain.

Here, we use the Theoretically Informed Coarse-Grained (TICG) model, which has been

shown to be in qualitative and quantitative agreement with experiment in prior works, as the machinery in which we implement a strategy for evaluating a substrate's efficacy at driving self-assembly. We build on previous work, in particular, the comparison of dislocation defects to perfect assembly free-energies performed by Nagpal *et al.* through thermodynamic integration provides a methodology by which to calculate the relative free-energies of metastable state. In the case of Rincon Delgadillo *et al.*, the meta-stable state most commonly seen outside the observed process windows is fingerprint assembly. Therefore, we attempt to make a first approximation about the relative efficacy of a substrate pattern by comparing the free-energy of lamella perfectly aligned to the underlying pattern to that of fingerprint assembly over the same pattern. We calculate this metric by using multiple simulations of single grains misaligned at unique angles to the underlying pattern and compare the lowest in free-energy, the most competitive, with the free-energy of the aligned assembly. As we use only a single grain, we are afforded the opportunity to use smaller simulation boxes, which makes the presented methodology tractable for a wide range of combinations of design parameters.

While previous work focused on finding ranges of patterning conditions that were effective at stabilizing well-aligned lamellae over the patterns, here we calculate the relative energies of the driving forces of patterns within these windows to elucidate design strategies that will be useful in achieving a single grain of lines-and-spaces. By combining experimental data and molecular simulations, we study the impact of the interfacial energy between BCP and a nanopatterned substrate on the thermodynamics of the assembled film. The implementation of process flows on 300mm wafers using an X-PS guiding stripe and random copolymer backfill brush allowed for the evaluation of the impact of materials and processing conditions on the DSA over large areas, while the fabrication and inspection of patterned samples using automated tools at imec enabled investigation of DSA on chemical patterns of various dimensions and chemistries. We used this industrial scale fabrication facility to systematically explore the effects that these tunable parameters have on the assembly of a

Table 3.1: Labels for polymer brushes with different poly(styrene) compositions

Brush	PS fraction, f_S
Brush-44	0.44
Brush-46	0.46
Brush-51	0.51
Brush-56	0.56
Brush-60	0.60
Brush-63	0.63
Brush-69	0.69

single grain aligned with underlying pattern. A collection of patterns was prepared with many combinations of backfill brush composition and guiding stripe width, W. We compare this data with free-energy calculations of coarse-grained Monte Carlo simulations of different grain orientations in these two process windows to gain insight into how different design parameters affect the relative free energies of competitive grains. This strategy is used to understand the effect that interfacial energy of the substrate and guide stripe width have on the effectiveness of a chemical pattern to drive the DSA process for HVM.

3.2 Experiments

3.2.1 Materials

Cross-linkable poly(styrene) (X-PS) (AZEMBLY™ NLD128), hydroxyl-terminated poly(styrene-*random*-methyl methacrylate) brushes with various monomer fractions, referred to as f_S and f_{MMA}, (AZEMBLY® series, shown on Table 3.1), and poly(styrene-*block*-methyl methacrylate) (PS-*b*-PMMA) (AZEMBLY™ PME312) lamellae forming BCP with a domain-spacing of $L_0 = 28$ nm, were synthesized and dissolved in organic solvent by EMD Performance Materials and used as received. Photoresist AIM5484 was purchased from JSR Micro and developer OPD262 from Fujifilm. Organic solvents RER600 and Orgasolv STR 301 were purchased from Fujifilm and BASF, respectively, and used as received.

3.2.2 Sample Preparation

All samples consisted of 300 mm Si wafers and were processed and inspected using all-track processing at imec (Leuven, Belgium).

Chemically nano-patterned substrates

For the fabrication of the patterned substrates, a 14 nm inorganic antireflective coating (ARC) film of SiN was deposited on the 300 mm Si wafers via chemical vapor deposition. Next, an 8 nm thick film of X-PS was spin-coated on the SiN layer and annealed for 5 min at 315°C under a nitrogen atmosphere in a TEL CLEAN TRACK ACT™ 12. The thickness of the SiN and X-PS films was selected to minimize surface reflections during photoresist exposure with 193 nm immersion lithography. Subsequently, a 95 nm thick layer of photoresist was coated and baked at 120°C for 1min. The samples were exposed on an ASML NXT:1950i scanner using the "Vinaigrette" mask, which contains gratings of multiple pitches (L_S) and widths, as well as a large area (7.5 mm x 5 mm) with pitch $L_S = 84$ nm. A 1.35 numerical aperture (NA) and quadrupole illumination (XY polarized, $\sigma_o = 0.87$, $\sigma_i = 0.72$) yielded well-defined line/space patterns with pitches in the range of 80-89 nm. Different widths of the photoresist lines, or critical dimension (CD), were obtained by using a focus-exposure matrix (FEM), in which the exposure energy and the focus were systematically varied on each field. The exposure dose was varied from 13-23 mJ/cm^2 in 1 mJ/cm^2 increments, and the focus was chosen in a range of 360 nm at 20 nm increments. Combinations of dose and focus were used to produce approximately 160 different exposure conditions on a single sample. After exposure, the samples were baked at 120°C for 20 sec and developed using OPD262. The samples were submitted to an O_2 and Cl_2 plasma etch step in a V3A Lam Research tool, to trim the resist lines and, simultaneously, remove the X-PS exposed to the plasma. The remaining photoresist was selectively removed from the X-PS using a wet strip with Orgasolv® STR 301 yielding periodic X-PS guiding stripes. The series of OH-terminated brushes of specific composition presented in Table 3.1 were

spin-coated at 1500 rpm yielding 50 nm thick films and annealed for 5 minutes at 250°C in a nitrogen environment. During the annealing step, a monolayer of the brush material was grafted to the regions between the X-PS lines via a condensation reaction. The material that did not react with the surface was rinsed with RER600. On the resulting periodic chemical patterns of defined chemistry and geometry, a 32 nm thick film of BCP, PME312™, was coated and annealed for 5 minutes at 250°C. To improve the contrast on the SEM images, the PMMA block was removed using a dry etch process in a TEL Tactras™ system. A Hitachi CG4000 scanning electron microscope (SEM) was used to image and measure the CD of the photoresist after trim etch, as well as the BCP assembled structures after PMMA removal. Representative images from eight CD per pitch (80-89 nm in 1 nm increments) were taken at five dose steps exposed at best focus. Each SEM image obtained was matched with its corresponding boundary condition. In addition, ten random locations on the 84 nm pitch large patterned areas, exposed at different doses and best focus, were imaged using relatively low magnification (2.5 mm x 2.5 mm).

Homogenous substrates

Non-patterned substrates were used for the characterization of the X-PS and the brush materials at different steps of the process. For this purpose, the polymer solutions were applied on bare Si wafers and processed with the same conditions as the step of interest, described in the fabrication of chemical patterns. The wetting properties of the materials comprising the chemical nano-patterns were characterized using static water contact angle. A Dataphysics OCAH230L contact angle measurement system was used for this purpose. In addition, ellipsometry measurements of homogeneous films deposited on (or grafted to) bare silicon wafers were performed using a KLA Tencor SCD100 over 49 points across the diameter to determine their thickness and uniformity.

3.2.3 Simulation Model

The simulation results presented are based on the standard coarse-grained model for block copolymers.[17] Previous work has relied on this model to elucidate morphological behavior of block copolymer films on chemically and topologically patterned substrates and results have been quantitatively consistent with experimental observation.[21, 37–39] Polymers in the model are represented by flexible, linear Gaussian chains discretized into N beads, where the position of the s^{th} bead in the i^{th} chain is given by the vector $r_i(s)$. A system is comprised of n AB copolymer molecules in a fixed volume V at a fixed temperature T. The Hamiltonian $H = H_b + H_{nb} + H_s$ of the system includes the interactions between bonded beads (b), the non-bonded interactions(nb), and the interaction of beads with the substrate (s). The connectivity of neighboring beads in a polymer chain is modeled by describing the bonded interactions acting along the chain by

$$\frac{H_b[\{\mathbf{r}_i(s)\}]}{k_B T} = \frac{3}{2b^2} \sum_{i=1}^{n} \sum_{s=1}^{N-1} [\mathbf{r}_i(s+1) - \mathbf{r}_i(s)]^2 \tag{3.1}$$

where k_b is the Boltzmann constant, $b^2 = R_e^2/(N-1)$ is the mean-squared bond length, and R_e^2 is the mean-squared end-to-end distance of an ideal chain. The non-bonded interactions are described by

$$\frac{H_{nb}[\phi_A, \phi_B]}{k_B T} = \frac{\sqrt{\overline{N}}}{R_e^3} \int_V d\mathbf{r} [\chi_{AB} N \phi_A \phi_B + \frac{\kappa N}{2} (1 - \phi_A - \phi_B)^2] \tag{3.2}$$

where $\sqrt{\overline{N}} = \frac{\rho_0 R_e^3}{N}$ represents the invariant degree of polymerization, which is proportional to the polymer's molecular weight in a dense melt, and ρ_0 is the bead number density. The local dimensionless density ϕ_K of species $K = A, B$ is computed using the configuration of the polymer beads relative to a lattice with spacing ΔL using a zeroth order particle-to-mesh interpolation. The incompatibility between unlike species is measured by the Flory-Huggins parameter, $\chi_{AB}N$, and the inverse isothermal compressibility, κN, gives the polymer melt

a finite compressibility.

To model the experimental systems used for DSA of block copolymers, the polymer is confined between two impenetrable walls normal to the z-axis of the simulation box. The top wall at $z = L_z$ is considered neutral, whereas the bottom wall at $z = 0$ mimics the chemically patterned substrate on which the block copolymer assembles. The interaction between the substrate and polymer is modeled by a one-body potential acting on each bead of the form

$$\frac{U_S(\mathbf{r}_i, K_i)}{k_B T} = \frac{\Lambda_{K_i}(x, y)}{d_s} \exp(\frac{-z^2}{2d_s^2}) \tag{3.3}$$

where d_s governs the range of the interaction and z is the distance between the polymer bead and the substrate along the axis normal to the substrate. The total contribution of the substrate-polymer interaction to the Hamiltonian is

$$\frac{H_s}{k_B T} = \sum_{i=1}^{nN} U_S(\mathbf{r}_i, K_i). \tag{3.4}$$

Λ_K represents the strength of the interaction between polymer beads of type $K = A, B$ located at (x, y) and the substrate. The functional form of Λ_K is dependent on the geometry of the chemical pattern.

Monte Carlo (MC) simulations are used to identify possible self-assembled morphologies over certain chemical patterns. Configurations are sampled according to Metropolis criteria, where the probability of accepting a trial configuration is given by $P_{acc} = \exp(-\Delta H/(k_B T))$, and where ΔH represents the energy difference between the original and proposed configuration. Trial configurations are produced using four different Monte Carlo moves: single bead displacement, translation of a chain, chain reptation, and chain inversion.

The polymer melt considered here is characterized by the parameters $\sqrt{\overline{N}} = 83$, $\kappa N = 22$, $\chi_{AB} N = 17$ which correspond qualitatively with AZEMBLY™ PME312 used in the experiments at imec. The lattice for computing local densities is defined such that the average number density of beads in any cell is $n_{int} = 14$. The computed bulk domain spacing

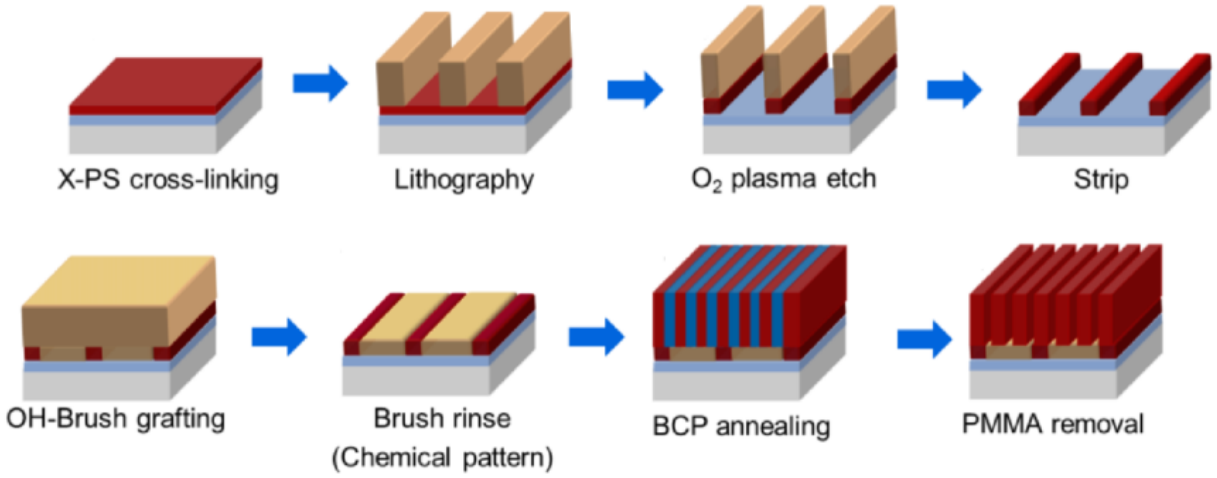

Figure 3.1: Liu-Nealey (LiNe) flow for the fabrication of chemically nanopatterned substrates with well-defined geometry and chemistry, and subsequent DSA of a symmetric BCP.

of the melt using these simulation parameters is $L_0 = 1.5R_e$. We choose $d_s = 0.05R_e$ to ensure that the interaction between the patterned substrate and the polymer operates on a range similar to that of the incompatibility between blocks. The underlying chemical pattern is composed of repeated stripes of width W that have a period L_S. The area between stripes is referred to as the backfill region. The guiding stripes' strength of interaction with the polymer is denoted by Λ_S and the backfill interaction by Λ_B. A larger value of Λ_S indicates a greater affinity of the stripes for the A-type polymer (PS), where a larger value of Λ_B indicates a greater affinity of the backfill for B-type polymer (PMMA).

3.3 Results

The chemo-epitaxy flow for directed self-assembly (DSA) of block copolymers (BCP) designed by Liu and Nealey (LiNe flow), shown in Figure 3.1, was used to assess the combinatorial effect of the composition and the dimensions of the chemically nano-patterned substrate on the assembly process. We used the fully-automated process implemented on industrial equipment available at imec. First, a thin film of X-PS was coated on a SiN layer deposited on 300mm silicon wafers. Next, a photoresist layer was coated and exposed using

193nm immersion lithography. The mask used for this work includes gratings of various pitches and a large patterned area of $L_S = 84$ nm. A matrix of focus and exposure doses (FEM) was used to print line/space patterns with varying critical dimension (CD). After exposure and development, a dry etch process was used to simultaneously tune the width of the photoresist lines and remove the X-PS exposed to the plasma. In the next step, the remaining photoresist was rinsed with organic solvent, yielding X-PS guiding-stripes. A series of OH-terminated brushes of specific composition was used to functionalize the area between the X-PS lines, often referred to as the backfill region, via condensation reaction of the hydroxyl-end groups and the oxygen moieties incorporated in the surface during the etch step. On these chemical patterns of defined geometry and chemistry, a BCP film was coated and annealed. After the removal of the PMMA block, the resulting structures were imaged and related to the boundary conditions used in each case.

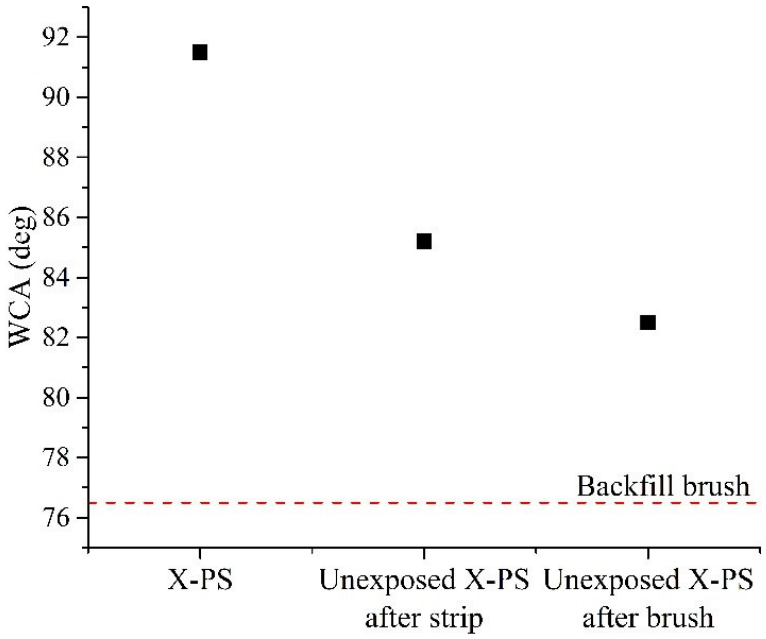

Figure 3.2: Water contact angle measurements of an X-PS film as coated and annealed, after resist strip, and after brush grafting, show the change in the wetting properties of the X-PS at each processing step in the creation of the chemically nanopatterned substrate.

In the fabrication of the chemical patterns, the X-PS is the first polymer applied on the SiN layer, which further underwent photoresist exposure, a trim-etch procedure, stripping of the photoresist, and brush deposition before coming into contact with the BCP material. In order to gain insight into the wetting properties of the guiding stripe relative to the unmodified X-PS, we assessed the impact of each of these steps on the chemical character of the X-PS prior to the construction of the final guiding feature. Due to the dimensions of the guiding stripe, direct evaluation of the wetting properties of the process-modified X-PS was difficult. Therefore, we created surfaces that were representative of the X-PS at each processing step. To achieve these model surfaces, we coated and annealed an X-PS and a photoresist layer onto an Si wafer with the same conditions described for the fabrication of the chemical patterns. On these substrates, checkerboard patterns, which consist of exposed and unexposed regions that are approximately 3cm x 3cm, were exposed using conventional illumination and energy of 18 mJ/cm^2. The printed areas are sufficiently large to allow for the measurement of the water contact angle (WCA) of each surface. The wafers were subsequently trim-etched, stripped, and coated with the different brushes to reproduce surfaces consistent with the X-PS at each step in the process of producing the chemically nanopatterned substrates. Water contact angle results for a blanket X-PS film and the unexposed and exposed areas on the checkerboard patterns that were processed prior to brush grafting are shown in Figure 3.2.

Each processing step made the X-PS film more hydrophilic. The first decrease in the WCA can be attributed to the degradation of the X-PS by the ultraviolet light generated during the exposure and the Cl_2 plasma during the trim-etch step.[40–42] Further optimization of the trim-etch may provide an alternative route to retain the hydrophobic character of the X-PS and increase the strength of the interaction between the guiding stripe and the BCP domains.

The second decrease in the WCA after the P(S-r-MMA)-OH coat and anneal suggests that the brush molecules can partially graft to the guiding stripes. This may be an additional

consequence of the modification of the X-PS, by UV irradiation, with oxygen-containing functionalities, which can further react with the hydroxyl end group of the random copolymer. At the end of the process, the unexposed X-PS presented a WCA of 82.5°, as shown in Figure 3.2. The total drop of nine degrees of the WCA indicated that the X-PS guiding stripe lost some of its non-polar character, resulting in a weaker expected interaction with the BCP. For the present analysis this is advantageous, as previous reports using the LiNe flow, as described in this study, show assembly of the BCP with a high degree of perfection, suggesting that the difference in interfacial energy between the X-PS and the backfill region with PS and PMMA is large enough to guide the BCP structures over thin ($W/L_0 \approx 0.5$) and wide guiding stripes ($W/L_0 \approx 1.5$). In contrast, a strong interaction with the guiding region may yield non-bulk morphologies during BCP assembly, especially for wide guiding stripes ($W/L_0 > 0$), which may limit the range of dimensions of the chemical patterns available for our investigation.[43, 44]

One important aspect of the LiNe flow is its brush-last approach, which ensures that the surface properties of the backfill area are exclusively controlled by the material design of the random copolymers grafted to this region. Therefore, before incorporating the P(s-r-MMA)-OH random brushes into the chemical nano-pattern, we measured the film thickness and WCA of each brush material, thereby gaining insight into the topographical and chemical nature of the patterned substrates. First, we coated blanket wafers with each unique brush and annealed to tether the molecules to the substrate through the hydroxyl end-group via the condensation reaction mentioned previously. Excess material was rinsed, yielding a monolayer that was chemically grafted to the surface. Film thickness and uniformity across wafer were characterized using ellipsometry. Independent experiments by varying anneal time and temperature have demonstrated that a saturated monolayer of a random copolymer brush with $f_{PS} = 0.51$, which is similar to the standard Brush-51 used in the experiments presented in this work, is about 7 nm.[45] We performed ellipsometry measurements on the AZEMBLY® series used in this work to provide accurate film thicknesses for the particular

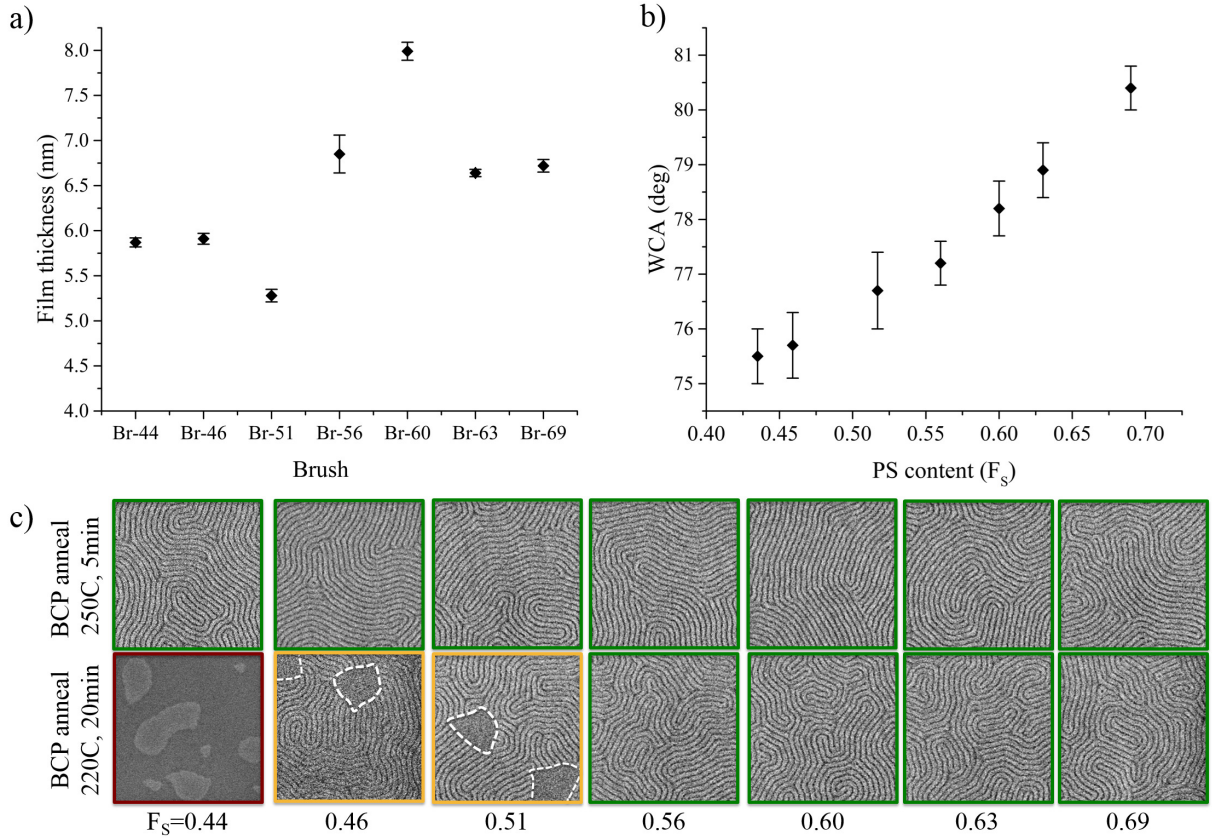

Figure 3.3: Characterization of a series of brushes with differrent compositions: a) monolayer film thickness after rinse as determined by ellipsometry measurements, b) water contact angle measurements, c) top-down SEM images of (P(S-*b*-MMA) films annealed at $220°C$ and $250°C$ on top of the different random brushes grafted onto silcon wafers. The green squares indicate the brushes that result in perpendicular BCP assembly, while yellow and red frames indicated mixed orientation and hole-island assemblies, respectively.

batch of materials used in the experiments shown. Figure 3.3a shows the film thickness results obtained for the investigated AZEMBLY® brushes; each measurement was performed on brushes that had the same initial film thickness and annealing conditions. The thinnest film was observed with Brush-51 where the thickness was measured to be 5.2 nm, while Brush-60 produced the thickest film of 8.0 nm. The difference of the brush thickness used in this work and the values obtained previously can be attributed to the different batches of materials used. In addition, we measured the thickness of a blanket X-PS film to be 7.2 nm. The difference between thicknesses of the blanket X-PS and each unique brush film suggests that there were minimal topographical features on the final patterned substrates.

The chemically modified surfaces were subsequently used to perform static WCA measurements. Figure 3.3b shows that the series of brushes exhibit a monotonic increase in WCA as f_S increases, with values that are in agreement with previous reports.[32] For the current study, in which the chemical patterns were comprised of an X-PS guiding stripe, Liu *et al.*[27] demonstrated that the optimal brush in the backfill region must be slightly PMMA preferential. Therefore, in order to test the wetting properties of the substrates treated with each brush material, a 32 nm film of BCP was coated on the samples and annealed at 250°C for 5 min or at 220°C for 20 minutes. As shown on Figure 3.3c, when the BCP was annealed using standard conditions (250°C, 5 min) all the samples showed perpendicular assembly of randomly oriented structures. However, at the lower temperature, mixed orientation was observed as the PS content in the brush decreases. At the lowest end, Brush-44 showed hole-and-island structures characteristic of preferential wetting of one of the blocks to the substrate. In contrast, the higher PS content in the brush materials ($\geq$ 56%PS) did not induce mixed or parallel orientation of the polymer domains. These results suggest that the composition of the brush series available in this study provides the wetting properties of interest, ranging from slightly preferential to the PMMA block to non-preferential.

The response of the BCP assembled on chemically nanopatterned substrates of different compositions and dimensions was also investigated. The impact of the commensurability of

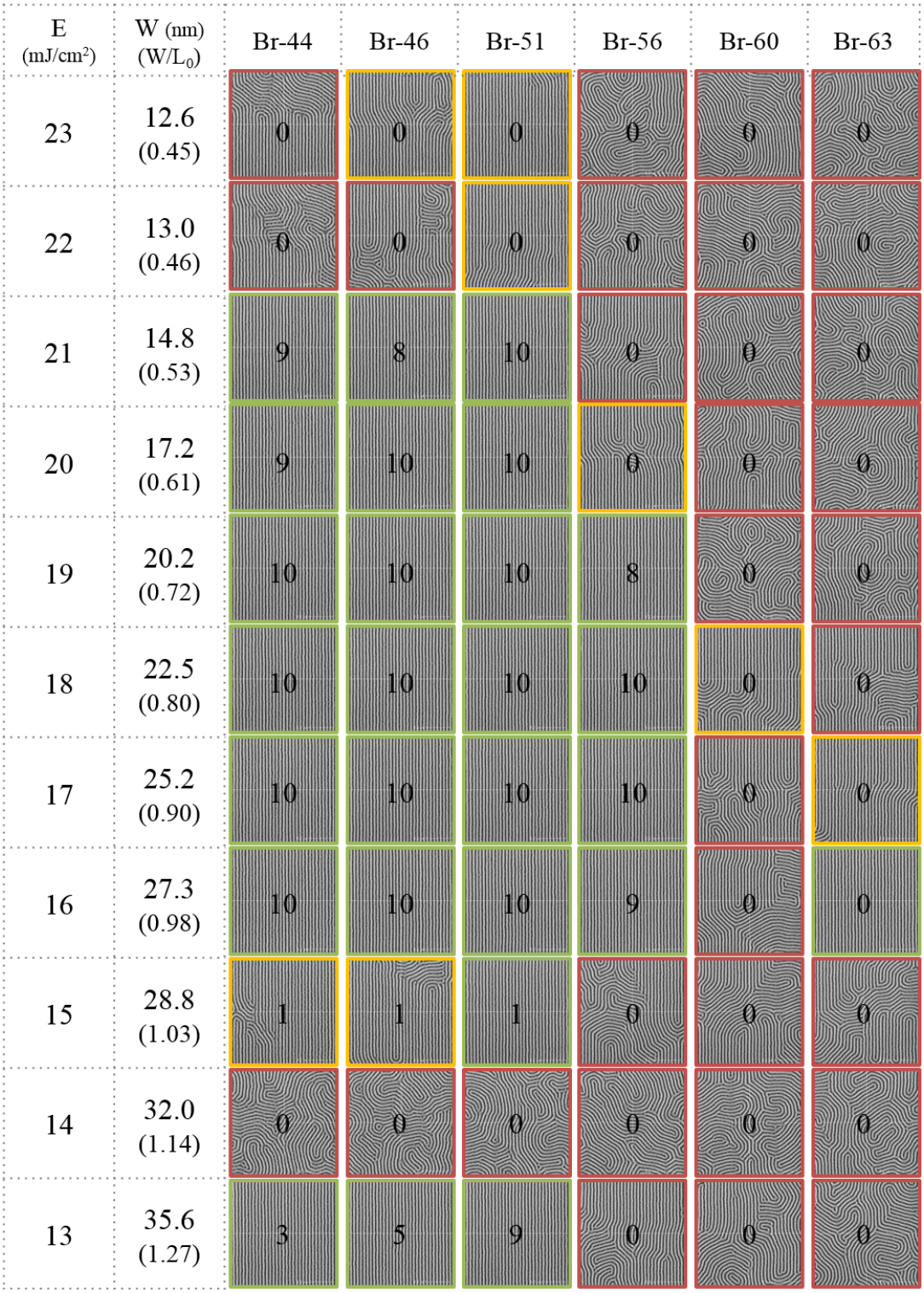

Figure 3.4: Top-down SEM images of a BCP assembled on chemical patterns with different W and backfill brush compositions over a pattern with an 84 nm pitch. The number on each die represents the number of defect-free images out of ten images analyzed.

the pattern period with the natural domain spacing of the BCP (L_S/L_0) and the width of the guide stripe (W/L_0) was studied by varying these parameters through the exposure and etching conditions, as described previously.[45] In addition, the interfacial energy between the PS and PMMA blocks with the backfill region was included in this analysis by using brushes of different compositions. In order to investigate the BCP behavior over large areas, the 84nm inspection blocks included from the reticle design were imaged using top-down SEM at ten different locations on each exposure condition. A total area of 62.5 μm^2 per die was imaged and used to evaluate the defect level through the patterned region. The number of defect-free images is reported as a measure of the degree of order, where a value of 10 indicates that all ten images taken had zero visible defects. This method does not differentiate between random orientation and a single dislocation; however, we can identify the pattern conditions that thermodynamically favor well-registered assembly (WRA) such that no misaligned sturctures exist after DSA. The results collected from ten dose steps at nominal focus with $12.6 < W < 35.6$ nm for the available brushes are shown in Figure 3.4. Random orientation or partial alignment, indicated by the red and yellow squares, respectively, was observed for all brush compositions when $W \leq 13.0$ nm, indicating that the guiding stripe is not wide enough to direct the BCP assembly. As W increases, good registration of the BCP with the underlying chemical pattern, represented by the green squares, was observed when $14.8 \leq W \leq 27.3$ nm on the samples treated with brushes of low f_S (0.44-0.51). In contrast, the images collected for large PS content random copolymers ($> 56\%$ PS) showed a drastic reduction of the process windows for the same guiding stripe width range. When W = 32 nm random orientation is observed for all brush compositions. This result is in good agreement with previous reports, where the lack of registration with the guiding material when $W/L_0 = 1.0$ was related to the largest total free energy of the system calculated at this condition. Finally, as W/L_0 approaches 1.5 , the material that resulted in the largest number of defect free images was Brush-51, although, in all cases, the process window was significantly smaller than the window for thinner stripes.

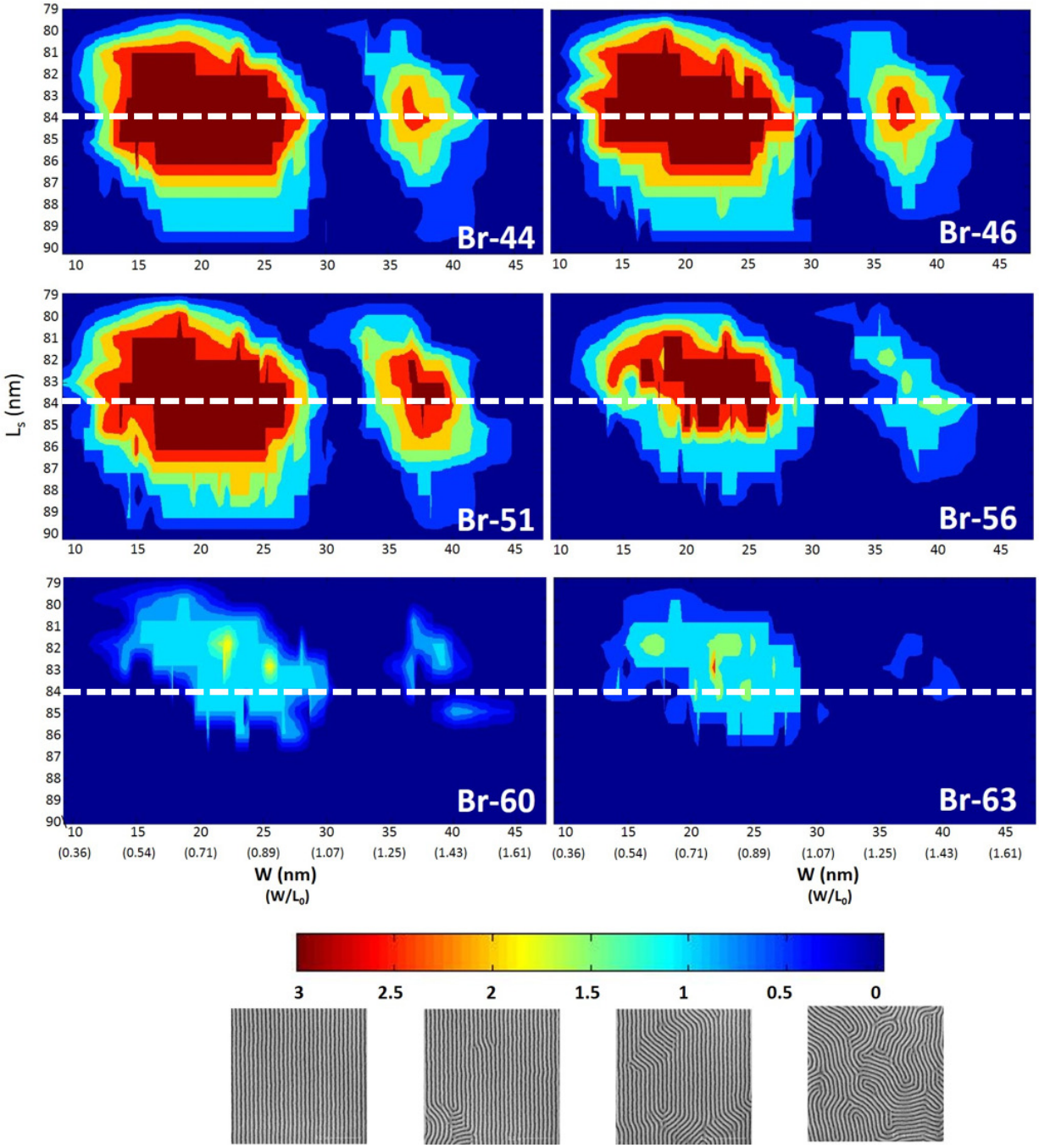

Figure 3.5: BCP assembly as a function of pitch (L_S) and width of the guiding stripe (W) for various compositions of the backfill brush. The color code used to evaluate the degree of perfection of the assembled structures is based on a $0-3$ score system corresponding to random orientation to good alignment, respectively, as shown by top-down SEM images. The dashed, white lines indicate the pitch that is commensurate with 3X density multiplication.

In order to include the impact of the commensurability of the pattern period with the natural domain spacing of the BCP (L_S/L_0) in our parameter space, we evaluated the degree of order of the BCP structures assembled on chemical patterns of different L_S, W, and backfill brush composition. For this end, top-down SEM-images of 2.5 μm x 2.5 μm area (1 μm x 1 μm are shown on Figure 3.5 to exemplify the scoring system) were assigned a score according to the degree of order observed at each condition. Ten random images, each of a 2.5 μm x 2.5 μm area, from each pattern design were investigated manually by eye to score the pattern. A range from 0 to 3 was used, corresponding to random orientation to a high degree of order, respectively. If at least nine of the ten images at the condition were absent of defects, then the pattern design was scored a 3. If fingerprint assembly was observed in all ten images, then the pattern was scored a 0. A score of 2 indicates that only isolated defects were observed, while a score of 1 indicates that among the ten images analyzed, a combination of images of fingerprint assembly and images of assemblies containing isolated defects were observed. This scoring system provides a qualitative experimental metric for the thermodynamic stability of a WRA compared to a misaligned structure. A score of 3 indicates that there is a large enough difference in the free-energy of the WRA and a misaligned domain that no other grains can be found in any field of view. In contrast, a score of 0 indicates that the the free-energy difference between all possible states is small, such that the field of view will consist of multiple grains. We identify a thermodynamic process window using this metric, by finding the conditions that produce SEM images with a score of 3.

Figure 3.5 shows these experimentally determined thermodynamic process windows in W/L_0 and L_S for patterns with different brushes. For the standard backfill material, Brush-51, the largest thermodynamic process windows in W occurred using a pattern with a commensurate pitch of 84 nm, where $L_S/L_0 = 3.0$. In addition, it can be observed that the BCP can accommodate to different pitches in the range of 81 nm$\leq L_S \leq$ 86 nm, with slightly higher tolerance for compression compared to stretching.

In terms of W, two process windows were obtained, in agreement with the observations over large patterned areas and with previous results. The largest window is observed when $W/L_0 < 1.0$ (12.4-27.0 nm). Process windows of similar size were observed at small values of W/L_0 for the chemical patterns with low f_S (0.44-0.46) grafted to the background. Still, Brush-51 showed more tolerance towards incommensurate chemical patterns, both at small and large pitches. Increasing the PS-content of the brush to $f_S = 0.56$ caused a shrink in these process windows. The brushes with the higher PS-content (Brush-60 and Brush-63) showed an even greater reduction in the process window size, such that only partial alignment was captured from top-down SEM images. As W/L_0 approaches 1.0, top-down SEM images show fingerprint patterns on all chemical patterns with different L_S and brush compositions. Finally, a second smaller process window was observed as W/L_0 approaches 1.5 (36-40nm). As with the process window observed over thin guiding features, the more PMMA-preferential brushes show combinations of W/L_0 and L_S that produce a WRA, but this window begins to disappear for brushes with $f_S > 0.56$. Results with Brush-69 are not shown because random orientation of the assembled BCP was observed on most samples. These trends in thermodynamic process window size indicate that a PMMA-preferential backfill of the pattern is necessary to create conditions that thermodynamically favor a WRA enough to have no other grains present in the final assembly for both thin and wide guiding stripes.

Experimental data were compared with simulation results to gain insight into the effect that the chemical nature of a patterned substrate has on the DSA process of lines-and-spaces. The simulations presented here focus on chemically patterned substrates that result in 3X density multiplication, which is comparable to the guiding patterns used in our experimental work. We investigate the impact that three parameters characterizing the chemical pattern have on the assembly of the block copolymer: guiding stripe width, guiding stripe's preference for the guided species PS, and the backfill's preference for the non-guided species PMMA. While film thickness is a key parameter in the resulting assembled morphology, here it is

fixed at a value of $L_z = 1.28L_0$ in all simulations, which is comparable to the experimental conditions, where the thickness of the AZEMBLY™ PME312 films assembled on the chemical patterns is approximately 32 nm.

In experiments, there are a wide range of unwanted structures that form over patterns where the final assembly would be categorized as a 0, 1, or 2 in Figure 3.5. A commonality amongst many of the defective structures observed in the SEM images analyzed earlier is the presence of lamella grains that are misaligned with respect to the underlying pattern and appear to be oriented perpendicular to the substrate. Figure 3.7 shows an SEM image depicting fingerprint registration of the block copolymer, which is a combination of the coexistence of many grains in one assembly, over a chemical pattern. The areas of misaligned lamella can be of various sizes, and Figure 3.7 shows examples of areas of grains that are at least as large as the simulation box ($6L_0$x$6L_0$). As a first approximation of a pattern's effectiveness for guiding a DSA process, we look at the thermodynamics of different grain orientations to the underlying patterned stripes. We investigated the relative thermodynamic stability of grain orientations over different patterns using thermodynamic integration to calculate the free energy of the meta-stable morphologies (with methodologies previously utilized with the TICG model).[43, 46]

We calculate the free energy associated with going from one thermodynamic state alpha to another state beta by changing a parameter u through the equation,

$$\Delta F_{\alpha\to\beta} = \int_{u_\alpha}^{u_\beta} \mathbf{d}u \Big\langle \frac{\delta H}{\delta u} \Big\rangle \tag{3.5}$$

where $\langle\rangle$ indicates a thermodynamic average. The pathway between states α and β are assumed to form a continuous, reversible path. The pathway used to calculate the free energy of a well-defined morphology from disorder is shown in Figure . The figure shows four branches of the thermodynamic integration scheme, and identifies the state α and β, as well as the three intermediate states along each branch of the pathway. For each morphology

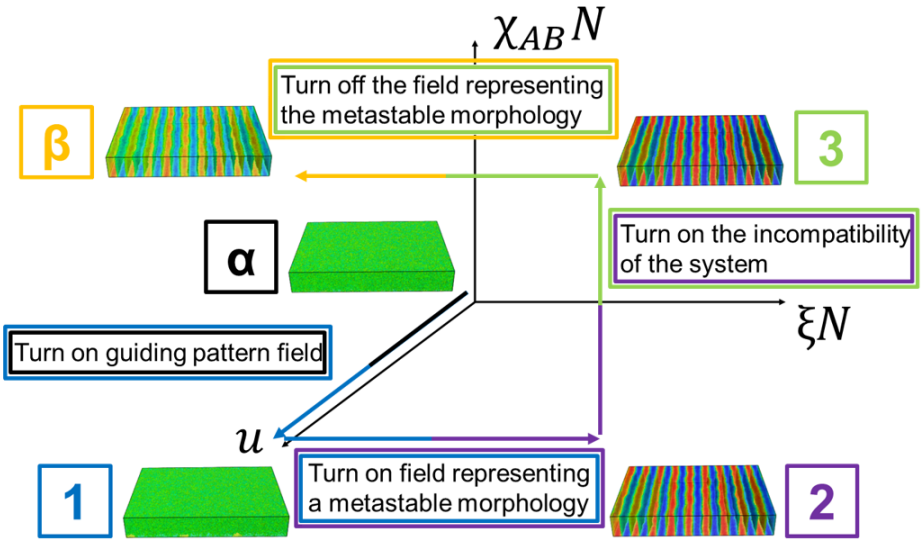

Figure 3.6: The thermodynamic integration cycle used for evaluating the difference in free-energy between an assembled structure and disorder. The first branch turns on the patterned field. The second branch turns on the external field, which matches the morphology of interest. The Flory-Huggins parameter is turned on in the third branch. And the final branch turns off the external field defining the morphology.

considered, the α state is defined as a system comprised of only rouse chains where $\chi N = 0$ and there is no pattern in the simulation box. This serves as a reference point and allows us to compare the free-energies of morphologies that are assembled over different pattern designs. The first stage of the thermodynamic integration involves integrating the pattern field which can be defined by

$$\frac{U_S(\mathbf{r}_i, K_i)}{k_B T} = \frac{\mu \Lambda_{K_i}(x, y)}{d_s} \exp(\frac{-z^2}{2d_s^2}) \tag{3.6}$$

Where μ is a coefficient with bounds at $[0, 1]$. The second branch requires the implementation of an external field that defines the morphology of interest, f_{ext}. It is similar to the patterned field in implementation. The external field is defined as

$$\frac{U_{ext}(\mathbf{r}_i, K_i)}{k_B T} = -\xi f_{ext}(\mathbf{r}_i, K_i) \tag{3.7}$$

where ξ determines the strength of the field, with maximum value ξ_{max} and minimum value of 0. The nature of the external field used here is defined by an order parameter that is a function of the local densities of each species,

$$f_{ext} = \left\langle \frac{\phi_A - \phi_B}{\phi_A + \phi_B} \right\rangle \tag{3.8}$$

The third branch integrates the system over the parameter $w\chi N$, where we increase w from 0 to 1. Finally, we perform the last branch, which is identical to the second, except the integration pathway goes from ξ_{max} to 0. The total free energy change along this pathway can be described by

$$\begin{aligned} \Delta F_{\alpha\to\beta} = \int_0^1 \mathbf{d}\mu \Big\langle \sum_i^{i=nN} \frac{\Lambda_{K_i}(x,y)}{d_s} \exp(\frac{-z^2}{2d_s^2}) \Big\rangle + \int_0^{\xi_{max}} \mathbf{d}\xi \Big\langle \sum_i^{i=nN} -f_{ext}(\mathbf{r}_i, K_i) \Big\rangle \\ + \int_0^1 \mathbf{d}w \Big\langle \sum_i^{i=N_{grids}} V_i \phi_A(i) \phi_B(i) \Big\rangle + \int_{\xi_{max}}^0 \mathbf{d}\xi \Big\langle \sum_i^{i=nN} -f_{ext}(\mathbf{r}_i, K_i) \Big\rangle \end{aligned} \tag{3.9}$$

We initialize the simulations such that the block copolymer is microphase separated into lamella that are perpendicular to the underlying substrate and form an angle θ with the underlying guiding stripe, which we refer to as a misaligned grain (MG), see Figure 3.7. We refer to the case where $\theta = 0.0^\circ$ as a well-registered assembly (WRA), which is the case where the grain is aligned with the patterned features. The simulations are allowed to relax over 5x10^5 MC sweeps to produce metastable morphologies that appear, from a top-down view, to be lines-and-spaces oriented at θ degrees with the guiding feature.

We could only investigate grains at a discrete number of angles θ due to the periodic boundary conditions of the simulation box. By assuming that the block copolymer adopts the natural bulk-domain spacing on average, we are able to investigate $3P + 1$ values of θ, where P is the number of chemical pattern periods contained in a simulation box. A value of $P = 2$ was used in this work, as the increased resolution in θ for $P > 2$ increased computation time. In addition, there are instances in experimental SEM images where grains of the same

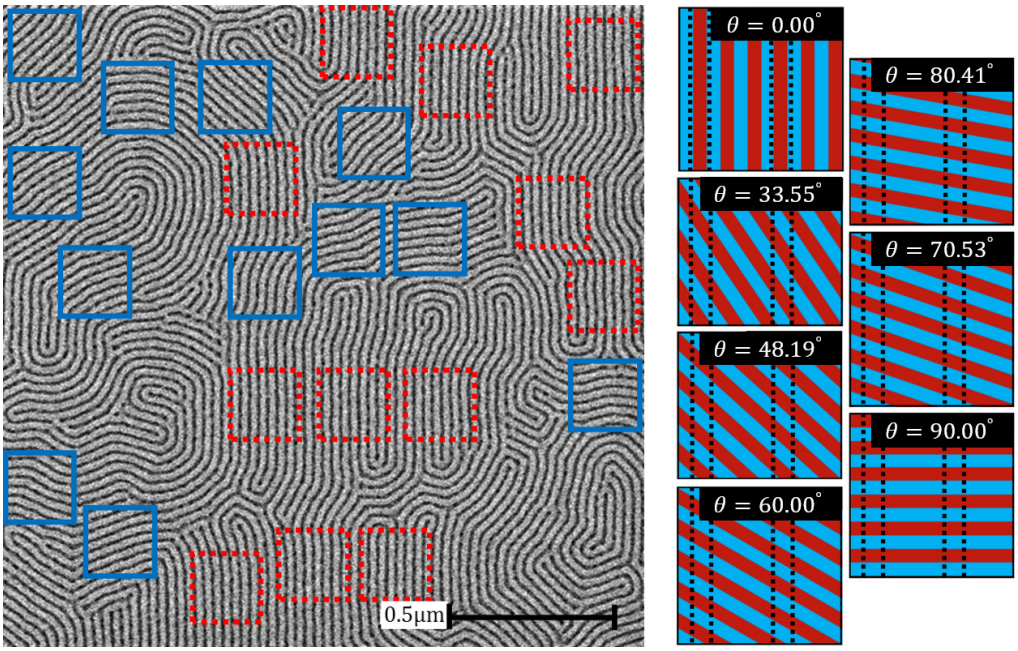

Figure 3.7: On the left is an SEM image of P(S-b-MMA) assembled atop a chemical pattern comprised of guiding stripes for production of lines-and-spaces using density multiplication. A subset of grains that are approximately the size of a simulation box are identified. Areas of the final assembly with misaligned grains are shown within solid blue boxes, while areas with a well-registered grain are within dashed red boxes. Each box has dimensions $6L_0$x$6L_0$. The tiled images on the right show cartoon schematics of the possible angles of rotation, θ, of lamella for two pattern periods. The angles are calculated assuming that average spacing of the lamella is equal to the natural bulk domain spacing, L_0. The dashed, black lines indicate the location and orientation of guiding stripes.

size as a box with $P = 2$ can be found, as shown in Figure 3.7. The values of θ and a schematic demonstrating the assembly over the chemical patterns for each value can be seen in Figure 3.7. For each simulation of a misaligned grain, the simulation box has a height of $L_z = 1.28L_0$ and the box-dimension normal to the direction of the underlying pattern is $6L_0$, such that each simulation contains two periods of the chemical pattern. The third dimension of the box is chosen such that the intialized microphase separated domains have a period of $1.0L_0$. The third dimension for the WRA is always $6.0L_0$. We then perform thermodynamic integration to compute the difference in free energy, ΔF, between an assembly of defect-free lamella perpendicular to the substrate that are oriented at an angle θ to the chemical pattern and defect-free lamella with period $1.0L_0$ confined between two neutral surfaces.

In order to demonstrate the described methodology, we investigate the impact of the guiding stripe on the relative free energy of different orientations of assembled lamella. We selected a chemical pattern with a guiding stripe with strength $\Lambda_S = 0.75$ and a backfill with strength $\Lambda_B = 0.20$. We calculated the relative free-energy for the seven orientations of assembly shown in Figure 3.7. Figure 3.8 shows the comparison of free energy between the WRA and the misaligned orientation with the lowest free energy, which we refer to as the most competitive assembly (MCA). Note that, all of the misaligned orientations have similar energies, but for the purposes of this work only the orientation with the absolute lowest free energy was considered as the MCA. The free energy of the MCA changes linearly with guiding stripe width. The MCA for each W/L_0 may correspond to different rotations of the misaligned grain. This trend can be explained by analyzing the structure of the misaligned assemblies, which adopt a morphology that consists of lamella that are deformed in close proximity to the substrate. In these assemblies, wetting layers of the guided material an unguided material form over the guiding stripe and the backfill, respectively. The larger interfacial energy of the guiding feature ($\Lambda_S > \Lambda_B$) leads to higher interfacial curvature of the lamellar domains over the guiding stripe than over the backfill due to this wetting behavior. The change in guiding stripe width does not cause a qualitative change in the

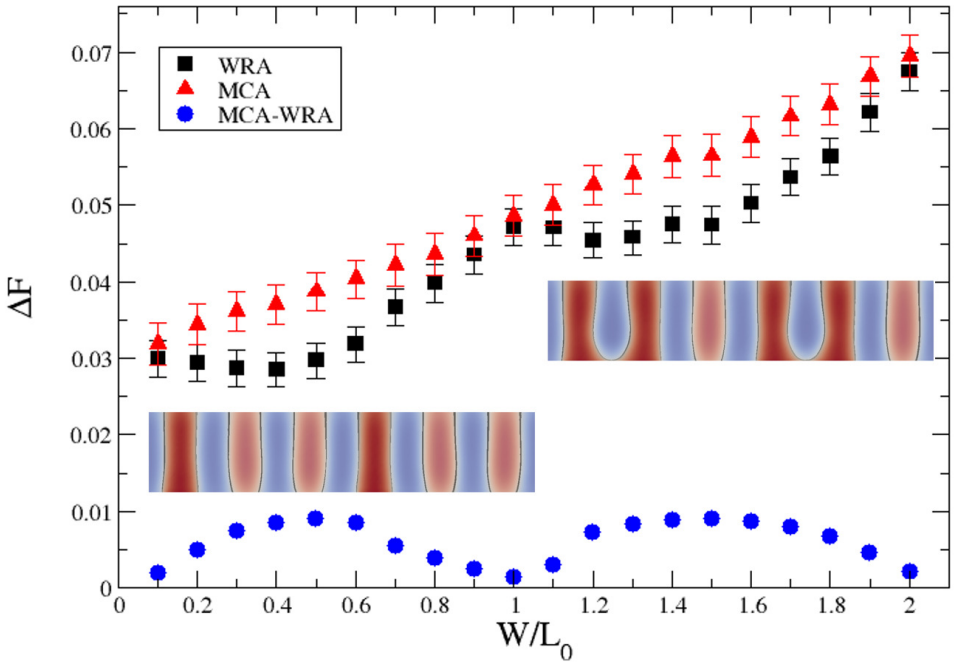

Figure 3.8: The red triangles and black squares show the calculated ΔF in k_BT/chain for the well-registered assembly and the most competitive assembly, respectively, over periodic guiding stripes of width W at a pitch of $L_S/L_0 = 3.0$ for $\Lambda_S = 0.75, \Lambda_B = 0.2$. The blue circles show the difference in the relative free energy of the WRA and the MCA for the corresponding stripe width using $\Delta\Delta F = \Delta F_{MCA} - \Delta F_{WRA}$. The insets show the through-film profile of the WRA at two different guiding stripe widths, $W/L_0 = 0.5, 1.5$. The guided domains are identified in dark red.

assembly for these rotated lamella; however, the increase in the volume of polymer that interacts with the guiding feature results in an increase in the fraction of lamella with larger interfacial curvature, resulting in the observed change in free energy of these structures with guiding feature width.

In contrast, a WRA has a fundamentally different structure over thin and wide guiding stripes. The differences between the two types of structures are demonstrated in the insets in Figure 3.8. For thin guiding stripes, $0 < W/L_0 < 1.0$, the assembly is characterized by a guided block (species A) domain centered over the stripe, while the wider guiding features, $1.0 \leq W/L_0 < 2.0$, have a non-guided block (species B) domain centered. The difference

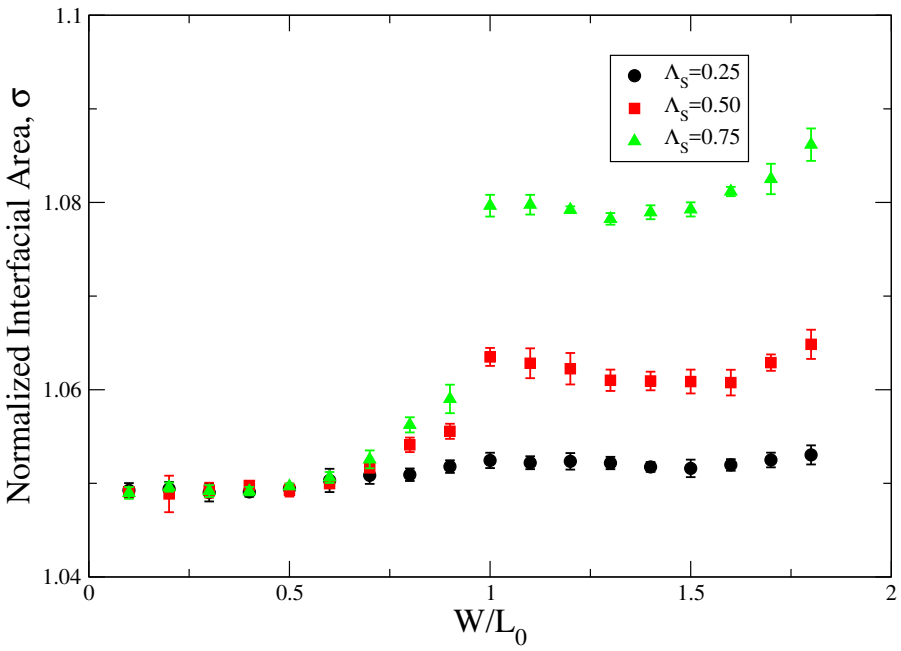

Figure 3.9: Normalized interfacial area, σ, of a WRA over periodic guiding stripes of widths $W/L_0 \in [0.5, 1.5]$ with pitch $L_S/L_0 = 3.0$. The value of σ is found by comparing interfacial area between A and B domains calculated from simulations of a WRA at equilibrium with the calculated A-B interfacial area that would exist if all A and B domains were rectangular prisms.

between these two types of assembly causes a more complicated trend in free energy versus guiding stripe width than that of the misaligned assemblies. The ΔF of the WRA over these chemical patterns results from three interactions: the amount of non-guided material (species B) affected by the guiding stripe, the amount of guided material (species A) affected by the backfill, and the curvature of the AB interface. Greater volumes of non-guided material assembled over the guiding stripe and guided material assembled over the backfill results in a larger enthalpic contribution to the free energy of the assembly. While, larger interfacial areas between A and B domains are associated with a larger entropic contribution.

In addition, Figure 3.8 shows the difference in ΔF associated with the WRA and the MCA, $\Delta\Delta F = \Delta F_{MCA} - \Delta F_{WRA}$, for the defined patterned substrate with a slightly weak guiding stripe and a slightly preferential background region. $\Delta\Delta F$ provides a measure of thermodynamic preference of the chemical pattern for the desired assembly, the WRA. Figure 3.8 shows local maxima in $\Delta\Delta F$ at $W/L_0 = (0.5, 1.5)$. These are the optimal guiding

stripe widths for having the highest thermodynamic preference for a WRA over a misaligned grain for the two fundamentally different assemblies mentioned earlier with the chosen interfacial energies ($\Lambda_S = 0.75, \Lambda_B = 0.20$). Although these two values of W/L_0 have a different material centered upon the guiding feature and the interfacial curvature of the assembled domains is drastically different, the relative values for $\Delta\Delta F$ at $W/L_0 = 0.5$ and $W/L_0 = 1.5$ in Figure 3.8 indicate that the two patterns provide equivalent selectivity for the assembly that appears to be well-registered to the underlying pattern from a top-down perspective. This is a rare situation, where the selectivity is approximately equal at the optimum condition within each processing window. Figure 3.11 shows that for most interfacial energy combinations the selectivity for a WRA is higher for thinner guiding features. While the thermodynamics may indicate that both guiding patterns have the same preference for a WRA over other grain orientations, the nature of the WRA is different and must be considered when designing experimental conditions for industrial applications, as the increased curvature could change the way the assembly affects post-DSA processing.

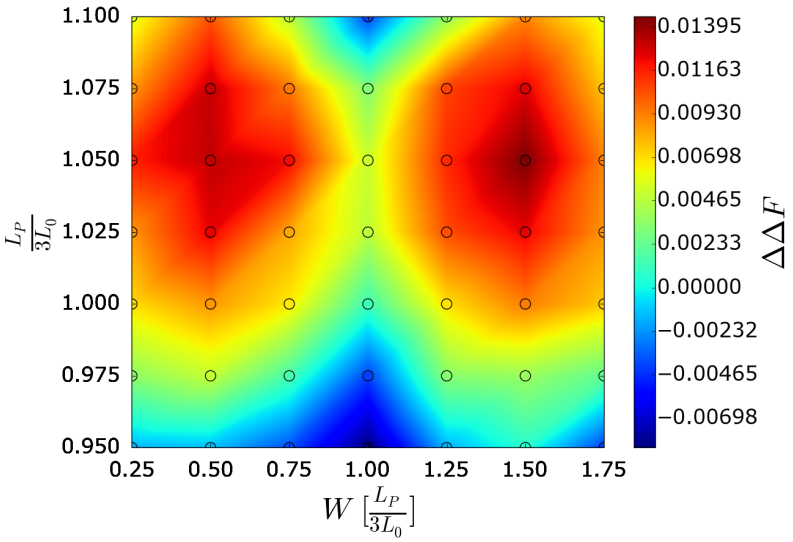

Figure 3.10: A heat map showing the difference in ΔF for the WRA and the MCA as a function of pattern pitch, L_S/L_0 and guiding stripe width, W/L_0, where $\Delta\Delta F = \Delta F_{MCA} - \Delta F_{WRA}$. The guiding stripe strength is maintained at a constant value of $\Lambda_S = 0.75$ and the backfill strength is fixed at $\Lambda_B = 0.2$.

Before investigating the chemistry of the patterned surface, we performed simulations over a range of combinations of periodicity and guiding stripe width. Figure 3.10 shows the $\Delta\Delta F$ for patterns with period of $L_S/L_0 \in [0.95, 1.05]$ and guide stripe widths of $W/L_0 \in [0.25, 1.75]$. Qualitatively, the same trends can be observed as seen in the experimental graphs shown in Figure 3.5. Two process windows can be identified, one centered around thin guiding stripes and the other centered around wider guiding stripes. The simulations predict that there is a higher selectivity for patterns that are wider than the commensurate 3X density multiplication pattern. However, this is not necessarily in contrast to the experimental evidence, as the metric used to grade the effectiveness pattern, lacks the capability to differentiate the patterns which resulted in scores of 3 from one another. The simulations seem to indicate that a higher selection for a WRA occurs at extended patterns, although the experimental window is centered around a compressed pattern period.

In order to better understand the effect of substrate chemistry on DSA, we also examine the guiding stripe affinity for the material to be guided. We fix $\Lambda_B = 0.2$, which models a backfill region that is slightly preferential for the non-guided material. This strength of the guiding stripe Λ_S was varied from 0.25 to 1.25 in 0.25 increments and W/L_0 was varied from 0.00 to 2.00 in 0.25 increments. The same procedure as outlined above was performed to calculate the ΔF and $\Delta\Delta F$ for each set of parameters. Figure 3.11 shows the ΔF vs. W/L_0 of the WRA and the MCA for three of the five different Λ_S values evaluated. For the thinnest guiding stripes with $W/L_0 = 0.25$, there is no statistically significant difference in the free energy of the WRAs between the three guiding stripe strengths. The increased strength is an increase in repulsion of the non-guided material, therefore the enthalpic energy of the system is only increased when the B species interacts with the guiding stripe. Stripes at this width only interact with one A-type domain in a WRA, increasing Λ_S does not cause a significant change in the ΔF because the A-preferential surface only interacts with the small amount of non-guided material that is present in the singular A-rich domain centered on the stripe. Figure 3.9 compares the change in interfacial area for different interfacial energies at various

guiding stripe widths through a normalized interfacial area, σ. This value is calculated by obtaining the average surface area of the interface between A and B domains in one period of the pattern, L_S, obtained from simulations at equilibrium and normalizing that value by the idealized surface area that would exist if each domain were rectangular prisms. The value of σ is never calculated to be 1.0 due to the molecular fluctuations present in the TICG model. However, it can be seen in Figure 3.9, that a larger value of Λ_S causes no statistically relevant change in the average interfacial area of WRA over guiding stripes of width $W < 0.8$. This results in WRAs that are equivalent in relative free energy, as the structure of the assemblies are approximately identical. Larger stripes have more of interaction with the B-species resulting in more perturbation to the WRA, and a larger ΔF. However, rotated assemblies invariably have fractions of the guiding stripe covered by the B-rich domain. The larger repulsion of the B-species that comes with stronger guiding stripes results in an increased wetting of the stripe by the A-species which causes an increase in the curvature of the AB interface. The extra frustration due to a larger amount of curvature at stronger guiding stripes causes the ΔF of these rotated assemblies to increase. The heat-map in Figure 3.11b shows that stronger thin guiding stripes caused an increase in $\Delta\Delta F$ for the Λ_S investigated due to the minimal impact that Λ_S has on the WRA and the higher amount of perturbation of the MCA associated with a stronger stripe.

For wide guiding stripes, where $W/L_0 > 1.0$, the presence of a B-domain over the guiding feature changes the trend in $\Delta\Delta F$ associated with a higher preference of the stripe for the guided material. The preference of the stripe for the guided material causes wetting of the stripe by the A-species, which leads to the larger interfacial curvature of a WRA over guiding stripes of width $W/L_0 > 1.0$ shown in Figure 3.9; at high values of Λ_S the B-rich domain becomes completely disconnected with the substrate. This wetting behavior creates more frustration in a WRA over stronger guiding stripes, as can be seen by the increase in ΔF of the WRA over wide stripes for higher Λ_S in Figure 3.11. Although the trends in ΔF for well-registered assemblies is different for thin and wide guiding stripes, the trend for the rotated

assemblies remains the same in both regimes of stripe width. The maximal $\Delta\Delta F$ over wide guiding stripes was obtained at $\Lambda_S = 0.75$ for the strengths investigated. For the values of $\Lambda_S > 0.75$, there is a decrease in the $\Delta\Delta F$ indicating that the frustration caused by the wetting behavior in the WRA causes the rotated morphologies to become more competitive. It should be noted that at values of $\Lambda_S > 1.25$ the WRA is no longer even metastable, and the simulations predict assemblies of non-bulk morphologies where the guiding stripe is completely wet by the preferred block. The decrease in $\Delta\Delta F$ and the instability of a WRA at high values of Λ_S indicate that the interfacial energy must be more tightly controlled for wide guiding stripes.

These results indicate that a value of Λ_S in the range of 0.5 and 0.75 qualitatively agrees with the experimental results, as Figure 3.11 shows that these two values of Λ_S have high selectivity for a WRA at thin and wide guiding stripes. The simulation results, presented in Figure 3.11, suggest that optimizing the processing conditions to retain the hydrophobicity of the unmodified X-PS could lead to greater thermodynamic selectivity for the BCP to assemble with a high-degree of perfection and improve the process over thin guiding stripes. In contrast, Figure 3.11 also demonstrates that using a more selective material could result in worse conditions for producing a WRA when using wide guiding stripes. In summary, the largest possible $\Delta\Delta F$ between a WRA and its corresponding MCA, that will lead to minimum number of defects, will occur at $W/L_0 = 0.5$. However, if, due to resolution limits or fabrication constraints, such dimensions are difficult to achieve, then a guiding stripe with $W/L_0 = 1.5$ and weaker interaction with the blocks may still result in WRA with a high degree of perfection.

The selectivity of a guiding pattern for WRA is also influenced by the choice of material used in the backfill area, as it was shown in the experimental work. The periodicity of the pattern was set to $L_S = 3.0L_0$, so as to compare directly with the width of the thermodynamic process windows in Figure 3.5. We chose to fix $\Lambda_S = 0.75$, as the guiding stripe chemistry remained constant in the experimental work, and investigated backfill strengths

of $\Lambda_B = [0.0, 0.2, 0.4]$ with W/L_0 from 0.0 to 1.5 by increments of 0.1. This is not a comprehensive exploration of guiding chemistries, but it does give insight into the influence of the backfill interfacial energy on the assembly. Figure 3.12 shows that for both thin and wide guiding stripes, increasing Λ_B results in a larger $\Delta\Delta F$. A backfill that is more preferential for the nonguided material results in a larger ΔF of the WRA due to increased AB-interfacial curvature that results from the wetting behavior of the B-species on the backfill. In addition, stronger backfills cause an increase in the ΔF of the MCA, for the same reason. For every guiding stripe width investigated in Figure 3.12, the MCA is more sensitive to backfill affinity because the geometry of a rotated assembly insures that a larger fraction of the B-rich domain assembles atop the backfill region. This indicates that increasing the affinity for the backfilled area for the nonguided material leads to an increased thermodynamic stability of a WRA relative to a misaligned grain. It should be noted that the backfill can be too preferential, such that parallel lamella become the preferred state, especially for thin guide stripes. However, for moderate values of Λ_B, molecular simulations demonstrate good agreement with experimental findings, where patterns with a PMMA-preferential backfills show greater thermodynamic selectivity for a WRA compared to a misaligned grain.

3.4 Conclusions

The implementation of a chemo-epitaxy flow in an industrial fabrication facility allowed for the systematic investigation and precise control of critical characteristics of chemically nanopatterned substrates. We focused specifically on the effects of guiding stripe width, guiding stripe affinity for the PS, and the backfill affinity for PMMA with a 3X density multiplication pattern that was commensurate with bulk domain spacing of the block copolymer. Top-down SEM images were able to identify two fundamentally different process windows that assembled single-grains with a high-degree of perfection. A new strategy that relies on molecular simulations supported the existence of these process windows by demonstrating maximum thermodynamic driving force for a well-registered assembly when compared to

a competitive misaligned grain at $W/L_0 = 0.5, 1.5$. Free-energy calculations also demonstrated that increasing the affinity of a thin guide stripe for PS increases the thermodynamic selectivity for a single grain aligned with the underlying pattern. The selectivity can be increased for wide guiding stripes, $W/L_0 = 1.5$, by having a higher affinity of the stripe with the guided material; however, if this affinity is too large for these stripe widths where unguided material is centered over the guiding stripe, then the selectivity is reduced until the WRA ceases to be meta-stable. Experimentally the size of these process windows was adjusted by changing the composition of the backfill brush. As PS-content in the brush was decreased, the two process windows in W increased in size. Similarly, we showed through simulations that a backfill that is more preferential for PMMA would have a higher thermodynamic selectivity for the WRA. The results presented here provide a justification for engineering rules that can be used for designing patterns. Although this study does not consider important kinetic aspects of the assembly process, we speculate that by tailoring the interfacial energies and guiding stripe widths according to the rules proposed here, such that the thermodynamic driving force is maximized, patterns can be designed that are more suitable for meeting industrial defect requirements. We finish by emphasizing that when assessing a chemical-pattern for industrial application, the through-film structure must be considered alongside the ease of producing what appears to be the desired assembly from a top-down perspective, and here we also showed that 3D structure can have curvature that may not be noticeable from top-down inspection.

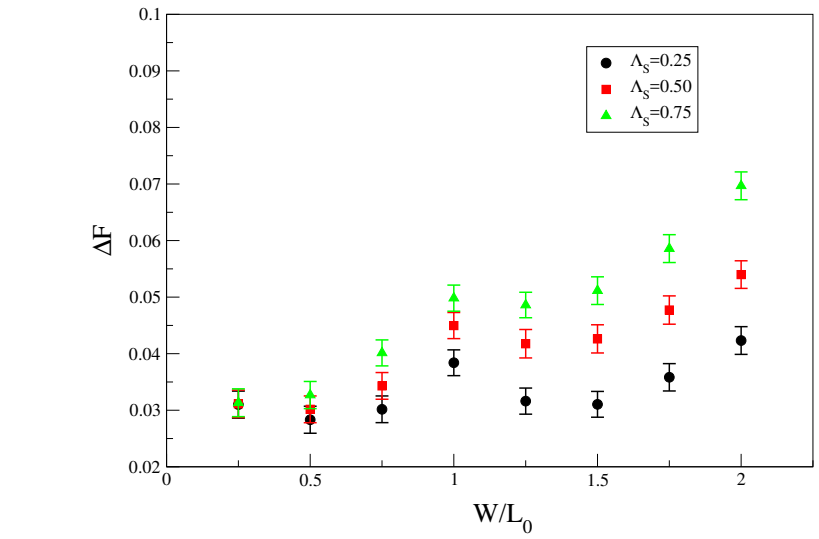

(a)

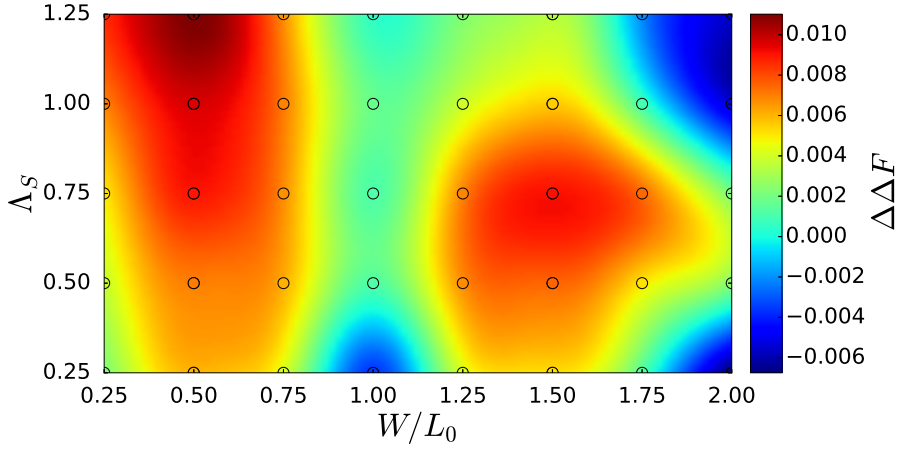

(b)

Figure 3.11: a) The relative free energy difference ΔF in k_BT/chain of the WRA as a function of guiding stripe width, W/L_0, for the guiding stripe strengths $\Lambda_S = [0.25, 0.75, 1.25]$ and $\Lambda_B = 0.2$ for a pattern with periodicity $L_S/L_0 = 3.0$. b) A heat map showing the difference in ΔF for the WRA and the MCA as a function of guiding stripe strength, Λ_S and W/L_0, where $\Delta\Delta F = \Delta F_{MCA} - \Delta F_{WRA}$.

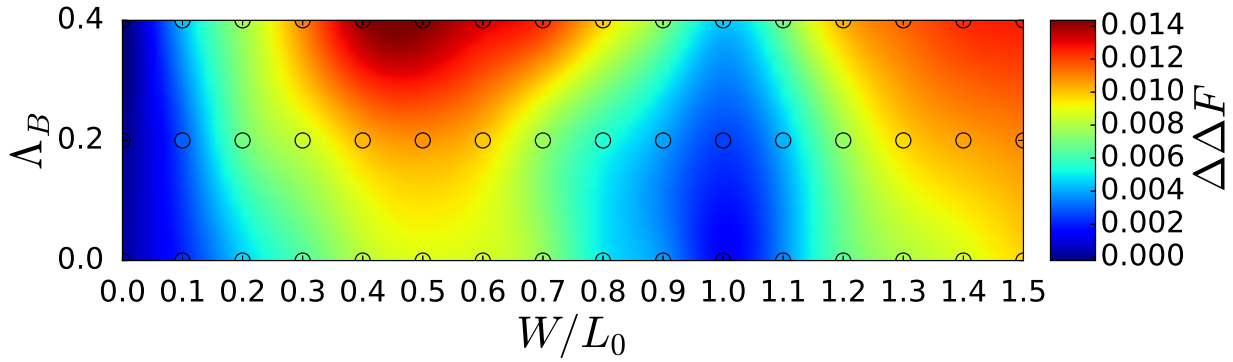

Figure 3.12: A heat map showing the difference in ΔF for the WRA and the MCA as a function of backfill strength, Λ_B and W, where $\Delta\Delta F = \Delta F_{MCA} - \Delta F_{WRA}$. The guiding stripe strength is maintained at a constant value of $\Lambda_S = 0.75$ and the pitch is fixed at $L_S = 3.0L_0$.

CHAPTER 4

ANALYZING THE MECHANISMS OF DEFECT ANNIHILATION IN SINGLE-HOLE CONFINEMENTS USING THE STRING METHOD IN COLLECTIVE VARIABLE SPACE

4.1 Introduction

As conventional optical lithographic techniques reach their resolution limit, and with many of the proposed replacements growing in cost, the directed self-assembly (DSA) of block copolymers has attracted considerable industrial interest as a means to achieve cost-efficient, high-resolution patterning at the nanoscale[47–52]. The DSA process relies on utilizing confinement design and chemically functionalized surfaces, referred to as graphoepitaxy [53–56] and chemoepitaxy [4–7, 57], respectively, in order to coerce a block copolymer morphology into a desired structure. These strategies have proven capable of yielding the assembly of lines[26] and cylinders [58] over large patterned areas [59]. Of particular interest for the fabrication of device-oriented structures is the assembly of cylindrical-phase block copolymers within cylindrical confinements (or "holes"), known as the hole-shrink process [60]. Such a process offers an inexpensive route towards efficient production of vertical interconnect accesses (VIAs) or cut masks [61, 62].

Cylindrical confinements have two unique surfaces: the sidewall of the holes and the circular bottom. The interfacial energy between each surface and each copolymer block needs to be carefully tuned, in concert with the template diameter, to induce the assembly of a desired cylinder. It has been demonstrated that cylinders can successfully form in smaller template diameters if the sidewall preference is for the majority block [63, 64]. However, most theoretical work has focused on cylindrical templates where the sidewall surface is preferentially wet by the minority block of a cylinder-forming block copolymer [65–68]. Peters et al., using a theoretically informed coarse-grained model, demonstrated that increasing

the affinity of the sidewall for the minority block leads to a stabilization of the desired through-film cylinder morphology over other metastable structures[23]. Laachi et al., utilizing a field-theoretic model, have also provided insights into the morphological, kinetic, and thermodynamic differences that exist between non-preferential sidewalls and sidewalls that are preferentially wet by the minority block [69]. These studies collectively support the conclusion that a sidewall that is preferentially wet by the minority block provides a critical boundary condition for obtaining the desired cylindrical morphology. However, given that smaller template diameters have been found to stabilize well ordered cylinders when the sidewall is preferentially wet by the majority block - a reduction from approximately twice the bulk domain spacing to a single bulk domain spacing - additional theoretical study is needed in order to understand assembly under such conditions.

In particular, recent experimental work by Doise et al. has shown that it is possible to experimentally control the wetting behavior of both the sidewalls and the bottom substrate independently, through random block copolymer brushes [70]. This control has allowed for the modification of the wetting behavior of the sidewalls and bottom of the cylindrical confinements separately; furthermore, the random block copolymer brushes allowed for the surfaces to be preferential for either the majority block or the minority block. Through manipulation of the brush composition, these authors demonstrated the ability to use prepattern holes with smaller and larger critical dimensions (confinements with diameters of approximately one and two times the natural domain spacing, respectively) to drive the assembly of cylindrical morphologies. Doise et al. achieved successful assembly at an open hole rate greater than 95% in some cases (as verified via top down SEM after pattern transfer); this relatively high threshold, however, does not meet the defectivity requirements for industrial applications, prompting further questions about how to optimize a prepattern to reduce or avoid defect formation in contact hole-shrink experiments.

The results reported by Doise et al. were generally in good agreement with predictions by Peters et al. but, at the experimental level, confinement still led in some cases to defective

assembly. The work of Peters et al. provided a qualitative understanding of which design rules are necessary for stabilizing a cylindrical morphology, but only considered the final -equilibrium- states reached in a simulation, without addresing how defective states form and remain stable, or how transitions between defective states occur. Recent work by Li et al., Hur et al. and Laachi et al. has shown that a string method can be used in coarse grained [24, 84] and field theoretic models [66, 69, 71], respectively, to analyze transition pathways in block copolymer systems. These works provided an understanding of transitions between competitive structures in thin films and in cylindrical confinement, but did not address how the formation of competitive, metastable states might interfere with morphology formation. In addition, in the context of exploring the transition between defective states and through film cylinders in contact holes, the work of Laachi et al. only explored a limited number of pre-pattern configurations, and did not consider how optimization of the prepattern might influence defectivity.

Here, we utilize a theoretically informed coarse grained model for block copolymers, which has been shown to be in good agreement with experiment in past work, to explore the emergence of metastable states within cylindrical confinements with a critical dimension of approximately one domain spacing. Subsequently, we use the string method to analyze the transition between competitive states, uncovering the free energy barriers opposing the transition from metastable defects to through-film cylinders. The influence of the strength of the affinity of the sidewall and bottom substrates on these free energy barriers is also considered. We find that in a large sample of simulations repeated at the same set of conditions, different final morphologies appear, including defects and through film cylinders, indicating template conditions which stabilize various morphologies. Transition pathways calculated at prepattern conditions in the vicinity of these regions, where several different morphologies occur, reveal that significant free energy barriers exist that oppose the annihilation of defects, even if the defective states have a significantly higher free energy.

4.2 Models and Methods

The simulation results presented in this work are based on the standard theoretically informed coarse-grained model[18, 72, 73], which represents block copolymer chains n Gaussian chains which are discretized into N beads connected by harmonic springs in a fixed volume V at a fixed temperature T. This model has previously been shown to be in quantitative and qualitative agreement with experimental results [17, 43]. In this model, the energy associated with the polymer bonds is expressed as

$$\frac{H_b[\{\mathbf{r}_i(s)\}]}{k_B T} = \frac{3}{2b^2} \sum_{i=1}^{n} \sum_{s=1}^{N-1} [\mathbf{r}_i(s+1) - \mathbf{r}_i(s)]^2 \tag{4.1}$$

where the s^{th} bead on the i^{th} chain has position $\mathbf{r}_i(s)$. R_e is the end-to-end distance of the polymer chains; typically, a unit system is adopted for the simulations where the end-to-end distance is unity. Additionally, k_B is the Boltzmann constant. The energy associated with non-bonded interactions is given as

$$\frac{H_{nb}[\phi_A, \phi_B]}{k_B T} = \frac{\sqrt{\overline{N}}}{R_e^3} \int_V d\mathbf{r} [\chi_{AB} N \phi_A \phi_B + \frac{\kappa N}{2} (1 - \phi_A - \phi_B)^2] \tag{4.2}$$

where $\sqrt{\overline{N}} = \frac{\rho_0 R_e^3}{N}$, the interdigitation number, is an estimate of the number of chains a given chains interacts with (ρ_0 is the average bulk number density of beads). The parameter χN is the Flory-Huggins parameter governing the incompatibility of the two blocks, and κ^{-1} is proportional to the melt compressibility. Each term $\phi(r)$is a function of the local density of each type of bead; these densities are calculated by a particle-to-mesh (PM_0) scheme, where the underlying grid is comprised of cubic cells with side length ΔL.

The cylindrical confinement is modeled as being composed of hard walls; the sidewall

and bottom substrate interact with the polymer according to the term

$$\frac{H_S}{k_B T} = \sum_{i=1}^{nN} f_s(x, y, K) \frac{\Lambda^K}{N d_s} \exp(\frac{-z^2}{2 d_s^2}) \tag{4.3}$$

where K is the type of monomer bead; the term $f_s(x, y, K)$ adopts the values of either -1 or 1, depending on the value of K and the position of the bead. Λ^K defines the strength of interaction between the surface and the bead; when a bead of type A is in a position preferable to type B, the overall energy contribution should be positive, and $\Lambda^A = -\Lambda^B$. Lastly, z is the distance to the surface, and d_s is the decay length of the potential. Both the sidewall and the bottom surface contribute a term of this form. The model is implemented in the context of a Monte Carlo simulation. Configurations are sampled according to the Metropolis criterion, where the probability of accepting a trial configuration is given by $p_{acc} = \exp(-\Delta H/(k_B T))$. Trial configurations are proposed using two different Monte Carlo moves; single bead displacement and chain reptation.

To find the minimum free energy pathways between two states of interest, we make use of the string method described mainly by Maragliano et al. [74–84] A string of states is constructed connecting the two states; each state along the string, or image, is a unique morphology. The string is mathematically described as $\mathbf{m}(\alpha)$ where α is the reaction coordinate ($0 \leq \alpha \leq 1$). The images are vectors, each component m_i of which is a function of an order parameter constructed from the local densities on a grid. At each point r_i in the grid, $m_i = \frac{\phi_A(r_i) - \phi_B(r_i)}{\phi_A(r_i) + \phi_B(r_i)}$. This quantity represents the normalized density differences between beads of type A and B in a volume ΔL^3 around each point r_i in the grid spanning the entire simulation box.

The condition for the string to be the MFEP is that the perpendicular component of the gradient of the mean force along the string must be zero everywhere. The potential of mean

force on the string, defined at each image, is given by

$$F(\mathbf{m}) = -k_B T \ln \int d\{\mathbf{r}^{nN}\} \exp(-\frac{H}{k_B T}) \delta[\mathbf{m} - \hat{\mathbf{m}}]. \tag{4.4}$$

In this equation, $\hat{\mathbf{m}}$ indicates the order parameter vector constructed from the particle coordinates $\{\mathbf{r}^{nN}\}$. The MFEP satisfies $\nabla_\perp F(\mathbf{m}) = 0$, which means that the variation perpendicular to the path is zero everywhere along the path. The mean force is numerically calculated via umbrella sampling with a harmonic restraint; the total Hamiltonian has the additional term

$$\frac{H_c}{k_B T} = \frac{\lambda}{2} \int_V d\mathbf{r} [\mathbf{m} - \hat{\mathbf{m}}]^2 \tag{4.5}$$

where λ is a spring constant which controls the strength of the training potential. In the limit of an infinitely large spring constant, the free energy of the restrained system converges to the free-energy functional $F(\mathbf{m})$. Using a spatial grid to evaluate the integral in the umbrella potential, the differential of free energy with respect to $\mathbf{m}$ goes to $\frac{\delta F}{\delta \mathbf{m}} = \lambda \Delta L^3 k_B T [\mathbf{m} - \langle \hat{\mathbf{m}} \rangle_c]$, where $\langle \hat{\mathbf{m}} \rangle$ is averaged over many MC steps. Therefore, the string is updated every iteration according to $\mathbf{m}_{k+1} = \mathbf{m}_k - \tau \lambda \Delta L^3 [\mathbf{m}_k - \langle \hat{\mathbf{m}} \rangle_c]$, where τ is a time constant controlling the frequency at which the string is updated. As described in Maragliano et al., the images are redistributed after every iteration to avoid the images falling into the minima of the free energy landscape [78].

The string is discretized into 128 nodes, each of which is an independent MC simulation used to estimate the mean force along the string. The free energy along the string can be determined from the free energy estimation method outlined in Maragliano et al. [78] The strings were initialized as linear interpolations in collective variable space between a defective morphology (or a disordered melt), $\alpha = 0$, and a through-film cylinder, $\alpha = 1$. These states were chosen from independent MC simulations. When calculating pathways between defects and ordered cylinders, the ends of the string are free to move, ensuring the ends represent local minima.

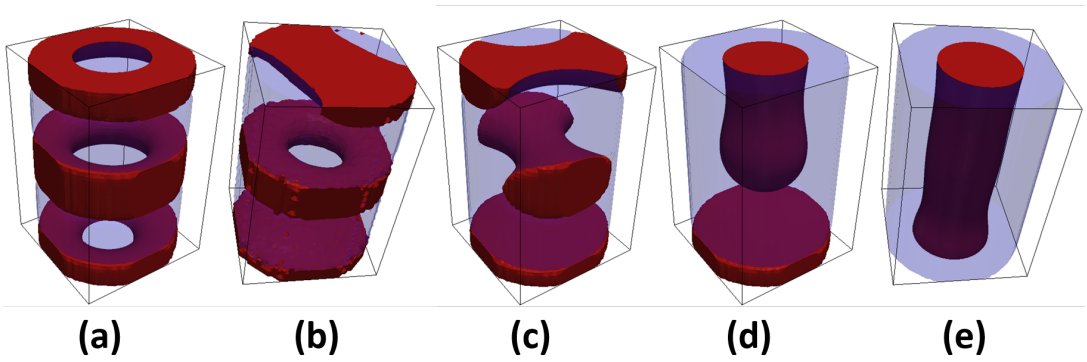

Figure 4.1: A compilation of the well-defined morphologies that were stabilized from independent Monte Carlo simulations of cylinder forming block copolymers. The dark, red phase represents the minority-block rich domain, while the light blue phase is the majority-block rich domain. The morphologies observed were (a) the double donut, 2D, (b) the donut-bar, DB, (c) the double bar, 2B, (d) the disconnected cylinder, DC, and (e) the cylinder.

4.3 Results and Discussion

he cylindrical confinement for guiding the DSA process utilizes chemoepitaxy and graphoepitaxy to drive the assembly of cylindrical features that span the height of the confinement. The simulations in this work focus on perfectly cylindrical confinements that are filled with poly-styrene-b-(methylmethacrylate), PS-b-PMMA, with a styrene volume fraction of $f_{PMMA} = 0.3$. We assume that the surfaces that produce the confinement, the vertical sidewall and the circular bottom, are unique in terms of their affinity for the polymer; thus, the block copolymer that is deposited inside the hole is assumed to have an independent interfacial energy with each surface. The strength of these interfacial energies is governed by the constants Λ_{SW} and Λ_B for the sidewall and bottom surfaces, respectively, and the surfaces interact with the polymer via the potential described above, where z is the distance between a polymer bead and the closest (normal) point on the given surface. A negative value indicates a preference for the minor block, poly-(methyl methacrylate), PMMA, and a positive value indicates a preference for the major block, poly-styrene, PS.

We performed a number of independent Monte Carlo simulations to investigate the impact of the combination of these parameters on a predicted morphology for constant confinement

Table 4.1: Stable morphologies that exist at intersections in design space

Λ_{SW}	Λ_B	**Stable Morphologies**
0.1	-0.1	2B, 2D
0.1	-0.6	DB, 2B
0.4	-0.2	2B, C, DC
0.3	-0.6	2B, DC
0.6	-0.5	C, DC

dimensions. A height of 62 nm, $1.67L_0$ and diameter of 43 nm, $1.16L_0$, were chosen in order to be in agreement with the experimental conditions used by Doise et al.[70]. These values were well in the region of the design space that resulted in the desired cylindrical morphology (at least when viewed from a top down perspective, experimentally). Using this geometrical confinement, we set the interfacial energy constants to be $0.0 \leq \Lambda_{SW} \leq 1.0$ and $-1.0 \leq \Lambda_B \leq 0.0$. In this work, the sidewall is assumed to be preferential for PS (or neutral) and the bottom for PMMA (or neutral); again, this is in qualitative agreement with the experimental setup of Doise et al. [70] The simulations were run for 500,000 Monte Carlo sweeps to find the stable morphologies at each interfacial energy combination.

The results of these simulations revealed that five unique, well-defined morphologies were stable within this range of parametric combinations. A 3D rendering of those morphologies can be seen in Figure 4.1, which includes the double donut (2D), the donut-bar (DB), the double bar (2B), the disconnected cylinder (DC), and the full cylinder (C). In some confinements, only one of these morphologies was stable across the set of simulations; however, there were many cases where more than one morphology was stable. This implies that either the states have comparable free energies, or that the stabilized morphologies represent kinetically trapped metastable states. Figure 4.2 shows a diagram that illustrates which morphologies were stable at each parametric combination of interfacial energies. The interfacial energy combinations that stabilize multiple morphologies are denoted by the large beige circles surrounding the markers in Figure 4.2 - these combinations are seen at the intersection of the areas of parameter space that stabilize only one structure. The points at these intersections have as potentially stable states the morphologies that are singularly

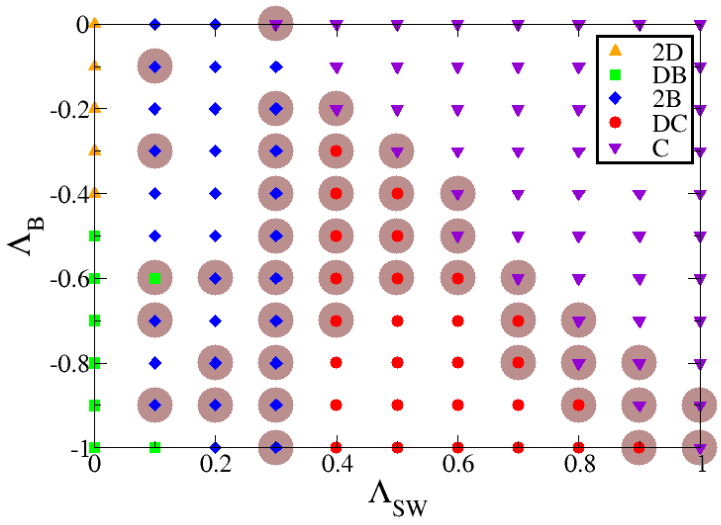

Figure 4.2: A phase diagram that shows which morphologies were most likely to form at a given combination of sidewall preference for the majority block, Λ_{SW}, and bottom preference for the minority block, Λ_B. Each combination of interfacial energies is given a marker that identifies which morphology was observed most often after 10 independent Monte Carlo simulations. The large beige circles denote interfacial energy combinations that resulted in multiple stable morphologies. The absence of a beige circle means that only one type of morphology was stabilized. The morphologies observed can be seen in Figure 4.1, and include the double donut (2D) denoted by orange upward pointing triangles, the donut-bar (DB) denoted by green squares, the double bar (2B) denoted by blue diamonds, the disconnected cylinder (DC) denoted by the red circles, and the cylinder (C) denoted by the violet downward facing triangles.

stable in the adjacent areas of design space. Examples of these intersections exist at the combinations of $(\Lambda_{SW}, \Lambda_B)$ listed in Table 4.1. One of the interesting combinations of interfacial energies occurs around the "triple point", where the conditions that stabilize the double bar, the disconnected cylinder, and the cylinder morphologies coincide. At the values of $\Lambda_{SW} = 0.4, \Lambda_B = -0.2$ the Monte Carlo simulations yield formation of all three of the aforementioned morphologies.

At this "triple point", where multiple possible stable states result arise in simulations, we can extract useful thermodynamic and kinetic information about their relative stability using the string method. We chose to analyze the transition pathway between a defective morphology and a cylinder beginning at the "triple point" ($\Lambda_{SW} = 0.4$ and $\Lambda_B = -0.2$),

then subsequently in its immediate vicinity in parameter space. This provided the opportunity to analyze the annhilation pathway for two different defects, the double-bar and the disconnected cylinder within a single confinement design.

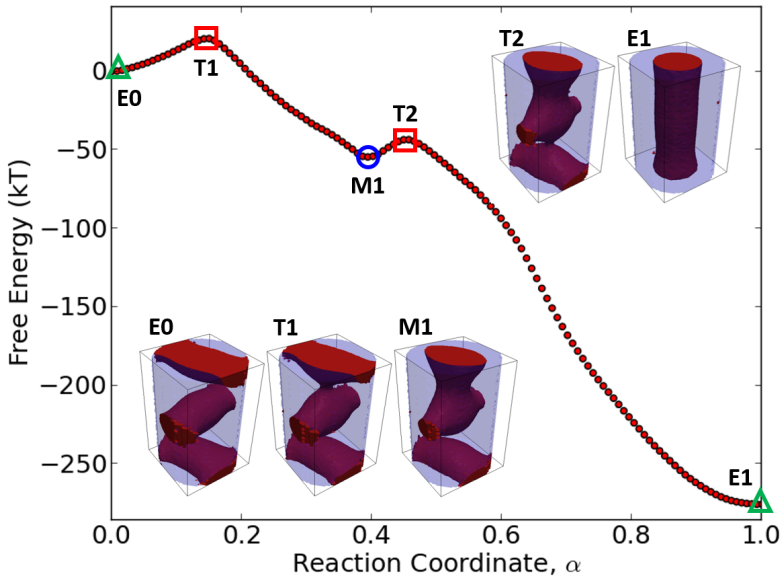

Figure 4.3: The transition pathway along the reaction coordinate α between a double bar morphology and a cylinder with $\Lambda_{SW} = 0.4, \Lambda_B = -0.2$. The green triangles identify the end nodes of the string, the red squares identify the nodes of the string where the transition states occur, and the blue circles identify the location of the metastable states along the pathway. Graphics of the morphologies corresponding to the labeled nodes are included.

First, we investigated the transition pathway between the double-bar and cylindrical morphologies using the string method. Figure 4.3 shows the MFEP calculated from the string between a double-bar structure ($\alpha = 0$) and the through-film cylinder ($\alpha = 1$) within a cylindrical confinement with $\Lambda_{SW} = 0.4$ and $\Lambda_B = -0.2$. Two clear transition states can be identified along this pathway. The first transition state is approximately $30 k_B T$ higher in free energy compared to the metastable defect, and it corresponds to the formation of a PMMA bridge linking the upper and middle bars. For this bridge to form, a certain number of PMMA chains must diffuse through a layer of PS, a highly unfavorable and unlikely event - hence, the large barrier. Following the initial bridge formation, however, polymer can diffuse more easily through the bridge, corresponding to the downhill descent in free energy. The

second transition state is approximately $15k_BT$ higher in free energy compared to the nearby metastable state, and it corresponds to the formation of a second PMMA bridge between the layer of polymer at the bottom and the growing PMMA structure in the middle. Just as was the case for the first bridge, the diffusion of the first few PMMA chains through the layer of PS is unfavorable, and so the free energy barrier is large. Once that process is initiated, however, there are no more free energy barriers, and polymer simply diffuses through the established bridges to form a well-ordered, complete cylinder.

It is of interest to consider why the opposite pathway is not favored - that is, the bottom bridge forming first, followed by the upper bridge. If the bottom bridge formation occurred first, it is expected that the first free energy barrier would be even higher because, in addition to requiring the same number of chains to diffuse the same distance, PS would be forced (due to the volume-filling nature of the model) to occupy space near the bottom substrate, a situation that is enthalpically unfavorable. This presumably large free energy barrier is circumvented when the system first forms the upper bridge; this also creates a bulge in the PMMA in the center of the system. Thus, when the bottom bridge does form, it need not traverse as great a distance, making up for the enthalpic penalty of forcing PS onto the bottom substrate. While this effect would likely be observed in the opposite pathway as well, it is the avoidance of the first very large barrier that is expected to be most critical.

Next, we fixed the end states of the string to be the disconnected cylinder and the complete cylinder morphologies. The calculated MFEP for the annihilation of this defective morphology can be seen in Figure 4.4. The MFEP for annihilation of the disconnected cylinder is similar to the last half of the annihilation of the double-bar, including a transition state that is approximately $20k_BT$ higher than the metastable defect. Likewise, this free energy barrier corresponds to the formation of a PMMA bridge between the bottom layer and the disconnected cylinder, requiring the unfavorable diffusion of PMMA through a PS layer. Indeed, it can be observed in Figure 4.3 that a metastable morphology very much like that corresponding to the disconnected cylinder exists in the middle of the pathway.

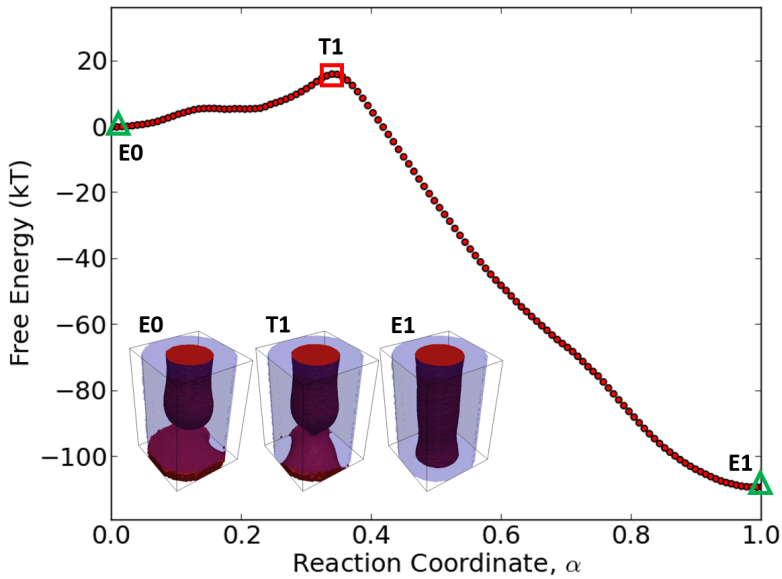

Figure 4.4: The transition pathway along the reaction coordinate α between a disconnected cylinder morphology and a cylinder with $\Lambda_{SW} = 0.4, \Lambda_B = -0.2$. The green triangles identify the end nodes of the string, the red squares identify the nodes of the string where the transition states occur, and the blue circles identify the location of the metastable states along the pathway. Graphics of the morphologies corresponding to the labeled nodes are included.

It is now clear that these defective morphologies are not competitive at equilibrium, but instead represent long lived kinetically trapped states. Despite the fact that a confinement design can be conceived to thermodynamically favor formation of a complete cylinder, there can simultaneously exist significant barriers that must be overcome if the assembly process initially leads to an undesirable, meta-stable structure. In an attempt to understand how design parameters affect these barriers, we performed string calculations for several interfacial energy combinations.

Figure 4.5 shows the effect that the sidewall interfacial energy has on the transition barriers by varying the value of $\Lambda_{SW} = \{0.3, 0.4, 0.5\}$ while $\Lambda_B = -0.2$. There is a significant reduction in the free energy barriers associated with both transition states as the sidewall becomes more preferential for the majority block, PS. Meanwhile, the free energy barriers grow much larger if the interaction parameter on the sidewall becomes more weakly preferential for PS.

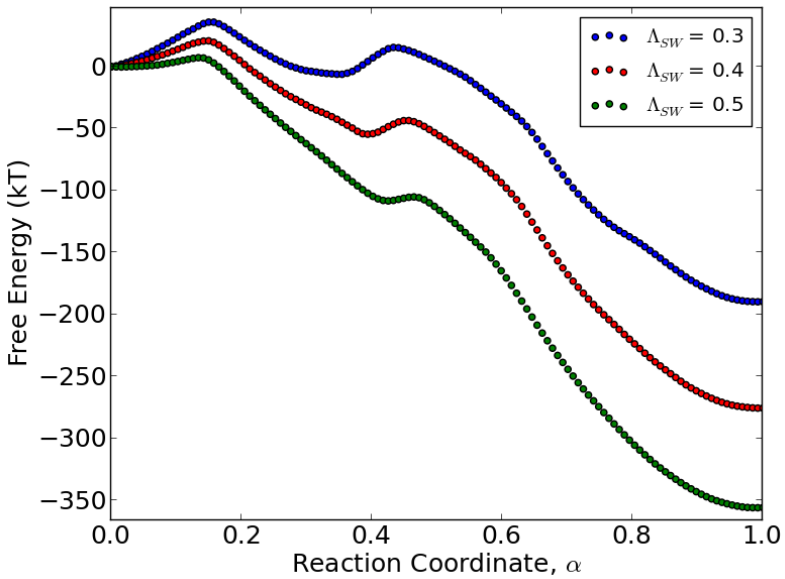

Figure 4.5: Three transition pathway along the reaction coordinate α between a double bar morphology and a cylinder with $\Lambda_B = -0.2$ where the sidewall interfacial energy is varied between $\Lambda_{SW} = \{0.3, 0.4, 0.5\}$.

Figure 4.6 also shows how the MFEP changes when the interfacial energy corresponding to the interaction between the bottom of the confinement and the polymer changes if we use $\Lambda_B = \{-0.1, -0.2, -0.3\}$ while $\Lambda_{SW} = 0.4$. In contrast to the sidewall interfacial energy, the bottom of the confinement has only a small effect on the barrier heights of the transition states. The first transition is virtually unaffected, and there is a minor influence on the height of the second free energy barrier. As discussed previously, part of the barrier associated with this latter transition is the forcing of PS to the bottom substrate as PMMA diffuses to the center. If the bottom substrate is less hostile to PS, there is less of a penalty associated with this transition. Furthermore, this observation also explains the reduction in the thermodynamic free energy difference between the two-bar structure and the full cylinder. The volume of PS wetting the bottom surface is greater in the full cylinder morphology than the two-bar morphology; increasing the preference for PMMA of the bottom surface therefore causes a greater perturbation to the free energy of the full cylinder morphology, resulting in the reduction in thermodynamic preference.

The simulation results in Figure 4.5 and Figure 4.6 show that the two unique surfaces

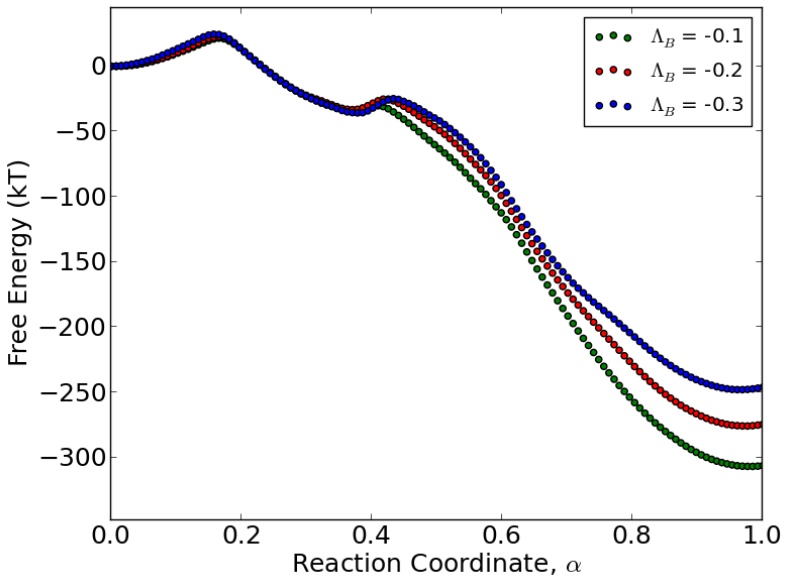

Figure 4.6: Three transition pathway along the reaction coordinate α between a double bar morphology and a cylinder with $\Lambda_{SW} = 0.4$ where the bottom interfacial energy is varied between $\Lambda_B = \{-0.1, -0.2, -0.3\}$.

comprising the guiding confinement have different effects on the thermodynamics and kinetics of the hole shrink process. These results indicate that it is more important to control the sidewall surface characteristics when trying to minimize the kinetic barriers that exist between defective states such as the two-bar structure and the desired full cylinder morphology. This follows intuition, as the full cylinder morphology needs the majority phase to wet the entirety of the sidewalls of the confinement for the cylinder to exist.

This provides evidence that if a sidewall surface can be designed that exhibits a sufficiently strong preference for the majority block, then the MFEP towards the desired cylindrical morphology is void of unwanted meta-stable morphologies. It is likely that continuing to increase the sidewall preference for the majority block will improve dynamics of assembly, as well as the thermodynamics. It is our belief that many pathways, including those that pass through defects and those which do not, remain competitive regardless of which is most probable. Therefore, continued increase of the sidewall preference for the majority block is likely to make defect-free pathways progressively more probable. Quantifying this effect is a future direction of interest.

The comparison of the MFEP for different patterning combinations seems to suggest that the bottom of the cylinder does not affect the relative selection for the desired cylinder over defective structures as much as the side walls. This provides an opportunity to improve upon the design of the patterned hole. A homogeneous bottom surface does not provide any method for assuring the location at which the cylinder contacts the bottom surface. This placement accuracy can be crucial when considering the usefulness of the technology for industrial application. If the hole-shrink process is to be used for VIAs, then a design strategy must be employed to guarantee that the BCP cylinder is in contact with the desired circuit feature. Here we propose a confinement hole with a stripe imprinted onto the bottom surface to control the placement of the cylinder contact. The stripe is assumed to be preferentially wet by the minority domain, so as to drive the cylinder to wet at the stripes location.

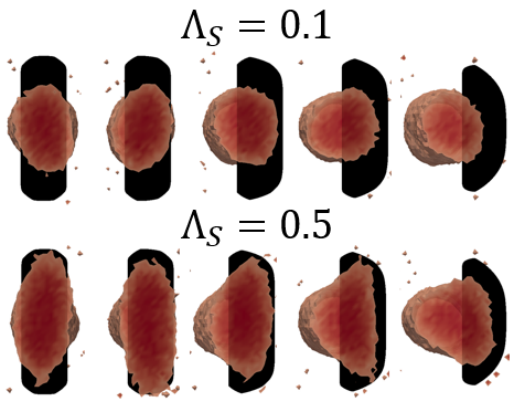

Figure 4.7: A bottom up view of the morphology assembled within a cylindrical confinement with a guiding stripe feature at the bottom of the patterning hole. The sidewall of the confinement has preference for the majority block with strength $\Lambda_{SW} = 0.4$. The stripe's preference for the minority block is constant across the rows and is labeled above the rows as Λ_S. The black band represents the locations of the guiding stripe, and as you move across the row of images, the stripe increases its offset from the center of the patterned hole.

Figure 4.7 shows a bottom-up view of this type of confinement, where a black stripe is located at the position of the guiding feature. A side view is omitted, as all of the morphologies resemble complete cylinders; the difference between the assemblies occurs only near the bottom of the confinement. For these simulations, $\Lambda_{SW} = 0.4$ so as to reduce

the likelihood of defective states. Note in Figure 4.7 that multiple bottom-up images are shown, where the guiding feature is centered at different locations relative to the center of the cylindrical confinement. This is done to model possible offsets that can occur when matching contact holes to the features that the VIAs are supposed to connect. A confinement that is suitable for this industrial application should be able to rectify the inevitable variations that will occur in pattern production, and provide the desired contact.

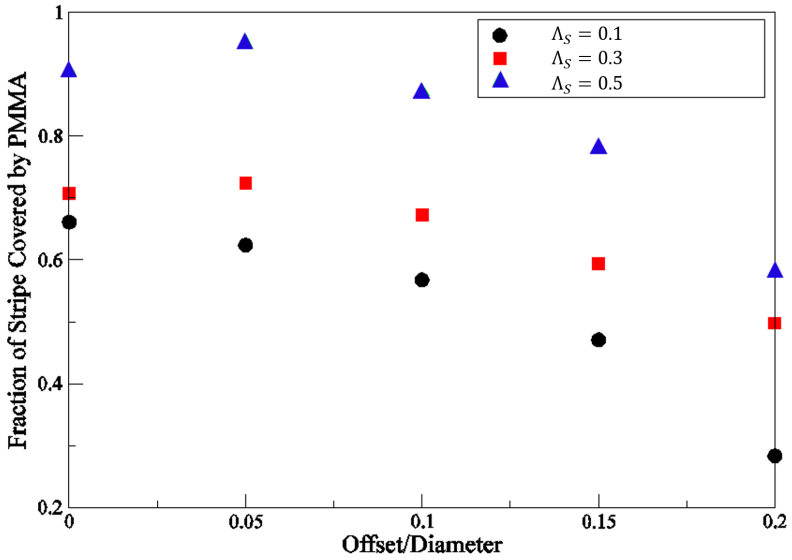

Figure 4.8: The fractional coverage of the guiding stripe at the bottom of the confinement hole by the assembled cylinder as a function of the stripe's offset to the cylindrical confinement. Three different guiding stripe strengths are shown.

The top row of bottom-up images is of a confinement, where the stripe has preference $\Lambda_S = 0.1$, while the bottom row is of a stronger guiding feature, $\Lambda_S = 0.5$. There is a qualitative difference between the structure of the morphology that can be seen from this view point. Intuitively, the more preferential stripe causes a larger wetting area of the assembled cylinder, which can be seen clearly in the far-left image, when the stripe is centered with respect to the contact hole. This causes a higher amount of perturbation to the overall structure, creating an almost T-like shape. Figure 4.8 shows the fraction of the stripe that is wet by the minority-rich domain. The higher perturbation caused by

the higher preference drives increased coverage of the feature by the minority-rich domain, regardless of the position of the guiding feature relative to the contact hole. This implies that designing contact holes with a highly preferential stripe-like feature will help increase placement accuracy and drive the formation of morphologies that serve as functional VIAs regardless of industrial process variability.

Furthermore, we acknowledge that increasing the wetting behavior within a simulation is different than what can be done in experimental systems. While there are kinetic and thermodynamic benefits to using highly preferential sidewalls for the majority block, there is no guarantee that an experimental confinement can be designed to be selective enough to realize the elimination of metastable states along the most probable path for cylinder formation. In addition, the design of confinements in which there is a guiding stripe feature at the bottom is accompanied by a plethora of challenges. However, by attempting to incorporate these designs into experimental confinements can improve defectivity as well as placement accuracy.

4.4 Conclusions

The systematic study of the single-hole shrink process where the sidewalls are wet by the majority block of a cylinder forming block copolymer have allowed for the identification of the metastable states that may arise depending on confinement design. Subsequent application of the string method has enable a detailed analysis of the transition pathways between defective states and the desirable through-film cylindrical morphology; specifically, the study of a single design chemistry where three different morphologies were stabilized in independent Monte Carlo simulations: a double-bar, a disconnected cylinder, and a complete cylinder. The complete cylinder was identified to be the morphology with the lowest free-energy of the three; however, the transition pathway between the desired morphology and the defects was found to exhibit significant energetic barriers of approximately $30k_BT$. This finding provides insights into the challenges associated with reaching industrial defect standards,

as the diffusion events necessary to transition from a defect to a cylinder are unlikely to occur if the system ends up in a defective state. Altering the sidewall chemistry has been shown to have a much more significant impact on these pathways than the chemistry of the bottom surface. As the sidewall becomes more preferential for the majority block, the number of metastable states that exist in the pathway is reduced until, for a sufficiently strong preference, the MFEP proceeds downhill, going straight to the desired cylindrical morphology. We note that the string method used to find this pathway is only able to identify a single, most probable transition path, and does not speak to the relative probability of proceeding down this path. However, the demonstrated ability to fundamentally change the most probable path using confinement design is promising, as it implies that if the sidewalls of these confinements can be created to be highly preferential for the majority block, the resulting hole-shrink process will be better suited to meet industrial defect standards.

CHAPTER 5

CONCLUSION AND FUTURE WORK

The works presented here were an attempt to understand the effects that nanoscale pattern design has on the directed self-assembly of block copolymers for industrial application. First, we investigated the assumption about substrates that block copolymers are deposited upon in thin-films that was made by previous works. Prior to the work presented in Chapter 2, the TICG had been used with substrate models that approximated the surface-polymer interaction as that of a hard surface that is impenetrable by the coarse-grained beads. However, in experimental systems, the substrate is often partly composed of polymer brush material which will penetrate into the deposited polymer melt, and vise-versa. Therefore by creating a model which uses an explicit polymer brush as the guiding surface, we were able to show that the approximation made by previous works is able to qualitatively reproduce the same behavior. The difference between the two models is shown to be in the under-estimation of the lateral range of interaction (width) of the preferential guiding feature. The soft substrate shows that the ability for a brush to penetrate into the neighboring areas, causes a smearing effect that creates an effectively wider guiding feature. While the methodology presented here is useful, a more advanced fitness function can be developed to allow for better recovery of the morphologies assembled over guiding stripes with widths of $W/L_0 < 0.8$ and $W/L_0 \geq 0.8$ using the same parameter set for the GPM.

In Chapter 3, we move on to investigating the role that chemical and geometrical designs of substrates have on the self-assembly process for lamella forming patterns. A thermodynamic explanation is provided to explain the existence of the two process windows that exist for 3X density multiplication patterns. There is a higher difference in the free energy between the desired assembly orientation and other competitive orientations at approximately $W/L_0 = 0.5$ and $W/L_0 = 1.5$. The free-energy difference can be controlled through modification of the chemistry of the guide stripe or backfill. Thin stripe patterns are shown to have a increased selection for the desired assembly orientation when the preference for the guided

block is increased, while the chemistry of the wider stripes must be more tightly controlled, as a stripe that is too prefential will result in a wetting of the stripe by the guided material and the formation of nonbulk morphologies. All the simulation results were corroborated with experimental evidence to provide an explanation for the observed trends and pattern design guidelines.

The assembly of lines-and-spaces has been well studied, and the work presented in chapter three adds to the body of work that exists in literature already. However, there exists no simulation model which attempts to model the substrate precisely. As there is still improvement that needs to be made to process flows to make DSA technology ready for industrial fabrication, the substrate in the molecular models may need to implement a more rigorous definition of the polymer-substrate pattern interface. The impact of topographical features, as well as the variation in material that exists across the pattern needs to be understood. The LiNe flow utilizes cross-linked polystyrene for the guiding stripe and brush molecules for the backfill, this leads to one region of the periodic pattern (the XPS) being impenetrable, while there is interpenetration with the polymer brush, which is in agreement with results shown in Chapter 2. Performing a rigorous analysis of a comprehensive substrate, may be necessary in understanding three dimensional shape of the morphologies assembled as well as insight into the existence of defects, which have been shown to be energetically unfavorable.

Finally in Chapter 4, we focused on cylinder forming polymers. Using the string method, we were able to define the minimum free energy path between defective morphologies within cylindrical confinements that are used for assembling vertical interconnect accesses. The results imply that when designing these confinements, the sidewall chemistry of the confinement is the most important in minimizing the likelihood of an assembly getting trapped in a defective state. Strongly preferential sidewalls reduce the kinetic barriers in the transition pathway from defective states to the desired cylindrical morphology. We also present a theoretical confinement design to provide placement accuracy when assembling the cylindrical

features, as this can be important in industrial application.

These works focused on analyzing assembled morphologies versus other metastable states in the presence of chemical patterns. However, this analysis cannot comprehensively determine the efficacy of a chemical pattern for eliminating the possibility of stabilized defective structures, and ensuring that the stabilized morphology is useful for the desired industrial application. Without elucidating the kinetics of defect formation, then a complete understanding of the relationship between desirable and undesirable morphologies is impossible. As the TICG model is used in Monte Carlo simulations, the kinetics of assembly processes are difficult to obtain. The string method can help provide insight into the pathways between two states, as demonstrated in Chapter 4. Instead of using the string method to analyze the pathway between two states, there has been work in the de Pablo group to attempt to define one of the end states of the string as disorder. By pinning one of the states as a disordered block copolymer, there is the possibility of gleaning information about the minimum free-energy path that exists to take a system to the desired state. This could be the next step necessary in identifying pattern designs that can help experimentalists realize assemblies that meet the stringent rules set by industrial needs.

REFERENCES

[1] F. Bates and G. Fredrickson, "Block copolymer thermodynamics: theory and experiment," *Annual Review of Physical Chemistry*, vol. 41, no. 1, pp. 525–557, 1990.

[2] F. S. Bates and G. H. Fredrickson, "Block Copolymers Designer Soft Materials," *Physics Today*, vol. 52, no. 2, p. 32, 1999.

[3] H. Frielinghaus, N. Hermsdorf, K. Almdal, K. Mortensen, L. Messé, L. Corvazier, J. Fairclough, A. Ryan, P. Olmsted, and I. Hamley, "Micro-vs. macro-phase separation in binary blends of poly (styrene)-poly (isoprene) and poly (isoprene)-poly (ethylene oxide) diblock copolymers," *EPL (Europhysics Letters)*, vol. 53, p. 680, 2001.

[4] M. P. Stoykovich, M. Müller, S. O. Kim, H. H. Solak, E. W. Edwards, J. J. de Pablo, and P. F. Nealey, "Directed assembly of block copolymer blends into nonregular device-oriented structures.," *Science (New York, N.Y.)*, vol. 308, pp. 1442–6, jun 2005.

[5] M. P. Stoykovich, H. Kang, K. C. Daoulas, G. Liu, C.-C. Liu, J. J. De Pablo, M. Müller, and P. F. Nealey, "Directed self-assembly of block copolymers for nanolithography: Fabrication of isolated features and essential integrated circuit geometries," *ACS Nano*, vol. 1, no. 3, pp. 168–175, 2007.

[6] S. O. Kim, H. H. Solak, M. P. Stoykovich, N. J. Ferrier, J. J. De Pablo, and P. F. Nealey, "Epitaxial self-assembly of block copolymers on lithographically defined nanopatterned substrates.," *Nature*, vol. 424, no. 6947, pp. 411–4, 2003.

[7] R. Ruiz, H. Kang, F. A. Detcheverry, E. Dobisz, D. S. Kercher, T. R. Albrecht, J. J. de Pablo, and P. F. Nealey, "Density Multiplication and Improved Lithography by Directed Block Copolymer Assembly," *Science*, vol. 321, no. 5891, pp. 936–939, 2008.

[8] D. Angelescu, J. Waller, D. Adamson, P. Deshpande, S. Chou, R. Register, and P. Chaikin, "Macroscopic orientation of block copolymer cylinders in single-layer films by shearing," *Advanced Materials*, vol. 16, no. 19, pp. 1736–1740, 2004.

[9] S. Okamoto, K. Saijo, and T. Hashimoto, "Real-time saxs observations of lamella-forming block copolymers under large oscillatory shear deformation," *Macromolecules*, vol. 27, no. 20, pp. 5547–5555, 1994.

[10] J. Zipfel, P. Lindner, M. Tsianou, P. Alexandridis, and W. Richtering, "Shear-induced formation of multilamellar vesicles (onions) in block copolymers," *Langmuir*, vol. 15, no. 8, pp. 2599–2602, 1999.

[11] G. Arya and A. Panagiotopoulos, "Log-rolling micelles in sheared amphiphilic thin films," *Physical review letters*, vol. 95, no. 18, p. 188301, 2005.

[12] A. Zvelindovsky, G. Sevink, and J. Fraaije, "Shear-induced transitions in a ternary polymeric system," *Physical Review E*, vol. 62, no. 3, pp. 3063–3066, 2000.

[13] B. L. Peters, A. Ramírez-Hernández, D. Q. Pike, M. Müller, and J. J. de Pablo, "Nonequilibrium simulations of lamellae forming block copolymers under steady shear: A comparison of dissipative particle dynamics and brownian dynamics," *Macromolecules*, vol. 45, no. 19, pp. 8109–8116, 2012.

[14] S. Hur, C. Garcia-Cervera, E. Kramer, and G. Fredrickson, "Scft simulations of thin film blends of block copolymer and homopolymer laterally confined in a square well," *Macromolecules*, vol. 42, no. 15, pp. 5861–5872, 2009.

[15] R. Segalman, H. Yokoyama, and E. Kramer, "Graphoepitaxy of spherical domain block copolymer films," *Advanced Materials*, vol. 13, no. 15, pp. 1152–1155, 2001.

[16] A. Marencic and R. Register, "Controlling Order in Block Copolymer Thin Films for Nanopatterning Applications," *Annual Review of Chemical and Biomolecular Engineering*, vol. 1, pp. 277–297, 2010.

[17] F. A. Detcheverry, H. Kang, K. C. Daoulas, M. Müller, P. F. Nealey, and J. J. D. Pablo, "Monte Carlo Simulations of a Coarse Grain Model for Block Copolymers and Nanocomposites," *Macromolecules*, vol. 41, pp. 4989–5001, 2008.

[18] F. A. Detcheverry, D. Q. Pike, P. F. Nealey, M. Muller, and J. J. de Pablo, "Monte Carlo Simulation of Coarse Grain Polymeric Systems," *Physical Review Letters*, vol. 102, p. 197801, may 2009.

[19] C.-C. Liu, E. Han, M. S. Onses, C. J. Thode, S. Ji, P. Gopalan, and P. F. Nealey, "Fabrication of lithographically defined chemically patterned polymer brushes and mats," *Macromolecules*, vol. 44, no. 7, pp. 1876–1885, 2011.

[20] J. Qin, G. S. Khaira, Y. Su, G. P. Garner, M. Miskin, H. M. Jaeger, and J. J. de Pablo, "Evolutionary pattern design for copolymer directed self-assembly," *Soft Matter*, vol. 9, pp. 11467–11472, 2013.

[21] A. Ramírez-Hernández, H. S. Suh, P. F. Nealey, and J. J. De Pablo, "Control of directed self-assembly in block polymers by polymeric topcoats," *Macromolecules*, vol. 47, no. 10, pp. 3520–3527, 2014.

[22] M. Matsen, "The standard Gaussian model for block copolymer melts," *Journal of Physics: Condensed Matter*, vol. 14, pp. R21–R47, 2002.

[23] B. L. Peters, B. Rathsack, M. Somervell, T. Nakano, G. Schmid, and J. J. De Pablo, "Graphoepitaxial assembly of cylinder forming block copolymers in cylindrical holes," *Journal of Polymer Science, Part B: Polymer Physics*, vol. 53, no. 6, pp. 430–441, 2015.

[24] S.-M. Hur, V. Thapar, A. Ramírez-Hernández, G. Khaira, T. Segal-Peretz, P. A. R. Delgadillo, W. Li, M. Müller, P. F. Nealey, and J. J. de Pablo, "Molecular pathways for defect annihilation in directed self-assembly," *Proceedings of the National Academy of Sciences*, vol. 112, pp. 14144–14149, nov 2015.

[25] G. P. Garner, P. Rincon Delgadillo, R. Gronheid, P. F. Nealey, and J. J. de Pablo, "Design of surface patterns with optimized thermodynamic driving forces for the directed self-assembly of block copolymers in lithographic applications," *Mol. Syst. Des. Eng.*, pp. –, 2017.

[26] J. K. Cheng, C. T. Rettner, D. P. Sanders, H. C. Kim, and W. D. Hinsberg, "Dense self-assembly on sparse chemical patterns: Rectifying and multiplying lithographic patterns using block copolymers," *Advanced Materials*, vol. 20, no. 16, pp. 3155–3158, 2008.

[27] C.-C. Liu, A. Ramírez-Hernández, E. Han, G. S. W. Craig, Y. Tada, and P. F. Nealey, "Chemical Patterns for Directed Self-Assembly of Lamellae-Forming Block Copolymers with Density Multiplication of Features," *Macromolecules*, vol. 46, no. 6, pp. 1415–1424, 2013.

[28] E. W. Edwards, M. Müller, M. P. Stoykovich, H. H. Solak, J. J. De Pablo, and P. F. Nealey, "Dimensions and shapes of block copolymer domains assembled on lithographically defined chemically patterned substrates," *Macromolecules*, vol. 40, no. 1, pp. 90–96, 2007.

[29] C.-C. Liu, C. J. Thode, P. A. Rincon Delgadillo, G. S. W. Craig, P. F. Nealey, and R. Gronheid, "Towards an all-track 300 mm process for directed self-assembly," *Journal of Vacuum Science & Technology B: Microelectronics and Nanometer Structures*, vol. 29, no. 6, p. 06F203, 2011.

[30] D. P. Sanders, J. Cheng, C. T. Rettner, W. D. Hinsberg, H.-C. Kim, H. T. Friz, S. Harrer, S. Holmes, and M. Colburn, "Integration of directed self-assembly with 193 nm lithography," *Journal of Photopolymer Science and Technology*, vol. 23, no. 1, pp. 11–18, 2010.

[31] P. Mansky, Y. Liu, E. Huang, T. P. Russell, and C. J. Hawker, "Controlling polymer-surface interactions with random copolymer brushes," *Science (New York, N.Y.)*, vol. 275, no. 5305, pp. 1458–1460, 1997.

[32] E. Han, K. O. Stuen, Y. H. La, P. F. Nealey, and P. Gopalan, "Effect of composition of substrate-modifying random copolymers on the orientation of symmetric and asymmetric diblock copolymer domains," *Macromolecules*, vol. 41, no. 23, pp. 9090–9097, 2008.

[33] P. A. R. Delgadillo, R. Gronheid, C. J. Thode, H. P. Wu, Y. Cao, G. Y. Lin, M. Somervell, K. Nafus, and P. F. Nealey, "Geometric Control of Chemically Nanopatterned Substrates for Feature Multiplication Using Directed Self-Assembly of Block Copolymers," *Journal of Photopolymer Science and Technology*, vol. 25, no. 1, pp. 77–81, 2012.

[34] P. Rincon Delgadillo, G. P. Garner, R. Gronheid, J. J. de Pablo, and P. F. Nealey *In Preparation.*

[35] X. Man, D. Andelman, and H. Orland, "Block copolymer at nano-patterned surfaces," *Macromolecules*, vol. 43, no. 17, pp. 7261–7268, 2010.

[36] K. Izumi, N. Laachi, X. Man, K. T. Delaney, and G. H. Fredrickson, "Self-consistent field theory of directed self-assembly on chemically prepatterned surfaces," *Proc. SPIE*, vol. 9049, pp. 904922–904922–7, 2014.

[37] A. Ramírez-Hernández, G. Liu, P. F. Nealey, and J. J. de Pablo, "Symmetric Diblock Copolymers Confined by Two Nanopatterned Surfaces," *Macromolecules*, vol. 45, pp. 2588–2596, mar 2012.

[38] G. Liu, H. Kang, G. S. W. Craig, F. a. Detcheverry, J. J. de Pablo, and P. F. Nealey, "Cross-sectional Imaging of Block Copolymer Thin Films on Chemically Pattemed Surfaces," *Journal of Photopolymer Science and Technology*, vol. 23, no. 2, pp. 149–154, 2010.

[39] G. Liu, F. Detcheverry, A. Ramírez-Hernández, H. Yoshida, Y. Tada, J. J. De Pablo, and P. F. Nealey, "Nonbulk complex structures in thin films of symmetric block copolymers on chemically nanopatterned surfaces," *Macromolecules*, vol. 45, no. 9, pp. 3986–3992, 2012.

[40] D. Zhang, S. M. Dougal, and M. S. Yeganeh, "Effects of UV Irradiation and Plasma Treatment on a Polystyrene Surface Studied by IR - Visible Sum Frequency Generation Spectroscopy," *Langmuir*, vol. 16, no. 10, pp. 4528–4532, 2000.

[41] R. Seidel, L. Williamson, Y. Her, J. Kim, G. Lin, P. Nealey, and R. Gronheid, "The role of guide stripe chemistry in block copolymer directed self-assembly," *Proc. SPIE*, vol. 9425, pp. 94250W–94250W–9, 2015.

[42] L. D. Williamson, R. N. Seidel, X. Chen, H. S. Suh, P. A. R. Delgadillo, R. Gronheid, and P. F. Nealey, "Three-Tone Chemical Patterns for Block Copolymer Directed Self-Assembly," *ACS Applied Materials and Interfaces*, vol. 8, no. 4, pp. 2704–2712, 2016.

[43] F. A. Detcheverry, G. Liu, P. F. Nealey, and J. J. de Pablo, "Interpolation in the Directed Assembly of Block Copolymers on Nanopatterned Substrates: Simulation and Experiments," *Macromolecules*, vol. 43, pp. 3446–3454, apr 2010.

[44] R. Seidel, P. Rincon Delgadillo, A. Ramírez-Hernández, H. Wu, Y. Her, J. Yin, R. Gronheid, P. Nealey, and J. de Pablo, "Investigation of cross-linking poly(methyl methacrylate) as a guiding material in block copolymer directed self-assembly," *Proc. SPIE*, vol. 9051, pp. 90510K–90510K–10, 2014.

[45] P. A. R. Delgadillo, R. Gronheid, C. J. Thode, H. Wu, Y. Cao, M. Neisser, M. Somervell, K. Nafus, and P. F. Nealey, "Implementation of a chemo-epitaxy flow for directed self-assembly on 300-mm wafer processing equipment," *Journal of Micro/Nanolithography, MEMS, and MOEMS*, vol. 11, no. 3, pp. 31302–31305, 2012.

[46] U. Nagpal, M. Müller, P. F. Nealey, and J. J. D. Pablo, "Free Energy of Defects in Ordered Assemblies of Block Copolymer Domains," *ACS Macro Letters*, vol. 1, no. 3, pp. 418–422, 2012.

[47] S.-J. Jeong, J. E. Kim, H.-S. Moon, B. H. Kim, S. M. Kim, J. B. Kim, and S. O. Kim, "Soft Graphoepitaxy of Block Copolymer Assembly with Disposable Photoresist Confinement," *Nano Letters*, vol. 9, pp. 2300–2305, jun 2009.

[48] J. Y. Cheng, A. M. Mayes, and C. A. Ross, "Nanostructure engineering by templated self-assembly of block copolymers," *Nature Materials*, vol. 3, pp. 823–828, nov 2004.

[49] J. Y. Cheng, D. P. Sanders, H. D. Truong, S. Harrer, A. Friz, S. Holmes, M. Colburn, and W. D. Hinsberg, "Simple and versatile methods to integrate directed self-assembly with optical lithography using a polarity-switched photoresist," *ACS Nano*, vol. 4, no. 8, pp. 4815–4823, 2010.

[50] H. Kato, Y. Seino, H. Yonemitsu, H. Sato, M. Kanno, K. Kobayashi, A. Kawanishi, T. Imamura, M. Omura, N. Nakamura, and T. Azuma, "Sub-30nm via interconnects fabricated using directed self-assembly," *Microelectronic Engineering*, vol. 110, pp. 152–155, oct 2013.

[51] Y. Seino, H. Yonemitsu, H. Sato, M. Kanno, H. Kato, K. Kobayashi, A. Kawanishi, T. Azuma, M. Muramatsu, S. Nagahara, T. Kitano, and T. Toshima, "Contact hole shrink process using directed self-assembly," in *Proceedings of SPIE* (W. M. Tong, ed.), vol. 8323, pp. 83230Y–83230Y–7, mar 2012.

[52] Y. Ma, J. A. Torres, G. Fenger, Y. Granik, J. Ryckaert, G. Vanderberghe, J. Bekaert, and J. Word, "Challenges and opportunities in applying grapho-epitaxy DSA lithography to metal cut and contact/via applications," in *Proceedings of SPIE* (U. F. W. Behringer, ed.), vol. 9231, p. 92310T, oct 2014.

[53] R. A. Segalman, H. Yokoyama, and E. Kramer, "Graphoepitaxy of Spherical Domain Block Copolymer Films," *Advanced Materials*, vol. 13, pp. 1152–1155, aug 2001.

[54] R. A. Segalman, A. Hexemer, and E. J. Kramer, "Effects of Lateral Confinement on Order in Spherical Domain Block Copolymer Thin Films," *Macromolecules*, vol. 36, pp. 6831–6839, sep 2003.

[55] R. A. Segalman, K. E. Schaefer, G. H. Fredrickson, E. J. Kramer, and S. Magonov, "Topographic Templating of Islands and Holes in Highly Asymmetric Block Copolymer Films," *Macromolecules*, vol. 36, pp. 4498–4506, jun 2003.

[56] R. A. Segalman, A. Hexemer, and E. J. Kramer, "Edge Effects on the Order and Freezing of a 2D Array of Block Copolymer Spheres," *Physical Review Letters*, vol. 91, p. 196101, nov 2003.

[57] G. Liu, A. Ramírez-Hernández, H. Yoshida, K. Nygård, D. K. Satapathy, O. Bunk, J. J. de Pablo, and P. F. Nealey, "Morphology of Lamellae-Forming Block Copolymer

Films between Two Orthogonal Chemically Nanopatterned Striped Surfaces," *Physical Review Letters*, vol. 108, p. 065502, feb 2012.

[58] C. Park, J. Y. Cheng, M. J. Fasolka, A. M. Mayes, C. A. Ross, E. L. Thomas, and C. De Rosa, "Double textured cylindrical block copolymer domains via directional solidification on a topographically patterned substrate," *Applied Physics Letters*, vol. 79, pp. 848–850, aug 2001.

[59] S. M. Park, M. P. Stoykovich, R. Ruiz, Y. Zhang, C. T. Black, and P. F. Nealey, "Directed Assembly of Lamellae Forming Block Copolymers by Using Chemically and Topographically Patterned Substrates," *Advanced Materials*, vol. 19, pp. 607–611, feb 2007.

[60] T. R. Younkin, R. Gronheid, P. A. R. Delgadillo, B. T. Chan, N. Vandenbroeck, S. Demuynck, A. Romo-Negreira, D. Parnell, K. Nafus, S. Tahara, and M. Somervell, "Progress in directed self-assembly hole shrink applications," in *Proceedings of SPIE* (M. H. Somervell, ed.), vol. 8682, p. 86820L, mar 2013.

[61] R. Tiron, a. Gharbi, M. Argoud, X. Chevalier, J. Belledent, P. Pimmenta Barros, C. Navarro, G. Cunge, S. Barnola, L. Pain, M. Asai, and C. Pieczulewski, "The potential of block copolymer's directed self-assembly for contact hole shrink and contact multiplication," *Proc. of SPIE*, vol. 8680, pp. 868012–868012–11, mar 2013.

[62] J. A. Torres, K. Sakajiri, D. Fryer, Y. Granik, Y. Ma, P. Krasnova, G. Fenger, S. Nagahara, S. Kawakami, B. Rathsack, G. Khaira, J. de Pablo, and J. Ryckaert, "Physical verification and manufacturing of contact/via layers using grapho-epitaxy DSA processes," *Proceedings of SPIE*, vol. 9053, p. 90530R, mar 2014.

[63] R. Tiron, A. Gharbi, P. Pimenta Barros, S. Bouanani, C. Lapeyre, S. Bos, A. Fouquet, J. Hazart, X. Chevalier, M. Argoud, G. Chamiot-Maitral, S. Barnola, C. Monget, V. Farys, S. Berard-Bergery, L. Perraud, C. Navarro, C. Nicolet, G. Hadziioannou, and G. Fleury, "Template affinity role in CH shrink by DSA planarization," in *Proceedings of SPIE* (D. J. Resnick and C. Bencher, eds.), vol. 9423, p. 942317, mar 2015.

[64] R. Gronheid, J. Doise, J. Bekaert, B. T. Chan, I. Karageorgos, J. Ryckaert, G. Vandenberghe, Y. Cao, G. Lin, M. Somervell, G. Fenger, and D. Fuchimoto, "Implementation of templated DSA for via layer patterning at the 7nm node," in *Proceedings of SPIE* (D. J. Resnick and C. Bencher, eds.), vol. 9423, p. 942305, mar 2015.

[65] T. Iwama, N. Laachi, K. T. Delaney, B. Kim, and G. H. Fredrickson, "Computational studies of shape rectification in directed self-assembly," in *SPIE Advanced Lithography* (D. J. Resnick and C. Bencher, eds.), vol. 9049, p. 904927, mar 2014.

[66] T. Iwama, N. Laachi, K. T. Delaney, and G. H. Fredrickson, "Field-theoretic Simulations of Directed Self-assembly for Contact Multiplication," *Journal of Photopolymer Science and Technology*, vol. 28, no. 5, pp. 689–693, 2015.

[67] A. Latypov, M. Preil, G. Schmid, J. Xu, H. Yi, K. Yoshimoto, and Y. Zou, "Exploration of the directed self-assembly based nano-fabrication design space using computational simulations," in *Alternative Lithographic Technologies V* (W. M. Tong and D. J. Resnick, eds.), vol. 8680, p. 868013, mar 2013.

[68] A. Yoshida, K. Yoshimoto, and M. Ohshima, "Effect of wall potential on morphology of symmetric diblock copolymers in nanotrench," *Japanese Journal of Applied Physics*, vol. 55, p. 06GE01, jun 2016.

[69] N. Laachi, K. T. Delaney, B. Kim, S.-M. Hur, R. Bristol, D. Shykind, C. J. Weinheimer, and G. H. Fredrickson, "Self-consistent field theory investigation of directed self-assembly in cylindrical confinement," *Journal of Polymer Science Part B: Polymer Physics*, vol. 53, pp. 142–153, jan 2015.

[70] J. Doise, J. Bekaert, B. T. Chan, R. Gronheid, Y. Cao, S. Hong, G. Lin, D. Fishman, Y. Chakk, and T. Marzook, "Implementation of surface energy modification in graphoepitaxy directed self-assembly for hole multiplication," *Journal of Vacuum Science & Technology B, Nanotechnology and Microelectronics: Materials, Processing, Measurement, and Phenomena*, vol. 33, p. 06F301, nov 2015.

[71] N. Laachi, T. Iwama, K. T. Delaney, D. Shykind, C. J. Weinheimer, and G. H. Fredrickson, "Directed self-assembly of linear arrays of block copolymer cylinders," *Journal of Polymer Science Part B: Polymer Physics*, vol. 53, pp. 317–326, mar 2015.

[72] M. W. Matsen and M. Schick, "Stable and Unstable Phases of a Linear Multiblock Copolymer Melt," *Macromolecules*, vol. 27, pp. 7157–7163, nov 1994.

[73] G. Fredrickson, *The Equilibrium Theory of Inhomogeneous Polymers*. Oxford University Press, dec 2005.

[74] W. E, W. Ren, and E. Vanden-Eijnden, "String method for the study of rare events," *Physical Review B*, vol. 66, p. 052301, aug 2002.

[75] W. E, W. Ren, and E. Vanden-Eijnden, "Simplified and improved string method for computing the minimum energy paths in barrier-crossing events," *The Journal of Chemical Physics*, vol. 126, p. 164103, apr 2007.

[76] W. E, W. Ren, and E. Vanden-Eijnden, "Finite Temperature String Method for the Study of Rare Events," *The Journal of Physical Chemistry B*, vol. 109, pp. 6688–6693, apr 2005.

[77] E. Vanden-Eijnden and M. Venturoli, "Revisiting the finite temperature string method for the calculation of reaction tubes and free energies," *The Journal of Chemical Physics*, vol. 130, p. 194103, may 2009.

[78] L. Maragliano, A. Fischer, E. Vanden-Eijnden, and G. Ciccotti, "String method in collective variables: Minimum free energy paths and isocommittor surfaces," *The Journal of Chemical Physics*, vol. 125, no. 2, p. 024106, 2006.

[79] L. Maragliano and E. Vanden-Eijnden, "On-the-fly string method for minimum free energy paths calculation," *Chemical Physics Letters*, vol. 446, pp. 182–190, sep 2007.

[80] T. F. Miller, E. Vanden-Eijnden, and D. Chandler, "Solvent coarse-graining and the string method applied to the hydrophobic collapse of a hydrated chain," *Proceedings of the National Academy of Sciences*, vol. 104, pp. 14559–14564, sep 2007.

[81] X. Cheng, L. Lin, W. E, P. Zhang, and A.-C. Shi, "Nucleation of Ordered Phases in Block Copolymers," *Physical Review Letters*, vol. 104, p. 148301, apr 2010.

[82] C. L. Ting, D. Appel, and Z.-G. Wang, "Minimum Energy Path to Membrane Pore Formation and Rupture," *Physical Review Letters*, vol. 106, p. 168101, apr 2011.

[83] M. Müller, Y. G. Smirnova, G. Marelli, M. Fuhrmans, and A.-C. Shi, "Transition Path from Two Apposed Membranes to a Stalk Obtained by a Combination of Particle Simulations and String Method," *Physical Review Letters*, vol. 108, p. 228103, may 2012.

[84] W. Li, P. F. Nealey, J. J. De Pablo, and M. Müller, "Defect removal in the course of directed self-assembly is facilitated in the vicinity of the order-disorder transition," *Physical Review Letters*, vol. 113, no. 16, pp. 1–5, 2014.